

Department of Advanced Energy  
Transdisciplinary Sciences  
Graduate School of Frontier Sciences  
The University of Tokyo

2020

Master's Thesis

Multi-Objective Optimization of Coil Parameters and Operation  
Frequency for Lunar Rover Wireless Power Transfer System  
(月面探査機ワイヤレス給電システムにおけるコイルパラメ  
ータと動作周波数の多目的最適化に関する研究)

Submitted January 26, 2021

Adviser: Associate Professor Hiroshi Fujimoto

陳 名洋

47196061 Mingyang Chen



I would like to dedicate this thesis to my parents.





## **Declaration**

I hereby declare that except where specific reference is made to the work of others, the contents of this dissertation are original and have not been submitted in whole or in part for consideration for any other degree or qualification in this, or any other university. This dissertation is my own work and contains nothing which is the outcome of work done in collaboration with others, except as specified in the text and Acknowledgements. This dissertation contains fewer than 65,000 words including appendices, bibliography, footnotes, tables and equations and has fewer than 150 figures.

Chen Mingyang  
February 2021



## Acknowledgements

Here, first of all I want to thank the Hori-Fujimoto laboratory. The laboratory has provided me with a free research environment and has given me a lot of help.

In the laboratory, I first want to express my gratitude and appreciation to Prof. Hori Yoich. He is highly respected, but still very patient, and even spends time to guide my research during the New Year.

Secondly, I want to thank Prof. Hiroshi Fujimoto, who is serious and responsible, and even replies to my emails at mid-night.

Thirdly, I would thank the assistant professors Dr. Osamu Shimizu, Dr. Toshiyuki Fujita and Dr. Sakahisa Nagai, they listened to my troubles at the WPT team meetings and gave me suggestions.

I further like to thank Mr. Shimada Shunhei, Mrs. Honda Sayuri and Mr. Osamu Kawasaki from JAXA, as well as Dr. Katsuhiro Hata and Prof. Takehiro Imura, they provided me with research topics and guidance.

In addition, I would like to thank Dr. Ji Bingcheng, without his pioneer research on Lunar rover WPT system and advice, there would not have been this thesis. Together, I would like to express my appreciate to Hong Chonghao, Jirawat Sithinamsuwan, Keiichiro Tokita, Feng Zhe, Daisuke Shirasaki and Ryo Matsumoto. They gave me suggestions at team meetings, helped me with my experiments.

Finally, I would like to thank my parents Mr. Chen Gaoyun and Mrs. Li Jianyu. They have always given me material and spiritual support. Especially my mother Li Jianyu, as a junior high school teacher, she went out early and returned late for over 20 consecutive years. I hope she can soon achieve her dream of opening a bakery near her school.



## **Abstract**

In this thesis, the optimization of coil design parameters and resonant frequency for Lunar rover WPT system is discussed.

The speciality of the objective system is the combination of PV MPPT and WPT, which leads to possibility of frequency splitting at MPPT process. And operation at an extreme temperature situation on lunar surface, which leads to parameter variation of compensate capacitors. Optimization method for this occasion is still in absence.

To determine the PV output for static efficiency optimization, frequency-duty two dimensional MPPT strategies, taking frequency splitting phenomenon detection in WPT into the MPPT algorithm, were proposed and verified by experiment.

Multi-objective optimization algorithm through half-FE and half-numerical modeling based on Meta-heuristic algorithms were proposed.

Applying the concept of Pareto optimal in the algorithm, this thesis not only achieved the improvement of static PV-load efficiency from 75 percent of previous Lunar rover WPT prototype to over 90 percent including the secondary DC-DC converter for a passive rectified WPT system at a 130 Watt experiment, but also showed the potential for design evaluation and performance visualization of the proposed method through the evaluation of JAXA's coil designs.



# Table of contents

|  |            |
|--|------------|
| <b>List of figures</b>   | <b>xv</b>  |
| <b>List of tables</b>  | <b>xix</b> |
| <b>Nomenclature</b>  | <b>xxi</b> |
| <b>1 Introduction</b>  | <b>1</b>   |
| 1.1 Lunar Rover WPT system . . . . .                                     | 1          |
| 1.1.1 Lunar Exploration and Lunar Rover . . . . .                        | 1          |
| 1.1.2 Wireless Power Transfer . . . . .                                  | 4          |
| 1.1.3 Lunar Rover Wireless Power Transfer System . . . . .               | 7          |
| 1.1.4 Photo-voltaic Cell and Maximum Power Point Tracking . . . . .      | 9          |
| 1.2 Lunar Rover WPT Frequency and Coil optimization background . . . . . | 10         |
| 1.2.1 Design of WPT Coils and Frequency . . . . .                        | 10         |
| 1.2.2 Specialized Characteristics in Lunar Rover WPT Design . . . . .    | 11         |
| 1.3 Thesis Outline . . . . .   | 13         |
| <b>2 Lunar Rover WPT Modeling</b>  | <b>15</b>  |
| 2.1 PV Output Modeling . . . . .   | 16         |
| 2.2 WPT Circuit Modeling . . . . .                                       | 19         |
| 2.3 Applied WPT Modeling . . . . .                                       | 22         |
| 2.4 Other Loss Evaluations . . . . .                                     | 24         |
| 2.4.1 Voltage Driven Inverter . . . . .                                  | 24         |
| 2.4.2 Current Driven Rectifier . . . . .                                 | 26         |
| 2.4.3 DC-DC Converter . . . . .  | 27         |
| 2.5 Half-FE Litz Wire Modeling . . . . .                                 | 29         |
| 2.6 Regression Model with MLI . . . . .                                  | 30         |
| 2.7 Verification of Modeling . . . . .                                   | 33         |
| 2.7.1 Verification for Regression Model . . . . .                        | 33         |

|          |   |           |
|----------|---|-----------|
| 2.7.2    | Verification for FE Model and AC-resistance Calculation . . .               | 37        |
| 2.7.3    | Verification for DC-DC loss estimation . . . . .                            | 40        |
| 2.8      | Summary . . . . .   | 42        |
| <b>3</b> | <b>Conventional and Proposed MPPT Strategies for Lunar Rover WPT system</b> | <b>45</b> |
| 3.1      | Review of previous Lunar Rover MPPT Strategies . . . . .                    | 45        |
| 3.1.1    | Duty-Sweep Method . . . . .   | 46        |
| 3.1.2    | Perturb and observe algorithm . . . . .                                     | 46        |
| 3.1.3    | Variant Step Incremental Conductance Method . . . . .                       | 47        |
| 3.1.4    | Particle Swarm Optimization Method . . . . .                                | 48        |
| 3.1.5    | Drawbacks of the previous methods . . . . .                                 | 48        |
| 3.2      | Experimental Platform Manufacturing . . . . .                               | 48        |
| 3.3      | Proposed Duty-sweep MPPT with frequency adjustment . . . . .                | 49        |
| 3.3.1    | Motivation and application . . . . .  | 50        |
| 3.3.2    | Proposed Algorithm . . . . .  | 51        |
| 3.3.3    | Experimental Verification . . . . .   | 53        |
| 3.4      | Proposed Duty-frequency 2-dimensional MPPT . . . . .                        | 53        |
| 3.4.1    | Duty-frequency two dimensional sweeping . . . . .                           | 54        |
| 3.4.2    | Duty-frequency two dimensional PSO . . . . .                                | 55        |
| 3.4.3    | Experiment Verification . . . . .   | 56        |
| 3.5      | Summary . . . . .   | 57        |
| <b>4</b> | <b>Single-Objective Optimization for Lunar Rover WPT</b>                    | <b>59</b> |
| 4.1      | Optimization based on Measurement . . . . .                                 | 59        |
| 4.2      | Optimization Based on Meta-heuristic algorithms . . . . .                   | 61        |
| 4.2.1    | Exhaustive Algorithm . . . . .  | 63        |
| 4.2.2    | PSO optimization for KQ product . . . . .                                   | 64        |
| 4.2.3    | Genetic algorithm and GA optimization for KQ product . . .                  | 64        |
| 4.2.4    | Discussion of Optimization results and Algorithm Selection .                | 67        |
| 4.3      | Proposed Logistic PSO . . . . .   | 68        |
| 4.3.1    | Motivation of Modified Algorithm . . . . .                                  | 68        |
| 4.3.2    | Principles of Modified Algorithm . . . . .                                  | 69        |
| 4.3.3    | Test of New Algorithm . . . . .   | 70        |
| 4.4      | Summary . . . . .   | 72        |
| <b>5</b> | <b>Multi-Objective optimization for Lunar Rover WPT</b>                     | <b>73</b> |
| 5.1      | Pareto Optimization . . . . .   | 74        |



|          |   |            |
|----------|---|------------|
| 5.1.1    | Review of Pareto Optimization in the WPT Design . . . . .           | 75         |
| 5.2      | Frequency Optimization based on Measurement . . . . .               | 75         |
| 5.2.1    | Cost Functions . . . . .  | 75         |
| 5.2.2    | Chebyshev Metric Method . . . . .                                   | 76         |
| 5.2.3    | Optimization results . . . . .                                      | 77         |
| 5.2.4    | Design Intuitions . . . . .   | 78         |
| 5.3      | Air-gap efficiency Pareto Optimization . . . . .                    | 78         |
| 5.3.1    | Design Background . . . . .   | 79         |
| 5.3.2    | Multi-Objective Optimization based on Decomposition . . . . .       | 79         |
| 5.3.3    | MOEA/D Optimization Results . . . . .                               | 81         |
| 5.3.4    | Design Intuitions . . . . .   | 83         |
| 5.4      | Power Density and Thermal Density Pareto Optimization . . . . .     | 83         |
| 5.4.1    | Implementation of L-MOPSO . . . . .                                 | 84         |
| 5.4.2    | Cost Functions . . . . .  | 86         |
| 5.4.3    | Optimization Results . . . . .                                      | 92         |
| 5.4.4    | Selected Design Example and Experiment . . . . .                    | 97         |
| 5.5      | Summary . . . . .   | 99         |
| <b>6</b> | <b>Evaluation of JAXA's Coil Design</b>                             | <b>101</b> |
| 6.1      | Brief Introduction to Coil Design Experiments . . . . .             | 102        |
| 6.1.1    | Experiment Setup and FE Reproduction . . . . .                      | 102        |
| 6.1.2    | Cost Functions . . . . .  | 104        |
| 6.1.3    | Result . . . . .  | 104        |
| 6.2      | Single Objective Optimization for Experiment Reproduction . . . . . | 104        |
| 6.3      | Multi-Objective Optimization for Experiment Reproduction . . . . .  | 106        |
| 6.3.1    | Cost Functions . . . . .  | 107        |
| 6.3.2    | Optimization Results . . . . .                                      | 107        |
| 6.4      | Summary . . . . .   | 110        |
| <b>7</b> | <b>Conclusion and Future Work</b>                                   | <b>111</b> |
| 7.1      | Conclusion . . . . .  | 111        |
| 7.2      | Future Work . . . . .   | 112        |
|          | <b>References</b>   | <b>113</b> |
|          | <b>Appendix A Publication Lists</b>                                 | <b>119</b> |
| A.1      | Published . . . . .   | 119        |

|                            |     |
|----------------------------|-----|
| A.2 To be submit . . . . . | 119 |
| A.3 Awards . . . . .       | 120 |

# List of figures

|      |  |    |
|------|--|----|
| 1.1  | (a) Lunar Surface and (b) Xuanji used to observe celestial bodies in ancient times [1] . . . . .   | 2  |
| 1.2  | A Spanish Lunar Calender for year 2017 [2] . . . . .   | 3  |
| 1.3  | (a) Russian Lunar Rover and (b) Sputnik1 [3] . . . . .   | 4  |
| 1.4  | (a) conventional structure and (b) WPT system structure (c) MLI structure [4] . . . . .  | 5  |
| 1.5  | (a) 2-m 60 watt self-resonant WPT experiment by MIT [5] (b) WPT illustration experiment by Hori-fujimoto Laboratory . . . . .                        | 6  |
| 1.6  | (a) Mission plan for Lunar south polar exploration and (b) JAXA's Lunar rover prototype . . . . .  | 7  |
| 1.7  | (a) Magnetic simulation for magnetic trasmissive MLI (MT-MLI) and (b) MT-MLI prototype and (c) MT-MLI influence towards IPT efficiency [4] . . . . . | 8  |
| 1.8  | Topology of the Lunar rover prototype [6] . . . . .  | 9  |
| 1.9  | Thesis Flowchart . . . . .   | 13 |
| 2.1  | Diode model V-I Characteristics [7] . . . . .  | 16 |
| 2.2  | (a) Diode model (b) Reversed Diode (c) Diode model and Drift current produced by radiation . . . . .   | 17 |
| 2.3  | Derivation of the PV output curve . . . . .  | 17 |
| 2.4  | Equivalent model for PV . . . . .  | 18 |
| 2.5  | Estimated PV propoerty of Lunar Rover WPT prototype . . . . .  | 19 |
| 2.6  | Series-Series WPT Topology and the T-type equivalent Circuit . . . . .   | 20 |
| 2.7  | Primary(blue) and Secondary(orange) Admittance Example . . . . .   | 23 |
| 2.8  | Class-D full bridge inverter as an example . . . . .   | 25 |
| 2.9  | Class-D current driven rectifier as an example . . . . .   | 26 |
| 2.10 | Synchronous rectification type buck converter as an example . . . . .  | 27 |
| 2.11 | Mini-model of measurement for Qi-A11 Coils with MLI . . . . .  | 31 |

|      |  |    |
|------|--|----|
| 2.12 | Cases of measurement for Qi-A11 Coils with MLI . . . . .   | 33 |
| 2.13 | Results of measurement for Qi-A11 Coils with MLI . . . . .   | 34 |
| 2.14 | Results of Mutual inductance for Qi-A11 Coils case I . . . . .   | 35 |
| 2.15 | Results of Mutual inductance for Qi-A11 Coils case II . . . . .  | 35 |
| 2.16 | Results of resistance for Coil 1 case I(a) . . . . .   | 35 |
| 2.17 | Results of resistance for Coil 1 case II(a) . . . . .  | 35 |
| 2.18 | Results of resistance for Coil 1 case I(b) . . . . .   | 36 |
| 2.19 | Results of resistance for Coil 1 case II (b) . . . . .   | 36 |
| 2.20 | Results of resistance for Coil 1 case I(c) . . . . .   | 37 |
| 2.21 | Results of resistance for Coil 1 case II(c) . . . . .  | 37 |
| 2.22 | Results of resistance for Coil 2 case I(a) . . . . .   | 38 |
| 2.23 | Results of resistance for Coil 2 case II(a) . . . . .  | 38 |
| 2.24 | Results of resistance for Coil 2 case I(b) . . . . .   | 38 |
| 2.25 | Results of resistance for Coil 2 case II(b) . . . . .  | 38 |
| 2.26 | Results of resistance for Coil 2 case I(c) . . . . .   | 39 |
| 2.27 | Results of resistance for Coil 2 case II(c) . . . . .  | 39 |
| 2.28 | Comparison between the basic parameters FE model and Measure-<br>ment for a Solid Wire coil example . . . . .  | 40 |
| 2.29 | Comparison between the AC resistance of half-FE model and Mea-<br>surement for a Qi A11 coil example . . . . . | 40 |
| 2.30 | Comparison between the DC-DC efficiency calculation and measurement  | 42 |
| 2.31 | Experiment for the DC-DC efficiency measurement . . . . .  | 43 |
| 3.1  | Lunar Rover WPT topology . . . . .   | 46 |
| 3.2  | Experimental Platform . . . . .  | 47 |
| 3.3  | Admittance example without frequency splitting . . . . .   | 49 |
| 3.4  | Admittance example with frequency splitting . . . . .  | 50 |
| 3.5  | PV output property applied in the experiments . . . . .  | 51 |
| 3.6  | Experiment result of the Proposed Duty-sweep method with frequency<br>adjustment . . . . .                     | 53 |
| 3.7  | Experiment result of two-dimensional Duty-frequency sweep method   | 54 |
| 3.8  | Experiment result of two-dimensional Duty-frequency PSO method .   | 55 |
| 4.1  | Frequency optimization based on VNA measurement and regression<br>models . . . . .                             | 60 |
| 4.2  | Optimization methods of meta-heuristic algorithms . . . . .  | 62 |
| 4.3  | Optimization result of Exhaustive algorithm . . . . .  | 63 |

|      |  |     |
|------|--|-----|
| 4.4  | Optimization result of pso for WPT efficiency . . . . .  | 64  |
| 4.5  | Optimization result of pso for WPT and inverter efficiency . . . . .   | 65  |
| 4.6  | Optimization result of GA for WPT efficiency . . . . .   | 65  |
| 4.7  | Optimization result of GA for WPT and inverter efficiency . . . . .  | 66  |
| 4.8  | Distribution of three learning coefficients( blue: $c_1$ , red: $c_2$ and $c_3$ ,<br>yellow: $c_3$ ) . . . . . | 70  |
| 4.9  | The test function eggholder . . . . .  | 71  |
| 5.1  | Pareto Optimization illustration . . . . .   | 74  |
| 5.2  | Pareto Front for 6 cases . . . . .   | 77  |
| 5.3  | Efficiency and power with respect to frequency for case I . . . . .  | 77  |
| 5.4  | Efficiency and power with respect to frequency for case II . . . . .   | 77  |
| 5.5  | Frequency and number of turns on Pareto Front . . . . .  | 82  |
| 5.6  | Optimization Result of the Final External Population . . . . .   | 82  |
| 5.7  | Pareto Front of the Efficiency and Air-gap . . . . .   | 83  |
| 5.8  | Calculation method of PV-load Efficiency . . . . .   | 84  |
| 5.9  | Pareto Front of the power density and thermal density . . . . .  | 93  |
| 5.10 | Frequency on Pareto Front . . . . .  | 94  |
| 5.11 | Number of turns on Pareto Front . . . . .  | 94  |
| 5.12 | Coil outer diameter on Pareto Front . . . . .  | 94  |
| 5.13 | Pitch on Pareto Front . . . . .  | 95  |
| 5.14 | Air-gap on Pareto Front . . . . .  | 95  |
| 5.15 | Low thermal density coil Example . . . . .   | 97  |
| 5.16 | Experiment waveform of Low thermal density coil Example . . . . .  | 97  |
| 5.17 | PV output of sweep experiment . . . . .  | 98  |
| 5.18 | PV output of PSO experiment . . . . .  | 98  |
| 5.19 | PV-Load efficiency of sweep experiment . . . . .   | 98  |
| 5.20 | PV-Load efficiency of PSO experiment . . . . .   | 99  |
| 6.1  | Coil Manufactured in the experiments . . . . .   | 102 |
| 6.2  | Process of coil design experiments . . . . .   | 102 |
| 6.3  | Experiment illustration of JAXA's Coil Design . . . . .  | 103 |
| 6.4  | Result of coil design experiments . . . . .  | 104 |
| 6.5  | Single objective optimization-number of turns . . . . .  | 105 |
| 6.6  | Single objective optimization-efficiency . . . . .   | 105 |
| 6.7  | Single objective optimization-frequency . . . . .  | 106 |
| 6.8  | Pareto Front convergence . . . . .   | 106 |

|      |   |     |
|------|---|-----|
| 6.9  | Number of turns on Pareto Front . . . . . | 106 |
| 6.10 | Frequency on Pareto Front . . . . .       | 108 |
| 6.11 | KQ product on Pareto Front . . . . .      | 108 |
| 6.12 | S21 on Pareto Front . . . . .             | 109 |

# List of tables

|     |  |     |
|-----|--|-----|
| 2.1 | Estimated results of $k_{cond}$ . . . . .                            | 37  |
| 2.2 | Estimated results of $k_{total}$ . . . . .                           | 37  |
| 2.3 | Circuit properties for calculation I . . . . .                       | 41  |
| 2.4 | Circuit properties for calculation II . . . . .                      | 41  |
| 2.5 | Circuit properties for calculation III . . . . .                     | 41  |
| 2.6 | Circuit properties for calculation IV . . . . .                      | 42  |
| 2.7 | Comparison result of WPT circuit . . . . .                           | 43  |
| 4.1 | Fixed Design Parameters . . . . .                                    | 62  |
| 4.2 | Variant Design Parameters . . . . .                                  | 63  |
| 4.3 | Comaprison of proposed and conventional algorithms . . . . .         | 71  |
| 5.1 | Coil Specification in air-gap and efficiency Optimization . . . . .  | 79  |
| 5.2 | Experiment Result of MLI Influence on WPT [4] . . . . .              | 79  |
| 5.3 | Comaprison of LMOPSO and conventional algorithms . . . . .           | 86  |
| 6.1 | Coil Specification in JAXA Experiment and Optimization [4] . . . . . | 103 |





# Nomenclature

## Roman Symbols

$j$  unit imaginary number

## Greek Symbols

$\delta$  skin depth

$\eta$  efficiency

$\gamma$  indicator for skin effect

$\omega$  angular frequency

$\pi$   $\simeq 3.14 \dots$

$\sigma$  conductivity

## Superscripts

$j$  superscript index

## Subscripts

0 Resonant state or subscript index

1 Lower Resonant state or subscript index

2 Higher Resonant state or subscript index

buck buck converter

inv inverter

$j$   $j$ -th iteration or subscript index

rect rectifier

wpt WPT circuit

### **Acronyms / Abbreviations**

FEA Finite Element Analysis

FEM Finite Element Method

GA Genetic Algorithm

KQ Magnetic coupling multiply by Quality factor

PV Photo-voltaic

LMOPSO Logistic Multi-Objective Particle Swarm Optimization

LPSO Logistic Particle Swarm Optimization

MLI Multi-layer Insulation

MOEA/D Multi-Objective Evolutionary Algorithm based on Decomposition

MOPSO Multi-Objective Particle Swarm Optimization

MPPT Maximum Power Point Tracking

WPT Wireless Power Transfer

MT-MLI Magnetic Transmissive Multi-layer Insulation

NSGA Non-dominated Sorting Genetic Algorithms

GPSO Gaussian Particle Swarm Optimization

PSO Particle Swarm Optimization

MPP Maximum Power Point

pp Parallel-Parallel

ps Parallel-Series

sp Series-Parallel

ss Series-Series

# Chapter 1

## Introduction

### 1.1 Lunar Rover WPT system

Since ancient times, exploring the moon has been one of the common goals of mankind. With scientific and mineralogical objectives, several lunar rovers have been landed on the lunar surface. Lunar rover refers to a special vehicle designed for Lunar surface exploration, powered by photo-voltaic cells. Conventional Lunar rover is connected to photo-voltaic cells by wire connection, which leads heat leakage through the wire at lunar night.

Novel structure has been proposed recently [6], applying wireless power transfer (WPT) to replace the wire connection. In this scheme, the rover side is able to be wrapped by a specialized thermal isolation material, namely Magnetic Trans-missive Multi-Layer Insulation (MT-MLI) [4], eliminating the heat leakage.

Nowadays, WPT through magnetic coupling has become a general solution for cordless power transferring in various systems for middle-distance power transfer [8]. The operation frequency of WPT on earth is limited by restrictions, but for lunar rover application, restriction is in absence hence optimization of operation frequency and coil parameters is discussed in this thesis.

This chapter is the introduction to lunar rover WPT system and explanation of the research target of operation frequency and coil parameters optimization.

#### 1.1.1 Lunar Exploration and Lunar Rover

It is human nature to explore the unknown. Since ancient times, human beings have never stopped observing and exploring the universe. For example, in ancient China,

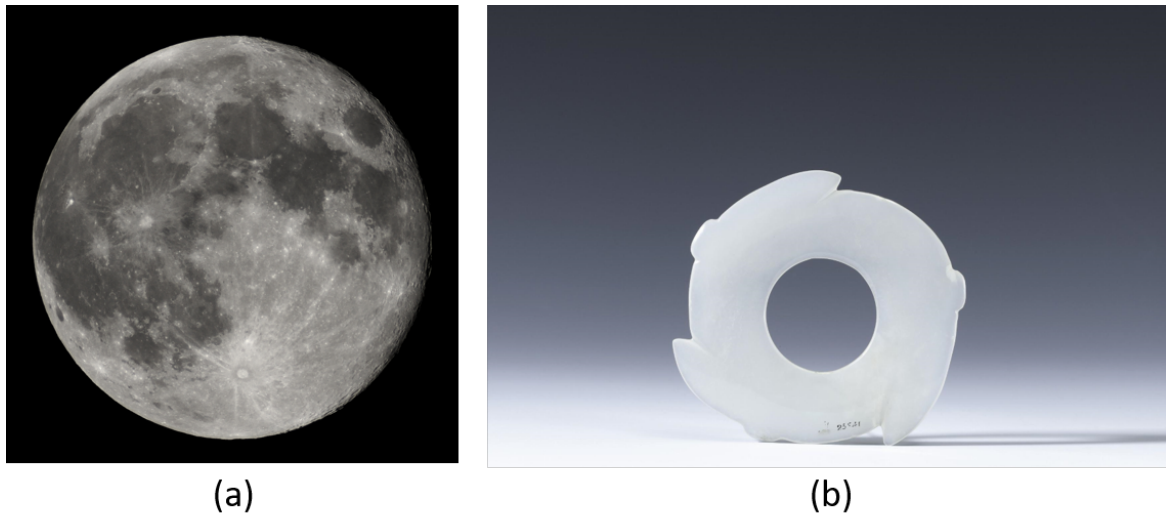


Fig. 1.1 (a) Lunar Surface and (b) Xuanji used to observe celestial bodies in ancient times [1]

people used a jade ware called Xuanji to observe the movement of celestial bodies and determine the four seasons.

Among the many celestial bodies that humans observe, the moon is undoubtedly one of the most familiar celestial bodies. The moon is called lunar, and it illuminates the earth day and night together with the sun. People worship the moon so much that the legend of the lunar deities is spread among many ancient religions in the world.

The exploration of the moon has also brought a lot of knowledge to mankind. In agricultural civilization, due to the observation of the moon, people have concluded the lunar calendar, which has achieved a huge contribution to the economic development of agricultural society. During the Renaissance, Galileo Galilei observed the moon through a telescope and discovered the unevenness of the surface of the moon, which rewritten the understanding of the celestial bodies since Aristotle. In 1687, Isaac Newton published the *Mathematical Principles of Natural Philosophy*, applied the motion of the moon to test the law of gravitation. It can be said, the emergence of modern science is inseparable from the observation of the moon.

After entering the 20th century, the rapid development of aerospace science and technology has brought mankind and the moon one step closer. On October 4, 1957, the Soviet Union successfully launched the first artificial satellite Sputnik 1. On September 12, 1959, the Soviet Union completed the hard landing of the Lunar 2












































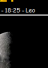
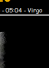
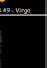
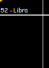


| Enero   | Febrero  | Marzo   | Abril   | Mayo   | Junio   | Julio  | Agosto   | Septiembre   | Octubre  | Noviembre  | Diciembre   |
|---|--|---|---|--|---|--|--|--|--|--|---|
| <br>5<br>JUEVES - 19.03 - Géminis      | <br>4<br>SÁBADO - 04.03 - Aries     | <br>5<br>DOMINGO - 13.03 - Tauro     | <br>3<br>LUNES - 18.03 - Géminis         | <br>3<br>MIÉRCOLES - 02.04 - Cáncer | <br>1<br>JUEVES - 12.04 - Leo        | <br>1<br>SÁBADO - 05.05 - Virgo       | <br>7<br>LUNES - 18.05 - Capricornio | <br>6<br>MIÉRCOLES - 04.06 - Acuario  | <br>5<br>JUEVES - 12.06 - Géminis       | <br>4<br>SÁBADO - 05.06 - Aries     | <br>3<br>DOMINGO - 16.07 - Tauro     |
| <br>12<br>JUEVES - 22.06 - Géminis     | <br>11<br>SÁBADO - 10.06 - Leo      | <br>12<br>DOMINGO - 18.06 - Virgo    | <br>11<br>MARTES - 25.06 - Virgo         | <br>10<br>MIÉRCOLES - 02.07 - Libra | <br>9<br>VIERNES - 13.07 - Ophiuchus | <br>9<br>DOMINGO - 04.08 - Sagittario | <br>15<br>MARTES - 03.08 - Tauro     | <br>13<br>MIÉRCOLES - 06.08 - Tauro   | <br>12<br>JUEVES - 12.08 - Géminis      | <br>10<br>VIERNES - 20.08 - Leo     | <br>10<br>DOMINGO - 26.09 - Tauro    |
| <br>19<br>JUEVES - 22.08 - Virgo       | <br>18<br>SÁBADO - 10.08 - Libra    | <br>20<br>LUNES - 18.08 - Sagittario | <br>19<br>MIÉRCOLES - 25.08 - Sagittario | <br>19<br>VIERNES - 02.09 - Acuario | <br>17<br>SÁBADO - 11.09 - Pieses    | <br>16<br>DOMINGO - 19.09 - Pieses    | <br>21<br>LUNES - 18.09 - Leo        | <br>20<br>MIÉRCOLES - 26.09 - Virgo   | <br>19<br>JUEVES - 18.09 - Virgo        | <br>18<br>SÁBADO - 15.09 - Libra    | <br>18<br>LUNES - 07.10 - Sagittario |
| <br>28<br>SÁBADO - 03.10 - Capricornio | <br>26<br>DOMINGO - 14.10 - Acuario | <br>28<br>MARTES - 02.10 - Géminis   | <br>26<br>MIÉRCOLES - 11.10 - Géminis    | <br>25<br>JUEVES - 19.10 - Tauro    | <br>24<br>SÁBADO - 11.09 - Orión     | <br>23<br>DOMINGO - 19.07 - Cáncer    | <br>29<br>MARTES - 07.09 - Escorpio  | <br>28<br>JUEVES - 02.10 - Sagittario | <br>27<br>VIERNES - 22.09 - Capricornio | <br>26<br>DOMINGO - 18.09 - Acuario | <br>26<br>MARTES - 04.10 - Pieses    |
|   |  |   |   |  |   | <br>30<br>DOMINGO - 19.04 - Virgo     |  |  |  |  |   |

Fig. 1.2 A Spanish Lunar Calendar for year 2017 [2]

detector on the lunar surface after many attempts, which is the first contact between artificial detector and the lunar.

During the same period, National Aeronautics and Space Administration (NASA) in the USA also conducted various of exploration of the universe and the moon. Thor-Able 1 was launched on August 17, 1958 as the first artificial satellite to target the moon in human history. After the near-month flight and landing experiments of multiple satellites, on July 16, 1969, Apollo 11 was launched into space, and humans landed on the moon for the first time.

At this time, aerospace technology has undergone considerable development. In order to better carry out lunar exploration missions, artificial detectors and astronauts need special vehicles that can travel on the surface of the moon. In consequence, on November 17, 1970, the Soviet Union sent the first unmanned lunar rover in history to the moon.

Since then, the United States and China have successively sent the Apollo lunar rover and Yutu lunar rover to the surface of the moon. These lunar rovers are driven by electricity, powered by photo-voltaic cells. The lunar rover consists of a wheeled chassis and an instrument compartment. Because there is no atmosphere on the lunar surface, the temperature difference between day and night is huge. In order to ensure that various detection instruments are not destroyed due to low temperature on the moon night, an insulating material is needed to wrap the instrument compartment, namely Multi-Layer Insulation (MLI) [9].

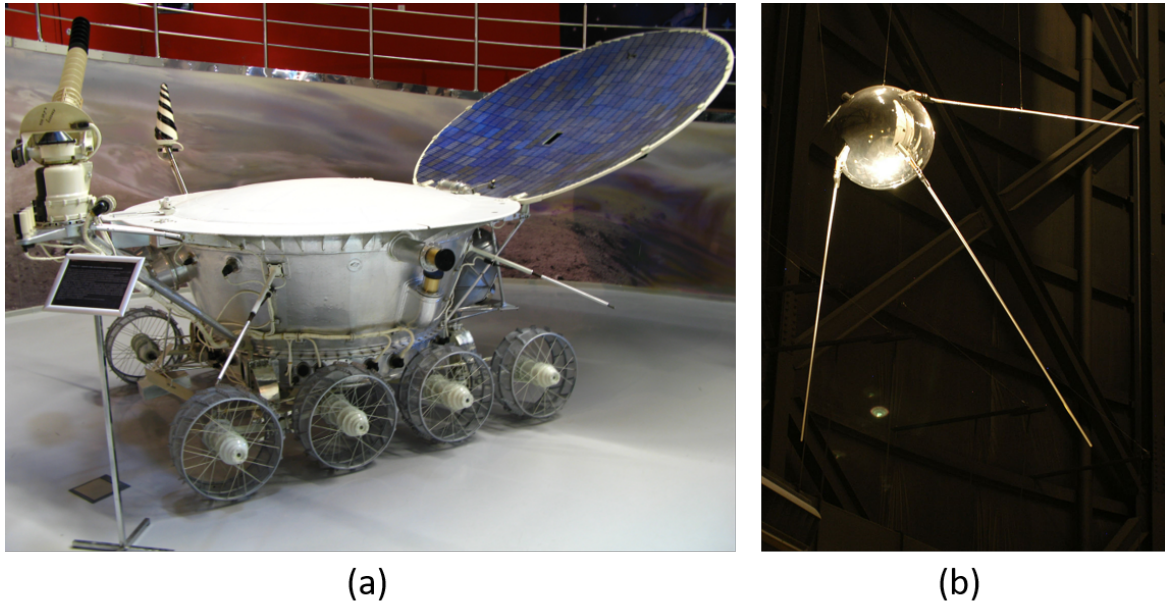


Fig. 1.3 (a) Russian Lunar Rover and (b) Sputnik1 [3]

Utilizing the characteristics of the Lunar environment as vacuum, and there is no thermal convection and thermal conduction in vacuum heat transfer, MLI is manufactured by Aluminized Mylars to reflect heat radiation. After multi-layer reflection, MLI can achieve almost complete heat insulation effect in vacuum compared to the insulation materials on the earth. Thus with MLI, thermal isolation of most Lunar Rover surface area can be achieved.

However, MLI cannot be used for thermal insulation of solar cells because of its radiation-shielding properties. In addition, the lunar rover body and solar cells are not without heat conduction. Through wires, a large amount of heat will be lost to the solar cells on the lunar night.

In order to avoid heat leakage through wires, novel lunar rover structure was proposed in recent researches applying Wireless Power Transfer (WPT) to replace the wire [10]. This research focus on the optimization of the Lunar Rover WPT system.

### 1.1.2 Wireless Power Transfer

In general, wireless power transfer have several categories. Microwave Power Transfer and Laser Power Transfer are far field wireless power transfer methods. Due to present cost-effectiveness disadvantages, far field WPT still has a long way to go, but the prospects are bright.

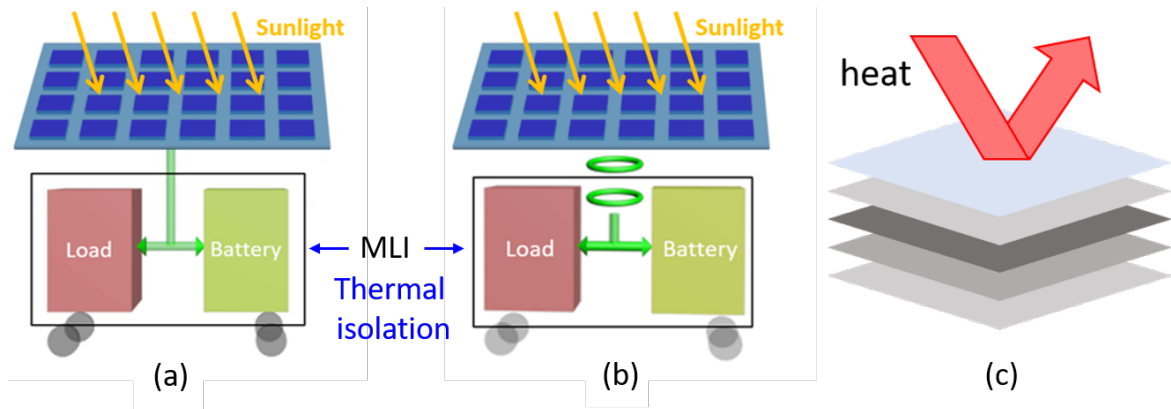


Fig. 1.4 (a) conventional Lunar Rover structure and (b) Lunar Rover WPT system structure (c) MLI structure [4]

Inductive Power Transfer (IPT) is most widely applied in the daily life, applying alternative current to coils to transfer electricity by alternative magnetic field. Capacitive (CPT) Power Transfer instead, transfer power through electric field, applying capacitors (such as metal plates). Both of them are able to achieve higher efficiency and transferred power by applying compensation. For IPT coils, compensation is applied by resonant capacitors at operation frequency, in this scheme, the IPT is called resonant wireless power transfer. In this thesis, the resonant IPT system is discussed. In the following text, WPT refers to resonant IPT.

It is believed that wireless power transfer was first proposed by Nicholas Tesla, and there have been many experiments since the 19th century. In the literature at that time, the use of capacitor and inductor to generate high-frequency alternating current, and the power transfer experiment through the magnetic field coupling already exists.

Because there was no power electronic switch technology at that time, the generation of high-frequency alternating current was slightly inconvenient. Moreover, without power electronic switches, it is difficult to adjust the frequency and duty cycle, which consequently increased the control difficulty of the circuit. The author of this thesis speculates that these may be the reasons why WPT had not widespread at that time.

Nowadays, the technology that applies semiconductor circuit components often used in electronic circuits to power systems, namely power electronics technology, has made considerable progress.

In 1874, Karl Braun discovered the rectifying ability of crystals, thus the first diode is invented. Starting from diode, to transistors and thyristors, the turn-on and



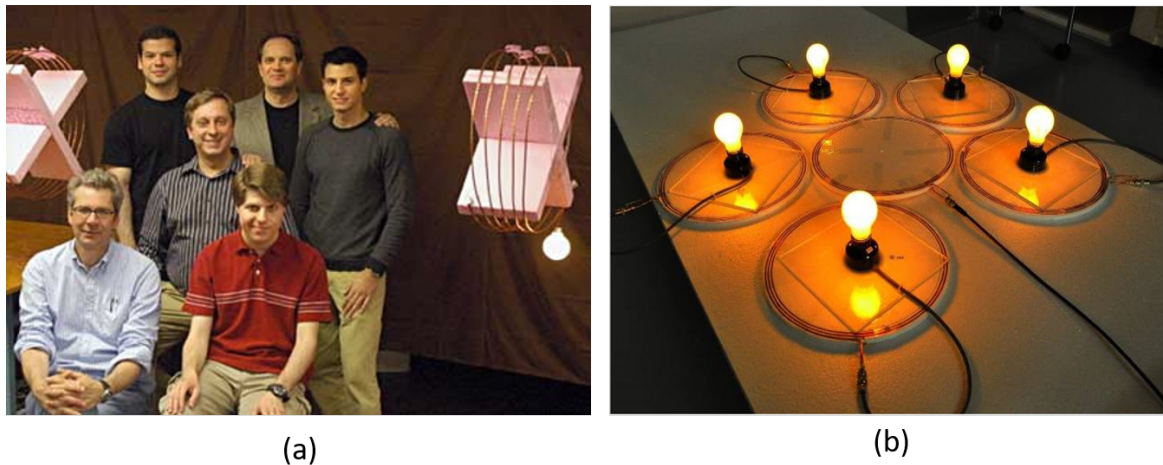


Fig. 1.5 (a) 2-m 60 watt self-resonant WPT experiment by MIT [5] (b) WPT illustration experiment by Hori-fujimoto Laboratory

turn-off of semiconductor components gradually become controllable. Nowadays, the popularization of fully-controlled switching components such as Metal-oxide-semiconductor field-effect transistor (MOSFET) and Insulated-gate bipolar transistor (IGBT) in power electronic systems makes it easier to implement high-frequency circuits required for wireless power transfer, as well as the selection of operation conditions. As a result, WPT technology has once again become a research hotspot.

At the end of the 20th century and the beginning of the 21st century, some researchers have done pioneering work in the field of inductive WPT. The John Talbot Boys team [11] from the University of Auckland has made innovative research for resonant wireless charging. Based on these results, Japan's Daifuku Company has realized the world's first non-contact power supply and transmission system at the year 1993. In 2004, based on circuit theory, the resonant frequencies of several common compensation typologies were analyzed. As well as an important phenomenon in WPT, namely frequency splitting phenomenon.

In 2007, a research team led by Marin Soljacic, professor of physics at the Massachusetts Institute of Technology (MIT), published a resonant wireless charging technology [5] in the *Science* journal. In this article, coupling mode theory is used to explain the phenomenon of WPT through resonance, and it is pointed out that the efficiency of WPT system can be optimized through load matching. Although this article is not limited to IPT systems, since magnetic field resonance is relatively easy to implement, an exemplary 2-meter 60-watt WPT experiment was implemented at the self-resonant frequency of the coils.



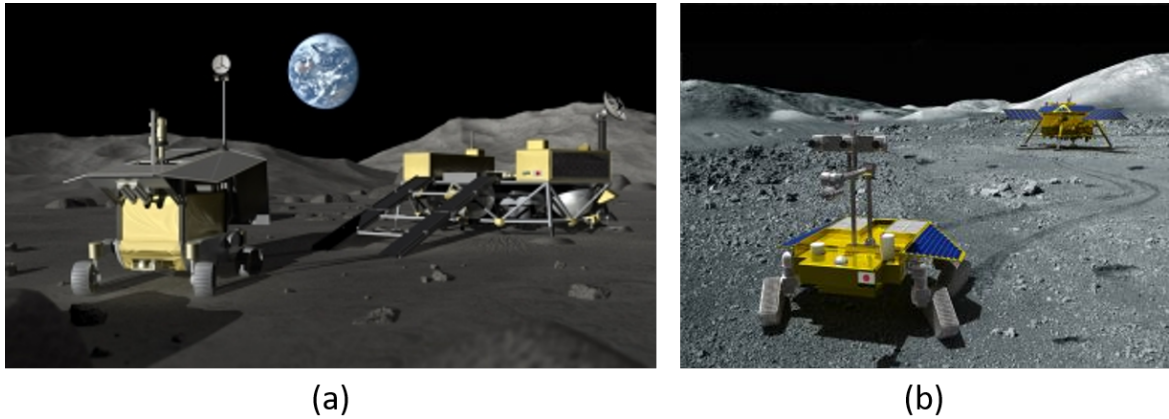


Fig. 1.6 (a) Mission plan for Lunar south polar exploration and (b) JAXA's Lunar rover prototype

After 2010, the design and control of the WPT system has undergone considerable development. For optimization of the WPT systems, laboratories such as Chunting Chris Mi team from San Diego State University, Professor Takehiro Imura from the Tokyo University of Science, John Kolar team from ETH zurich has made a lot of contributions [12–14].

Same period, researches on application of WPT are also not uncommon. Such as biomedical usages, portable devices, pulse charging of the electric vehicles and electric scooters, wireless in wheel-motors, hybrid unmanned aerial underwater vehicle [15–17]. Usually accompanied with the energy storage systems and power flow control, various applications combines WPT with different power electronics scenes [18, 19].

Inspired by these these application scenes, a system that combines WPT and Photo-voltaic (PV) cells, the Lunar Rover WPT system, is proposed recently [20]. In view of the uncertainty of PV output changes with ambient temperature and radiation intensity, the optimization of the WPT coil and frequency of this Lunar Rover WPT system has also become a new topic.

In section 1.2, the author of the thesis will briefly introduce the traditional and proposed WPT optimization methods and point out their advantages and disadvantages.

### 1.1.3 Lunar Rover Wireless Power Transfer System

For the reasons mentioned in section 1.1.1, the Japan Aerospace Exploration Agency (JAXA) is preparing for the next lunar rover mission to the moon [21]. For this

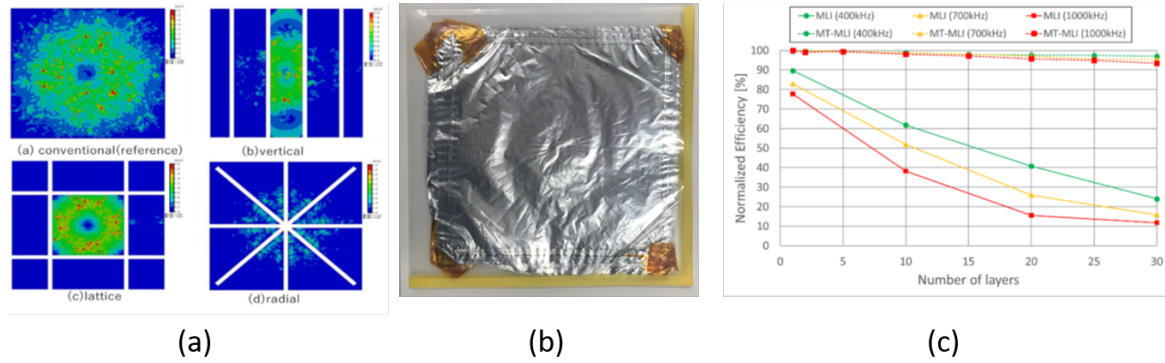


Fig. 1.7 (a) Magnetic simulation for magnetic trasmissive MLI (MT-MLI) and (b) MT-MLI prototype and (c) MT-MLI influence towards IPT efficiency [4]

reason, JAXA plans to use the WPT system to replace the wires to eliminate heat leakage caused by the heat conduction of the wires. For this purpose, JAXA designed the MT-MLI material that hardly interferes with the IPT system, and developed a prototype of the lunar rover WPT system.

As mentioned earlier, the principle of MLI is to use aluminized film to reflect heat radiation. Therefore, JAXA carves the material into radial slits [4], because there is almost no change in the reflection area for heat radiation, but the slits have a great influence on eddy currents. Therefore, this kind of MT-MLI achieves thermal insulation with almost no impact on WPT.

The system consists of PV panel as power source, class-D full bridge voltage driven inverter, WPT with series-series compensation topology, class-D current driven rectifier, DC-DC converter, load and another DC-DC converter to stabilize the DC-bus voltage through batteries [6]. In the optimization of the system, the real load as well as the second DC-DC converter to stabilize the DC-bus voltage, are equivalent to resistive load.

In order to simplify the structure of the primary side as much as possible due to thermal considerations in the Lunar rover WPT system, the DC-DC converter used for Maximum power point tracking (MPPT) is placed on the secondary side of the WPT [22].

In the next section, the author will briefly introduce the MPPT method of the system.

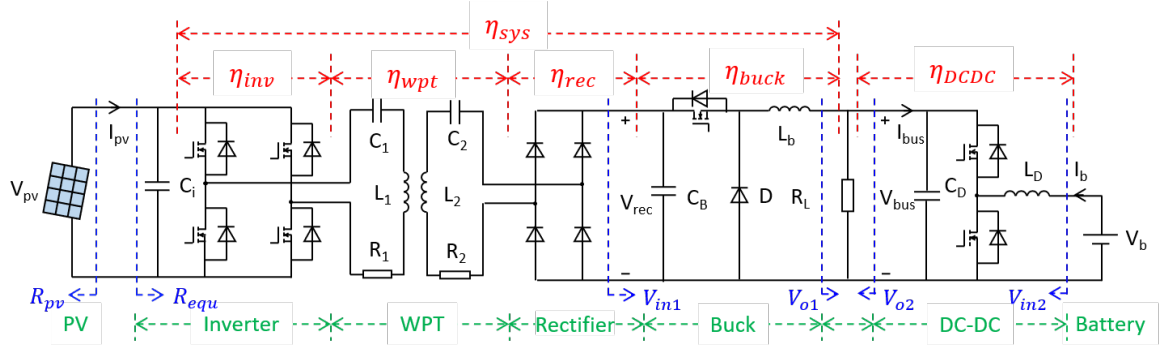


Fig. 1.8 Topology of the Lunar rover prototype [6]

### 1.1.4 Photo-voltaic Cell and Maximum Power Point Tracking

The principle of solar cells, the same as diodes, also comes from the PN junction. Doping the silicon crystal with the pentavalent element Phosphorus, because the five electrons in the outer layer of the pentavalent element are unstable, it is easy to form covalent bonds with surrounding atoms and lose one of the outer layer electrons, resulting in a high concentration of free electrons. Similarly, doping crystalline silicon with trivalent element Boron will form a high concentration of holes due to the lack of one electron in the outer layer.

When we combine these two silicon crystals with impurities, electrons and holes will diffuse to each other silicon crystal, This produces a built-in electric field. If we connect it to an external circuit, a current can be generated, which is called drift current.

When photons from outside enter the PN junction, they can provide energy for the outer electrons, thereby increasing the concentration of electron-hole pairs. As a result, the drift current will increase with the light intensity.

This is how solar cells generate electricity. As a result, the volt-ampere characteristic curve of the solar cell will be a reverse diode volt-ampere characteristic curve after being raised by a radiation-dependent drift current.

This shows that the output of the solar cell changes with the resistance of the external circuit. If we connect multiple such PN junctions in series or in parallel, when the parallel PN junctions are partially blocked, the output voltage of this parallel branch will decrease, causing it to fail to output. In this case, the output of the solar cell will appear multi-peak characteristics.

As consequence, conventionally a DC-DC converter is needed to adjust the input resistance of the photo-voltaic cell.

Traditional MPPT is generally implemented through adjusting the duty of the DC-DC converter to adjust the impedance of the load. There are already many MPPT algorithms, such as Perturb and observe algorithm [23], Constant voltage tracking [24], etc.

In previous studies on the lunar rover system, MPPT algorithms based on particle swarm optimization have been proposed. Comparing to conventional MPPT control, PSO has an advantage of searching for global best position in a multi-peak output curve. Several modification for PSO has been done for the improvement of searching speed.

However, previous studies did not consider the optimization of system efficiency, and ignored the frequency splitting phenomenon of resonant WPT.

Therefore, while optimizing the system, we also took the movement of the resonance frequency into account, and proposed two MPPT methods that not only change the duty cycle of the DC-DC converter, but also change the WPT frequency at the same time. And optimized on this basis. These methods will be explained in detail in Chapter 2.

## **1.2 Lunar Rover WPT Frequency and Coil optimization background**

Previous lunar rover WPT system uses 85kHz frequency and un-optimized coil, the PV-load efficiency of the previous prototype is only 75 percent at about 50 watt operation power, which means there will be 25 percent power dissipated in the circuit [6]. These facts shows necessity in optimization. In space, there is no restrictions on frequency selection of WPT system. in order to improve the performance of Lunar Rover WPT system, this thesis focused on optimization of coil and frequency.

### **1.2.1 Design of WPT Coils and Frequency**

Nowadays, With the continuous development of WPT technology, regulations for WPT have been gradually developed. One of the example is the operation frequency of WPT. In many WPT designs, the operating frequency is often specified as a specific value. But for lunar rover application, restriction is in absence hence optimization of operation frequency and coil parameters is discussed in this thesis.

Numerous optimization methods have been proposed concerning WPT coils and frequency. Finite element analysis (FEA) for magnetic coupling and quality

factor (KQ Product) evaluation [14] is generally adapted to optimized maximum AC-AC efficiency. However, the design method ignores operation conditions of system. Numerical calculation [25, 16, 26] is more flexible, taking specified condition [25, 16] or DC-DC efficiency [26] in to consideration, but with relatively few design parameters. Optimization combining metaheuristic algorithms and numerical calculation enables simultaneous optimization of more design parameters [27] [28], however, the accuracy of numerical calculation comparing to FEA is relatively insufficient. Combination of exhaustive algorithm, FEA [14] and numerical modeling of circuit enables Pareto optimization under high accuracy, however, the expensive calculation cost limited its application to continuous design space.

Meta-heuristic algorithms is a sort of algorithms based on intuition or empirical construction, which can give a feasible solution to the problem at acceptable calculation cost. Such as Genetic algorithm (GA) [29], Particle swarm optimization (PSO) [30], Multi-objective evolutionary algorithm based on decomposition (MOEA/D) [31], Multi-objective particle swarm optimization (MOPSO) [32] are often used in optimization problems. In WPT optimization, they can be used as a method to search for the optimal solution in the design space.

In this thesis, single and multi-objective optimization based on meta-heuristic algorithms, combining the circuit calculation and FE models is proposed. Coil parameters under different frequency is generated by FE models, specialized calculations such as static DC-DC efficiency at Maximum power point tracking (MPPT) condition and frequency splitting phenomenon is conducted by numerical modeling, and searching for optimum design in the continuous design space is carried out by the proposed Logistic Particle Swarm Optimization.

However, it is worth pointing out that the optimal design of WPT coils has its prerequisites, that is, the need to understand relatively certain circuit working conditions. However, for PV-WPT systems, the output of PV varies with the environment. So next, the author of the thesis will briefly introduce the circuit composition of the Lunar Rover WPT system, and the specific modeling and working status analysis will be completed in chapter 2 and 3.

## 1.2.2 Specialized Characteristics in Lunar Rover WPT Design

### Frequency optimization background with MT-MLI

There are already researches focusing on eddy current loss in the frequency optimization of the WPT coils, however, none of these researches considered the case of

metal materials between two coils. The frequency optimization in underwater WPT systems for autonomous underwater vehicles [16] is similar to this case. Because the power loss caused by sea water between the transmitter and receiver coil is generated by the eddy current inside the seawater, which is similar to a metal materials. In references [16, 33–35] the eddy current loss in the seawater have been analysed. The most precise calculation for occasions with ferrite and without ferrite are proposed in the reference [16] and [33], respectively. But there are certain difference between water and metal materials. Furthermore the recent researches for under-water WPT frequency optimization haven't considered the frequency-dependant variation of copper loss of the coils, compared to the eddy current in sea water.

Taking the MLI materials into consideration, this section investigated the WPT system property of a Qi [36] coil WPT system with frequency variation. Analysis has been carried out to explain the frequency-dependent influence of the system, and an electrical model based on the theoretical analysis as well as ordinary linear squared (OLS) regression has been established to calculate the optimal frequency of WPT systems with MLI materials. In further studies, the analysis method and regression model can be used to conduct the closed-form formulas of optimal resonance frequency for general WPT systems with metal materials placed between different coils. This proposed model will be presented in chapter 2, and the application of the measured data will be present in chapter 4 and 5.

### **DC-DC efficiency evaluation constraints of PV-WPT system**

For the PV-WPT system of the lunar rover, in the process of optimizing considering DC-DC efficiency, the output characteristics of the PV are inevitably involved, as well as Maximum power point tracking (MPPT).

The optimization of this thesis does not pay attention to dynamic efficiency, so the duty sweep method is adopted for MPPT for the optimization conditions when calculating DC-DC efficiency in Chapter 4 and 5.

For WPT resonant circuits, changing the equivalent impedance of the secondary side may cause frequency splitting [37]. In view of the optimization of the coil parameters in this thesis, air-gap is also used as a design parameter, and the effect of frequency splitting on efficiency is particularly important, so it is included in the scope of comparison. In the design of this thesis, when frequency splitting occurs, in accordance with the processing practice of WPT researches [38], in order to reduce high-order harmonics and ensure that the inverter current lags behind the voltage,

the optimizations for DC-DC efficiency in this thesis uses the upper resonant point as the operating frequency.

In addition to the proposed optimization of MPPT-DC-DC efficiency, for the purpose of evaluating JAXA's coil design, as an real application of the proposed coil design method, in Chapter 6, referring to conventional methods,  $KQ$  product and  $S_{21}$  are also used as cost function in the optimizations.

### 1.3 Thesis Outline

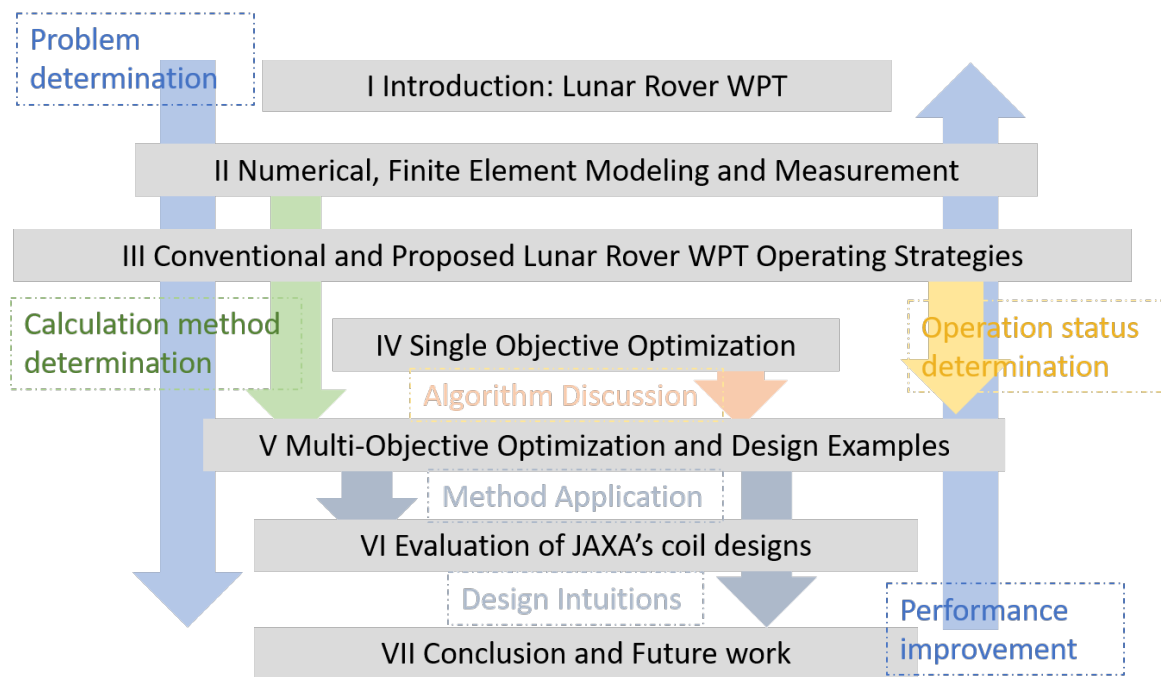


Fig. 1.9 Thesis Flowchart

In the second chapter, we will build a half-mathematical half-FE model for the PV-WPT system. The loss calculation formula used in subsequent calculations, the verification of the calculation methods, will all be introduced in Chapter 2.

In Chapter 3, we will introduce the proposed MPPT method. And the experimental results of MPPT will be presented in this Chapter. The operation strategies proposed in Chapter 3 will be used in the operation status determination in optimization process.

In Chapter 4 and 5, based on the calculations in Chapter 2 and MPPT methods in chapter 3, we will combine the finite element analysis and the meta-heuristic

algorithm to optimize the frequency and the coil of lunar rover WPT system with single and multi-objectives. Design intuitions from the algorithms will be discussed. Design example will be presented, and experiment verification of proposed method will be introduced.

Moreover, as an example of application of this thesis, the coil optimization experiment conducted by JAXA and the explanation of the experimental results using the Pareto optimization proposed in chapter 5 will be discussed in Chapter 6.



## Chapter 2

# Chapter 2 Lunar Rover WPT Numerical, Finite Element Modeling and Measurement

This chapter will introduce the traditional numerical modeling methods for PV output characteristics, series-series WPT circuit, inverter and rectifier loss evaluation methods and DC-DC converter efficiency estimation methods.

The modeling of frequency splitting phenomenon of the WPT circuits and the efficiency evaluation method based on the s-domain admittance will be introduced. In the authors' point of view, the calculation based on admittance will be benefit for efficiency evaluation at frequency splitting condition, although the calculation methods are traditional, the application into WPT efficiency evaluation is still in absence, as most papers model the circuit at fixed operation frequency.

Moreover, in this chapter, the measurement for WPT coils mini-model with MLI material by VNA (vector network analyzer) will be introduced.

In addition, the finite element model based on software FEMM [39] will be introduced, calculation method combining numerical and FE model for AC resistance, as well as the comparison between the FE model and measurement will be introduced.

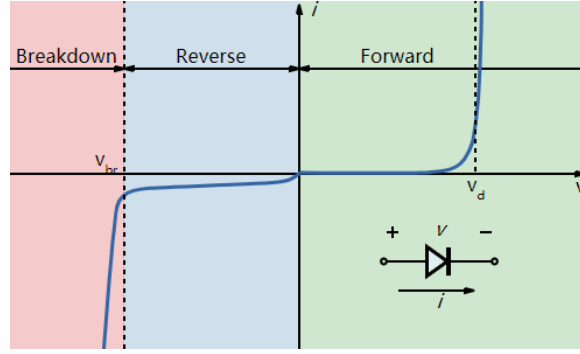


Fig. 2.1 Diode model V-I Characteristics [7]

## 2.1 PV Characteristics Modeling and Parameter Estimation

Because the lunar rover WPT system uses PV as the power source. In order to pave the way for proposed calculation and operation methods, the author will briefly introduce the output characteristics of solar cells (PV) in this section.

As mentioned in the previous section 1.1.4, the principle of PV comes from the characteristic that the drift current of the PN junction changes with the radiation intensity.

We know from semiconductor physics that the volt-ampere characteristic curve of diode can be described by the Shockley ideal diode equation (formula 2.1). Which is shown in Fig. 2.1.

$$I_D = I_o \left( e^{\frac{V_D}{nV_T}} - 1 \right) \quad (2.1)$$

Where  $I_D$  is the diode current,  $I_o$  is the reverse bias saturation current,  $V_D$  is the voltage across the diode and  $n$  is the ideality factor and the  $V_T$  is the thermal voltage, which can be derived from equation 2.2.

$$V_T = \frac{kT}{q} \quad (2.2)$$

Where  $k$  is the boltzmann constant,  $T$  is the temperature in Kelvin, and  $q$  is the magnitude of charge of an electron.

If we reverse the diode direction in Fig. 2.1 and add the aforementioned current controlled by the radiation intensity, as shown in Fig. 2.2, the breakdown and reverse part in Fig. 2.1 will be flipped to the right half plane and raise by  $I_{ph}$ , the V-I curve is shown in Fig. 2.3.

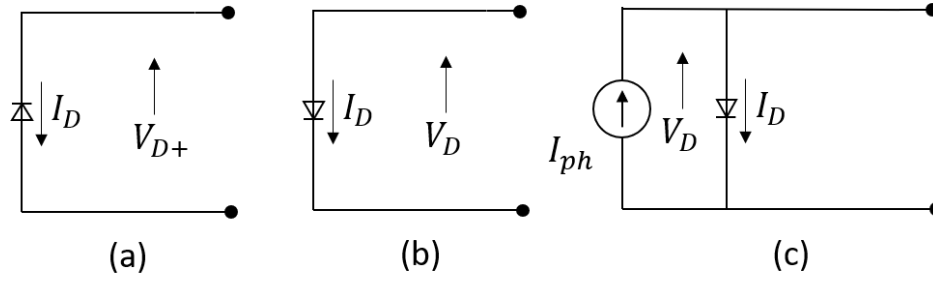


Fig. 2.2 (a) Diode (b) Reversed Diode (c) Diode and Photo current produced by radiation

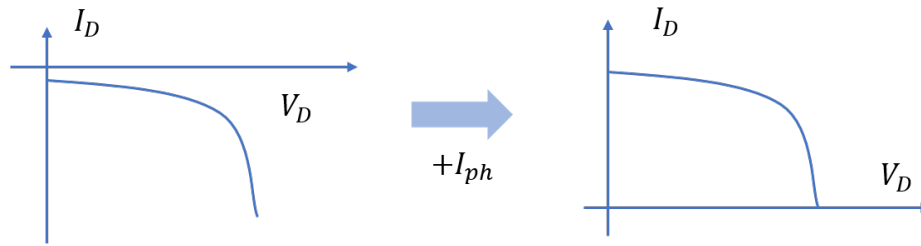


Fig. 2.3 Derivation of the PV output curve

For the actual PV, it is necessary to add series and parallel equivalent resistances to the model to obtain the equivalent circuit in Fig. 2.4. From the equivalent circuit, one can derive equation 2.3 to 2.6.

$$I_{ph} = [I_{sc} + k_i \cdot (T - 298)] \cdot \frac{G}{1000} \quad (2.3)$$

Equation 2.3 is the Photo current generated by light radiation. Where  $I_{sc}$ ,  $k_i$ , and  $G$  is the short-circuit current, thermal dependence factor, and solar radiation intensity for the modeled PV module, respectively. As the nominal radiation and temperature is  $1000 \text{ Watt/m}^2$  and  $298 \text{ K}$  in data-sheet, this equation means the photo current is proportional to radiation, and the temperature influence can be estimated linearly.

$$I_0 = I_{rs} \cdot \left( \frac{T}{298} \right)^3 \cdot \exp \left[ \frac{q \cdot E_{go} \cdot (1/298 - 1/T)}{n \cdot k} \right] \quad (2.4)$$

Equation 2.4 is the saturation current of Diode model. Where  $E_{go}$  is the semiconductor band gap energy, with a magnitude of about  $1.1 \text{ eV}$  for silicon.  $I_{rs}$  is the reverse saturation current, which can be calculated by equation 2.5.

$$I_{rs} = \frac{I_{sc}}{e^{\left( \frac{q \cdot V_{oc}}{n \cdot k \cdot T} \right)} - 1} \quad (2.5)$$

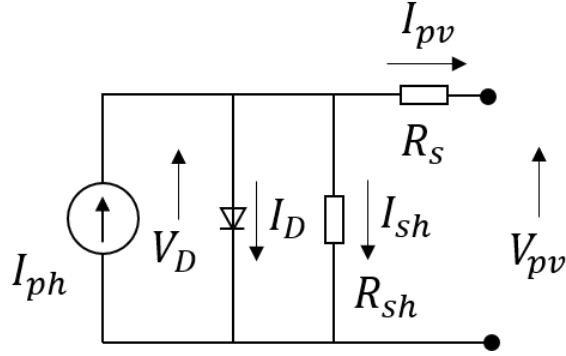


Fig. 2.4 Equivalent model for PV

Finally, with the equations from equivalent circuit and material science above, the output of a PV can be modeled as equation 2.6.

$$I = I_{ph} - I_0 \cdot \left[ \exp \left( \frac{q \cdot (V_{pv} + I_{pv} \cdot R_s)}{n \cdot k \cdot T} \right) - 1 \right] - I_{sh} \quad (2.6)$$

This equation is applied in the optimization algorithm when there's necessity to estimate the PV output. Note the equation as an algebraic loop, so the calculation in this thesis is based on iteration method. Furthermore, the parameters are estimated for the actual prototype of Lunar Rover.

In JAXA's plan, the Lunar Rover uses  $4cm \times 8cm$  PV module. With 17 in series and 8 in parallel, the modules produce about 130 Watt power at maximum power point in nominal condition. For the purpose of optimization, the actual PV properties is necessary, and several numerical estimations are applied to extract the parameters from the data sheet.

In the equations, the series and shunt resistance need to be estimated. The estimation method is shown in equation 2.7 and equation 2.8.

$$R_s = - \left. \frac{dV_{pv}}{dI_{pv}} \right|_{OC} - \frac{V_T}{I_{SC}} \quad (2.7)$$

$$R_{sh} = - \left. \frac{dV_{pv}}{dI_{pv}} \right|_{SC} \quad (2.8)$$

Where  $|_{OC}$  means at open-circuit condition,  $|_{SC}$  means at short circuit condition, respectively. From the experiment results of PV module carried out by JAXA [40], the estimated parameters in the numerical model are:  $R_s = 1.36\Omega$   $R_{sh} = 102.6248\Omega$ .

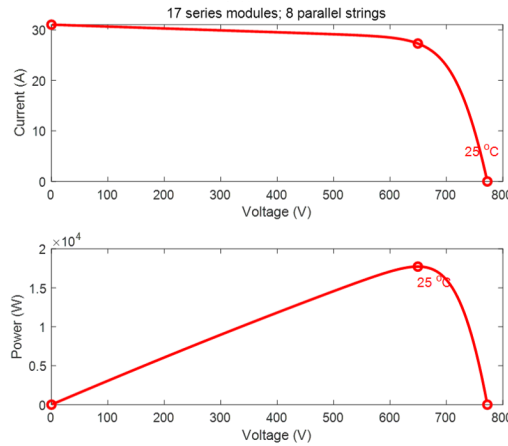


Fig. 2.5 Estimated PV propoerty of Lunar Rover WPT prototype

The overall output of PV is derived from the basic module by the superposition principle of voltage and current in the case of series and parallel connections, where  $V_{oc} = 45.441 \text{ Volt}$   $I_{sc} = 3.88 \text{ Ampere}$ . The rough property of estimated PV model is shown in Fig. 2.5. The properties are applied in design calculation.

In addition, as one can conclude from the numerical model above, the output property of PV is connected to the radiation and temperature. In consequence, connecting PV modules in series or parallel, once the partial shading condition happened, it may cause multiple peaks in output power curve. If one of the parallel module produced less voltage than the others because of the uneven distributed radiation, then the branch may be charged by the other branches. Which is called Hot-Spot issue in partial shading condition. To protect the modules at this condition, bypass diodes are applied into the scheme. Which caused the failure of components with insufficient output voltage.

As already mentioned in Chapter 1, to track the MPP of the PV output, both for one-peak situation and for partial shading conditions, there are already plenty of works presented. However, the PV plus WPT system, especially the topology positioning the DC-DC converter at secondary side of WPT, is still in absence. In this thesis, considering the WPT properties, specialized MPPT methods are presented in Chapter 3.

## 2.2 Conventional WPT Circuit Modeling

In Fig. 2.6 (a), the circuit topology for series-series WPT compensation is presented. In corresponds to four different series-parallel connection methods of the compensation

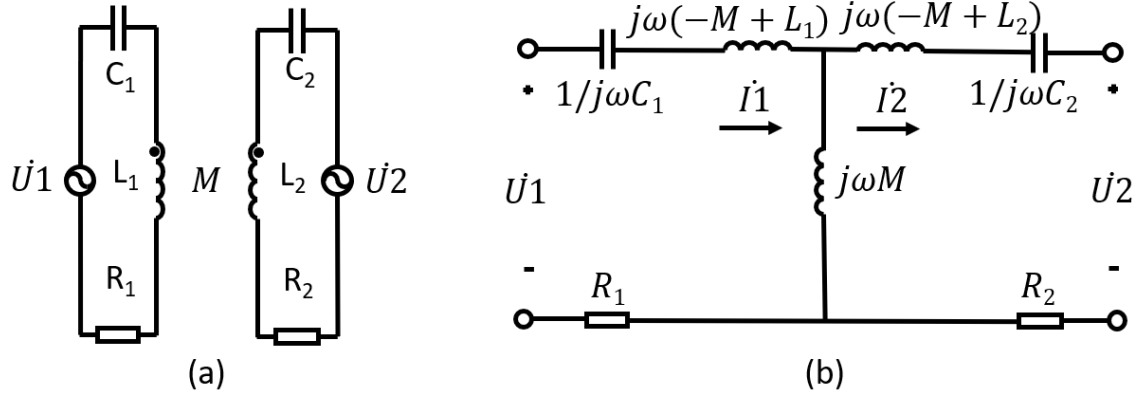


Fig. 2.6 Series-Series WPT Topology and the T-type equivalent Circuit

capacitor, there's four basic compensation typologies in WPT, series-series, series-parallel, parallel-parallel and parallel-series. In the Lunar Rover WPT system, series-series (S-S) topology is applied.

Mutual inductance  $M$  can be modeled using the T-type equivalent circuit, as the two topology has the same equations if we observe from the ports.

According to the circuit theory, the equations of the s-s topology can be expressed as equation 2.9.

$$\begin{aligned}\dot{U}_1 &= -j\omega M \dot{I}_2 + (R_1 + \frac{1}{j\omega C_1} + j\omega L_1) \dot{I}_1 \\ 0 &= \dot{U}_2 - j\omega M \dot{I}_1 + (R_2 + \frac{1}{j\omega C_2} + j\omega L_2) \dot{I}_2\end{aligned}\quad (2.9)$$

For resonant WPT, the operation frequency is chosen to eliminate the reactance of the circuit.

$$0 = \frac{1}{j\omega C_1} + j\omega L_1 = \frac{1}{j\omega C_2} + j\omega L_2 \quad (2.10)$$

Based on resonance, the circuit equations are:

$$\begin{aligned}\dot{U}_1 &= -j\omega M \dot{I}_2 + R_1 \dot{I}_1 \\ 0 &= \dot{U}_2 - j\omega M \dot{I}_1 + R_2 \dot{I}_2\end{aligned}\quad (2.11)$$

For active rectifying circuit, the phase difference between primary and secondary voltage determines the energy flow direction, for passive rectified system like Lunar Rover WPT prototype, following the assumption that the current driven rectifier has current and voltage in phase with each other [41], the secondary voltage is usually modeled as a pure resistor  $R_L$ .

$$R_L \dot{I}_2 = \dot{U}_2 \quad (2.12)$$

Therefore, by applying some algebraic transformations to the two formulas in formula 2.11, we can get equation 2.13 as the efficiency of the S-S topology.

$$\eta = \frac{\omega^2 M^2 R_L}{(R_2 + R_L)(R_1 R_2 + R_1 R_L + \omega^2 M^2)} \quad (2.13)$$

At this time, find the partial derivative of  $\eta$  with respect to  $R_L$ , and set the partial derivative equal to zero, one can get the matched impedance of the secondary side, and the maximum efficiency of WPT circuit.

$$R_{L-\eta \max} = \sqrt{R_2 \left( \frac{\omega^2 M^2}{R_1} + R_2 \right)} \quad (2.14)$$

$$\eta_{\max} = \frac{\omega^2 M^2 R_{L-\eta \max}}{(R_2 + R_{L-\eta \max})(R_1 R_2 + R_1 R_{L-\eta \max} + \omega^2 M^2)} \quad (2.15)$$

Another method to express the maximum efficiency equation is through the quality factors and magnetic coupling.

$$\eta_{\max} = \frac{k^2 Q^2}{(1 + \sqrt{1 + k^2 Q^2})^2} \quad (2.16)$$

Where

$$k = \frac{M^2}{\sqrt{L_1 L_2}} \quad (2.17)$$

$$Q = \sqrt{Q_1 Q_2} \quad (2.18)$$

From equation 2.15, one can obtain the most widespread design principle for WPT system, namely  $KQ$  product optimization. Since the theoretical maximum efficiency of WPT circuit is the function of  $KQ$ , and maximizing  $KQ$  has totally the same effect of maximizing the theoretical maximum efficiency. Measurement results in this thesis shows the theoretical maximum efficiency corresponds with the actual efficiency well, even if the system is not optimum-loaded. The measurement results will be presented in chapter 4 and 5. The conventional model is able to explain most of the phenomenons we face at design of WPT circuit, especially at perfect

compensation. However, there's a load-dependent phenomenon called frequency splitting that violate the rules [42].

## 2.3 Frequency Splitting Modeling and Efficiency Evaluation Method

For most load conditions, WPT system has only one peak in the efficiency curve, with operation frequency as independent variable. The reason is at the resonant frequency, both primary and secondary side reactance can be eliminated.

However, since the equivalent impedance of the secondary side reflecting on the primary side is a frequency-magnetic coupling and load dependent multi function, there is possibility of other resonant points if we look at the primary side. When the other resonant points exists, there's possibility for invalidation of the fundamental wave hypothesis, which is the prerequisite of the conventional modeling method.

Frequency splitting phenomenon is the most important phenomenon for the WPT circuits, in this section, the modeling of it will be introduced.

For simplification, symmetric coil is considered in this section. For the s-s topology, if we assume  $j\omega L + \frac{1}{j\omega C} = jX$ ,  $jX + R = Z$  and  $L_2 = L_1 = L$ ,  $R_2 = R_1 = R$ ,  $C_2 = C_1 = C$  for symmetric coils, there will be:

$$\begin{aligned}\dot{U}_1 &= -j\omega M \dot{I}_2 + Z \dot{I}_1 \\ 0 &= -j\omega M \dot{I}_1 + (Z + R_L) \dot{I}_2\end{aligned}\tag{2.19}$$

For the equivalent impedance if we look from the primary side WPT, there will be:

$$Z_{eq} = Z + \frac{M^2 \omega^2}{Z + R_L}\tag{2.20}$$

For resonance, the imaginary parts in this equation should be zero, thus there is:

$$\text{Im}(Z_{eq}) = X - X \frac{M^2 \omega^2}{(R + R_L)^2 + X^2}\tag{2.21}$$

And the solutions of this equation can be derived as:

$$X = 0\tag{2.22}$$



$$\omega_{1,2} = \sqrt{\frac{2L - C(R + R_L)^2 \pm \sqrt{4M^2 + C^2(R + R_L)^4 - 4LC(R + R_L)^2}}{2C(L^2 - M^2)}} \quad (2.25)$$

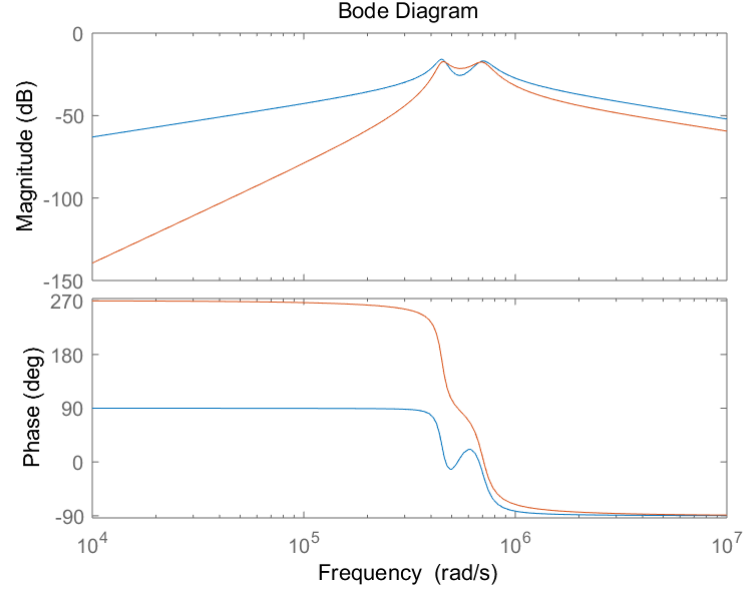


Fig. 2.7 Primary(blue) and Secondary(orange) Admittance Example

or:

$$(R + R_L)^2 + X^2 - M^2\omega^2 = 0 \quad (2.23)$$

For  $X = 0$  situation, the solution is the natural frequency, which is often selected as the operating frequency.

$$\omega_0 = 1/\sqrt{LC} \quad (2.24)$$

However, for equation  $(R + R_L)^2 + X^2 - M^2\omega^2 = 0$ , there is also possibility of having real solution, which is shown in equations.

Criterion of splitting in symmetric S-S topology is derived as:

$$4M^2 + C^2(R + R_L)^4 - 4LC(R + R_L)^2 > 0 \quad (2.26)$$

In order to evaluate the WPT circuit efficiency at the frequency splitting situation, which is unavoidable in MPPT conditions, it is proposed to use admittance in s-domain to model the WPT circuit and applying frequency response at  $\omega_2$  to calculate the precise circuit properties. From the circuit equations, one can conclude:

$$\dot{I}_1 = \frac{(R_L + z_2) \dot{U}_1}{z_1 z_2 + c_1^2 M^2 + z_1 R_L} = Y_1 \dot{U}_1 \quad (2.27)$$

$$\dot{I}_2 = \frac{j\omega M \dot{U}_1}{z_1 z_2 + \omega^2 M^2 + z_1 R_L} = Y_2 \dot{U}_1 \quad (2.28)$$

Where symmetric design is considered:

$$z_1 = z_2 = R_1 + sL_1 + \frac{1}{sC_1} = R_2 + sL_2 + \frac{1}{sC_2} \quad (2.29)$$

The input and output real and reactive power can be conclude:

$$\dot{U}_1 (\bar{\dot{I}}_1) = |\dot{U}_1|^2 \operatorname{Re}(Y_1) - j |\dot{U}_1|^2 \operatorname{Im}(Y_1) = P_1 + jQ_1 \quad (2.30)$$

$$\dot{U}_2 (\bar{\dot{I}}_2) = R_L \cdot |\dot{U}_1|^2 |Y_2|^2 = P_2 \quad (2.31)$$

And proposed equation to calculate efficiency will be:

$$\eta_{wpt} = \frac{P_2}{P_1} = R_L \cdot \frac{|Y_2|^2}{\operatorname{Re}(Y_1)} = R_L \cdot \frac{|Y_2|^2}{|Y_1| \cos \varphi_1} \quad (2.32)$$

Note that current driven rectifier is considered in this thesis, which means the secondary voltage and current is in phase, with a ratio of  $R_L$ . For active rectification, the equation can be rearranged according to secondary voltage.

One of Bode diagram of design example is shown in Fig. 2.7 It is observed that splitting happens.

## 2.4 Other Loss Evaluations

This section introduce the calculation methods for the rest part of the Lunar rover WPT system. Including the inverter, rectifier and converter.

### 2.4.1 Voltage Driven Inverter

As for the inverter loss, the working frequency is still one of the decisive factors, so it is necessary to consider the WPT part and inverter loss at the same time. Corresponding to the SS topology of WPT, series resonant class D inverter is often

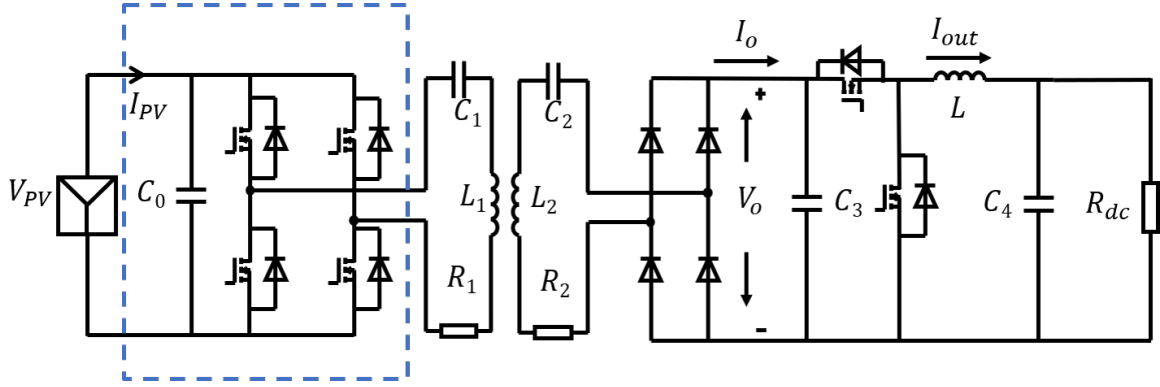


Fig. 2.8 Class-D full bridge inverter as an example

used. In this section, a full bridge series resonant class D inverter is used as an example of WPT system operation frequency optimization.

It is worth noting that if the inverter works perfectly at resonance frequency, switching loss can be eliminated, but this is not practical. In most of the cases, it is assumed that the operating frequency of the inverter is slightly higher than the resonant frequency of the resonance loop, thus generating turn-off loss rather than turn-on loss. The advantage of operating above resonance is to realize zero voltage switching on, so it is not necessary to consider turn on loss and worry about the damage of MOSFET due to the reverse recovery of body diodes.

The loss of inverter  $P_{inv}$  can be divided into three parts: conduction loss  $P_{inv}$ , switching loss  $P_{toff}$  and driver loss  $P_{driver}$ . They are generated by the charge and discharge of the on equivalent resistance and the input and output capacitance of MOSFET, respectively.

$$P_{inv} = P_{rds} + P_{toff} + P_{driver} \quad (2.33)$$

In order to avoid the high nonlinear input and output capacitance, the rise time of the voltage  $t_r$  and fall time of the current  $t_f$  is applied to calculate the turn-off switching loss [41]. Since the rise of voltage is approximately quadratic function and the current is approximately linear function, we can get the following formula of turn off switching loss as follows.

$$P_{toff} = 8f(t_r/3 + t_f/2)U_1I_1\sin\theta \quad (2.34)$$

Where  $\theta$  is the phase difference of current lag voltage in resonance circuit. Secondly, the charge of gate input capacitor of MOSFET is used to calculate the

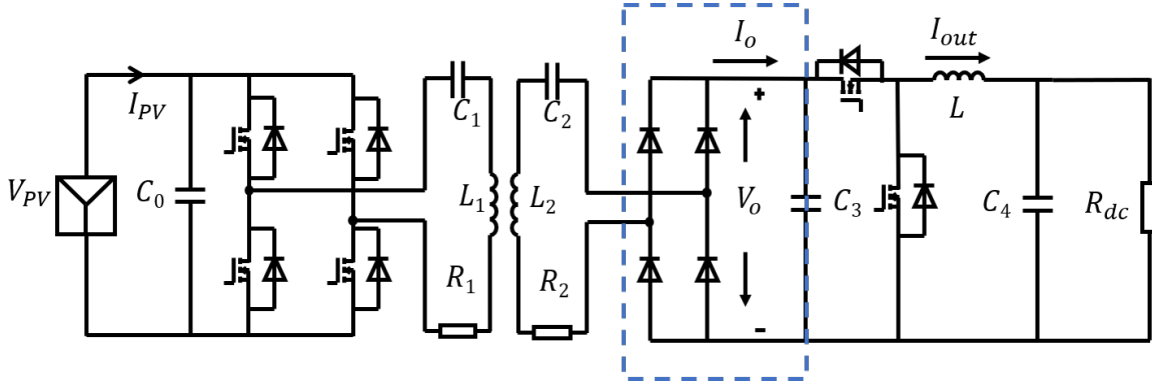


Fig. 2.9 Class-D current driven rectifier as an example

driver loss when switching on and off. The current and voltage in this section is RMS value, for peak value, the equations can be divided by 2.

$$P_{driver} = 4fQ_gV_g \quad (2.35)$$

Where  $Q_g$  is the total charge of the gate driver and  $V_g$  is the difference between the peak points of the gate driver voltage.

Finally, since half of the four MOSFETs are in the on state and the equivalent resistance is  $R_{ds}$ , the conduction loss is described by the following equation.

$$P_{rds} = 2I_1^2r_{ds} \quad (2.36)$$

To sum up, for the lunar rover WPT system, the inverter loss can be described as the following formula.

$$P_{inv} = 2I_1^2r_{ds} + 8f(t_r/3 + t_f/2)V_oI_1\sin\theta + 4fQ_gV_g \quad (2.37)$$

### 2.4.2 Current Driven Rectifier

The full bridge rectifier connecting to resonant circuit is approximately modeled as current driven rectifier. The efficiency can be evaluated as [41]:

$$\eta_{rec} = \frac{P_o}{P_i} = \frac{1}{1 + \frac{2V_F}{V_o} + \frac{\pi^2}{4} \cdot \frac{R_F}{R_{out}} + \frac{r_c}{R_{out}} \cdot \left(\frac{\pi^2}{8} - 1\right)} \quad (2.38)$$

Where  $V_F$ ,  $R_F$  and  $r_c$  is the forward voltage, conduction resistance of diodes and the ESR of output filtering capacitor. The ratio  $\frac{\pi^2}{8} - 1$  is derived by integration of the AC part of the sine half wave from WPT circuit.  $R_{out}$  is the output resistance of

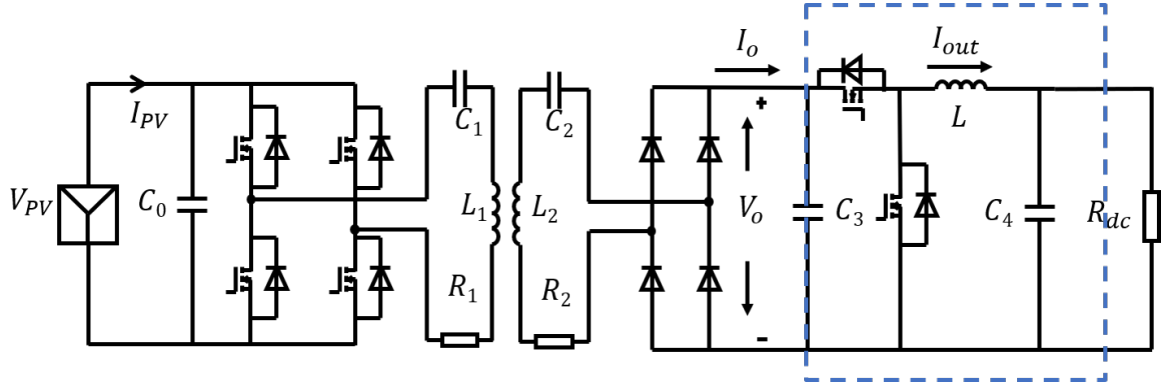


Fig. 2.10 Synchronous rectification type buck converter as an example

rectifier and  $V_o$  is the output voltage of rectifier. To do some simplification to connect the equation with WPT resonant circuit, one can apply the relationship between input and output voltage of the rectifier, to introduce  $R_L$  from the WPT circuit into the equation:

$$Mv_R = \frac{V_0}{V_{Rms2}} = \frac{\pi}{2\sqrt{2}}\eta_{rec} \quad (2.39)$$

$$R_{out} = \frac{V_0}{I_0} = \frac{\pi^2}{8}R_L\eta_{rec} \quad (2.40)$$

Then one can conclude:

$$\eta_{rec} = 1 - \left( \frac{8VF}{\pi V_{m2}} + \frac{2RF}{RL} + \frac{8rc}{\pi^2 RL} \times \left( \frac{\pi^2}{8} - 1 \right) \right) \quad (2.41)$$

It can be observed from this equation, that the rectifier efficiency is dependent on the secondary peak voltage of WPT circuit and the equivalent resistance of the WPT circuit.

### 2.4.3 DC-DC Converter

In the topology of Lunar rover WPT, secondary side DC-DC converter is used for MPPT. To calculate the efficiency of the WPT system, we consider the synchronous rectification type buck converter as example [43].

Several main aspects is considered in the estimation of dc-dc converter efficiency, including mosfet conduction loss  $P_{on}$  can be estimated by, where  $R_{ds}$  is the conduction resistance of MOSFET.  $V_{out}$  and  $V_{in}$  is the output and input voltage of the DC-DC

converter, respectively. The 1/12 ratio of the ripple current  $\Delta I_L$  is derived by the integration of squared ramp current.

$$P_{on} = \left[ I_{out}^2 + \frac{\Delta I_L^2}{12} \right] \times R_{ds} \times \frac{V_{out}}{V_{in}} \quad (2.42)$$

Where ripple current  $\Delta I_L$  is calculated by:

$$\Delta I_L = \frac{(V_{in} - V_{out})}{f_{dcdc} \times L} \times \frac{V_{out}}{V_{in}} \quad (2.43)$$

Where  $f_{dcdc}$  is the operation frequency of DC-DC converter, and  $L$  is the inductance of the buck inductor.

MOSFET switching loss  $P_{sw-dcdc}$  can be estimated by:

$$P_{sw-dcdc} = \frac{1}{2} \times (V_{in} + VF) \times I_{out} \times (t_r + t_f) \times f_{dcdc} \quad (2.44)$$

Where  $t_r$ ,  $t_f$  is the rise time of the voltage and fall time of the current, at the turn-off situation. These two parameters can be obtained by data-sheet. And the  $VF$  is the forward voltage of the body diode, since the current direction for the low side MOSFET is always same as the diode, zero-voltage switching is achieved.

Here we assumed linear variation of both voltage and current, we calculated the triangle area that the voltage and current coincident. However, for the real cases, if we assume a linear variation of current, the voltage variation across the equivalent capacitor of the MOSFET, should be the instantaneous integral of current, as the quadratic function of time, instead. Taking this phenomenon into consideration, there is another version of switching loss shown as:

$$P_{sw-dcdc} = (V_{in} + VF) * I_{out} * \left( \frac{t_r}{3} + \frac{t_f}{2} \right) * f_{dcdc} \quad (2.45)$$

Dead time loss, which sometimes can be ignored, estimated as:

$$P_D = V_F \times I_{out} \times (t_r + t_f) \times f_{dcdc} \quad (2.46)$$

Driver loss and the inductor loss:

$$P_G = Q_g \times V_{gs} \times f_{dcdc} \quad (2.47)$$

$$P_{L(DCR)} = \left[ I_{out}^2 + \frac{\Delta I_L^2}{12} \right] \times DCR \quad (2.48)$$

The major part of loss come from the integration of current of in and output capacitors, such as

$$P_{\text{cinloss}} = \left( D \sqrt{1-D} * I_{\text{out}} \right)^2 * r_c \quad (2.49)$$

The input capacitor loss  $P_{\text{cinloss}}$ , capacitor ESR  $r_c$  and the duty  $D$  depicts the loss of rectangular wave AC components into buck.

In addition, the output of dc/dc converter also consists ripple, which is filtered by the output capacitor.

$$P_{\text{closs}} = \frac{\Delta I^2}{12} * r_{\text{cbuck}} \quad (2.50)$$

The buck efficiency can be calculated by:

$$\eta_{\text{buck}} = \frac{V_{\text{out}} * I_{\text{out}}}{(V_{\text{out}} * I_{\text{out}} + P_{\text{on}} + P_{\text{sw}} + P_{\text{cinloss}} + P_{\text{ind}} + P_{\text{closs}})} \quad (2.51)$$

By far, we already obtained the detailed calculation methods of the DC-DC efficiency for the Lunar rover WPT. To further model the WPT coils and obtain the parameters, next section will introduce the method of relatively accurate estimation of the magnetic field and coil parameters, namely simulation based on FE models.

## 2.5 Half-FE models for Litz Wire Coil AC Resistance

The optimization of the coil involves the calculation of the magnetic field. However, most of the numerical analysis is based on the assumption of static magnetic field, inaccurately. In order to accurately analyze the magnetic field and calculate the WPT efficiency, the finite element analysis applied.

In chapter 4 and 5, taking consideration of computational cost, the open-source 2-D finite element analysis tool FEMM will be adopted and the symmetrical circular coil will be studied, application of meta-heuristic algorithms to coil design will be introduced. Every evaluation process of meta-heuristic algorithm comes from a finite element simulation.

Since for litz wire coils, the FE models sometimes produces inaccurate AC resistance results. The reasons are [25]:

- the length of Litz wire strands is not the same with total length of the wire due to the winding method inside the litz wire, in order to ensure that the center of each strand is symmetrical, the strands are curved inside.

- The heads of the strands of the litz line are connected to each other, so that each strand is not completely independent.
- The environment, especially the surrounding conductor and temperature, can affect the measurement of the AC resistance of the litz line to a considerable extent.

In the chapter 4 and 5, for AC resistance calculation of the litz wire, a half-numerical method is applied. The modeling methods are from Mühlethaler Jonas. For unit length of the litz wire coil, the skin effect and proximity effect can be estimated as [44]

$$p_{\text{skin}} = n \cdot R_{\text{dc}} \cdot F_{\text{R}}(f_0) \cdot \left(\frac{\hat{I}}{n}\right)^2 \quad (2.52)$$

$$p_{\text{prox}} = n \cdot R_{\text{dc}} \cdot G_{\text{R}}(f_0) \cdot \left(\hat{H}_{\text{e}}^2 + \frac{\hat{I}^2}{2\pi^2 d_{\text{a}}^2}\right) \quad (2.53)$$

Where the  $n$  is the number of strands in the litz wire coil,  $\hat{I}$  is the current peak value,  $\hat{H}_{\text{e}}$  represents the external magnetic field for each turn of the coil, it is estimated by the magnetic field at the center of the wire, calculated by the FE models.  $d_{\text{a}}$  is the diameter of the litz wire and the  $F_{\text{R}}(f_0)$  and  $G_{\text{R}}(f_0)$  are the operation frequency dependent factors. In addition, in the calculations, some empirical factors based on measurement are applied to the model, including inside  $F_{\text{R}}(f_0)$  and  $G_{\text{R}}(f_0)$ , to model the coils in corresponds to the measurement [25].

## 2.6 Regression Model for WPT with MT-MLI based on Measurement

The previous sections discussed the modeling of WPT system without MT-MLI consideration. For system with MT-MLI, the FE models based on the software femtet has already been presented by JAXA [4], however, the accuracy for MT-MLI modeling is still insufficient.

To obtain the effect of MT-MLI towards WPT efficiency and to optimize the frequency for Qi-A11 coils, as an example for coil design in Lunar rover WPT system, measurements has been carried out. A regression model is presented.

Previous researchers have done plenty of numerical models for frequency-dependent resistance of litz-wire coils. The frequency-dependent resistance of



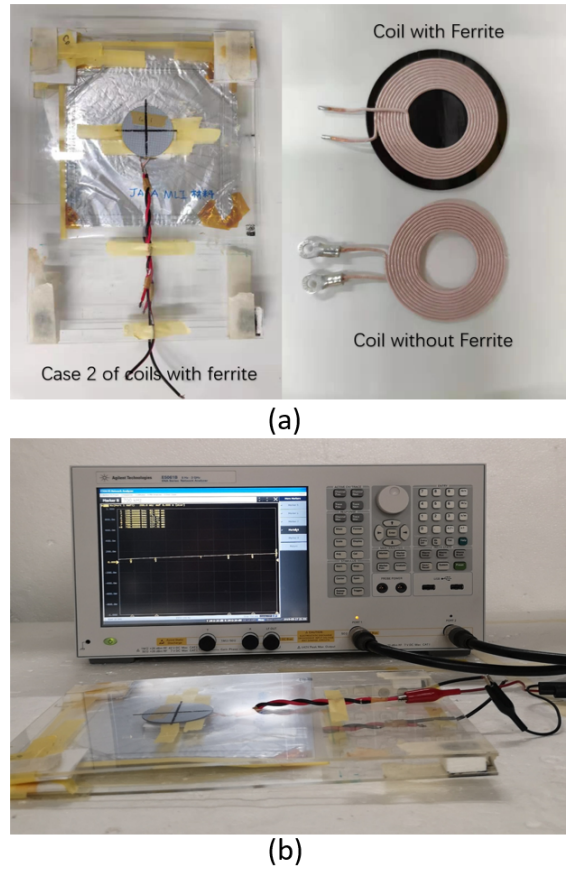


Fig. 2.11 Mini-model of measurement for Qi-A11 Coils with MLI

litz-wire coils consist of two parts: the conductivity resistance caused by net current and the proximity resistance caused by the eddy current inside the wires.

$$R(f) = R_{\text{cond}} + R_{\text{pr}} \quad (2.54)$$

For conductivity losses, according to previous researches, it can be concluded that when the radius of each strand  $r_s$  in litz wire is relatively small compared to the skin depth  $\delta$ , the skin effect can be ignored:

$$F_R = \frac{R_{\text{cond}}}{R_{\text{dc}}} \approx 1 + \frac{1}{48} \left( \frac{r_s}{\delta} \right)^4 \approx 1 \quad (2.55)$$

Where

$$\delta = \frac{\sqrt{2}}{\sqrt{\mu\sigma\omega}} \quad (2.56)$$

Where  $\mu$  is the permeability and the  $\sigma$  is the conductivity of the material.  $R_{cond}$  is the conductivity resistance of a unit length wire. It can be observed that for general litz-wire coils, the radius of each strand is small (For example the coils employed), the conductivity resistance is a constant when the coil is fixed.

For proximity effect, the eddy current loss per unit length inside an arbitrary coil caused by the alternating magnetic field will be proportional to frequency squared. [25]

$$P_j = \frac{\pi \gamma^4 H_j^2}{8\sigma} \quad (2.57)$$

Where

$$\gamma = \sqrt{2}r_s/\delta = r_s \sqrt{\mu\sigma\omega} \quad (2.58)$$

Under the circumstance of  $\gamma < 1$ ,  $P_j$  and  $H_j$  represent the power loss per unit length caused by proximity effect and H-field intensity of the  $j$ -th turn. Because the H-field intensity for  $j$ -th turn is proportional to the net current and the equivalent proximity resistance for a strand of unit length in the  $j$ -th turn is:

$$\begin{aligned} R_j &= \frac{P_j}{(I_{rms}/n_0)^2} = \frac{2P_j}{(I/n_0)^2} \\ &= \frac{2n_0^2 P_j}{I^2} \end{aligned} \quad (2.59)$$

Based on the analysis, The resistance caused by the proximity effect will be proportional to frequency squared. Thus the frequency-dependent regression model for litz wire coils is:

$$R(f) = R_{cond} + R_{pr} = k_{cond} + k_{pr}f^2 \quad (2.60)$$

Where  $k_{cond}$  is a constant, equals to the DC resistance.  $k_{pr}$  is another constant related to the magnetic field distribution of the coil. The calculation of the factors is out of scope for this section, detailed models are in reference [44].

But these conventional formulas cannot explain the increase of resistance caused by the MLI materials. So in this section, a novel electric regression model has been proposed by adding an equivalent resistance representing the MLI influence into the resistance model.

Because the power loss of eddy current for a certain conductor between transmitter and receiver coils can be obtained as follows [16, 45].

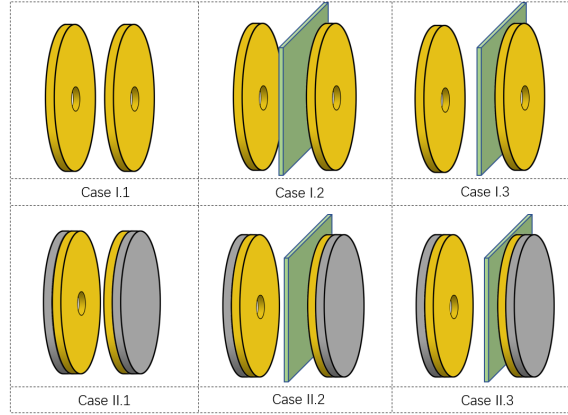


Fig. 2.12 Cases of measurement for Qi-A11 Coils with MLI

$$P_{eddy} = k_{eddy1} I_1^2 f^2 + k_{eddy2} I_2^2 f^2 \quad (2.61)$$

Where  $k_{eddy1}$  and  $k_{eddy2}$  are the complex multiple integrals representing the position and structure where eddy current exists [10]. Thus the value of  $k_{eddy1}$  and  $k_{eddy2}$  are constant under frequency variation.  $I_1$  and  $I_2$  are the coil RMS currents of the transmitter and receiver side generating the electric field inside the integral domain.  $f$  is the frequency of the magnetic field, which equals to the frequency of the alternating current. It is assumed that the external eddy current caused by the coil increases the equivalent resistance of each coil, so the eddy current loss is added to the coil copper loss to establish an equivalent resistance model. So the final resistance model for transmitter and receiver coils is:

$$\begin{aligned} R(f) &= \frac{P_{cond} + P_{prox} + P_{eddy}}{I^2} \\ &= k_{cond} + k_{pr} f^2 + k_{eddy} f^2 = k_{cond} + k_{total} f^2 \end{aligned} \quad (2.62)$$

## 2.7 Measurement Verification of the FE Models and Numerical Approaches

### 2.7.1 Verification for Regression Model

The employed coils are shown in Fig. 2.8 (a), the experiment platform is in Fig. 2.8 (b). The distance between two coils is 10 mm, and three cases for two types of coils have been measured as shown in Fig. 2.9. The first case is without MLI materials. In the second case, MLI materials is placed in the middle of two coils. In the third case,

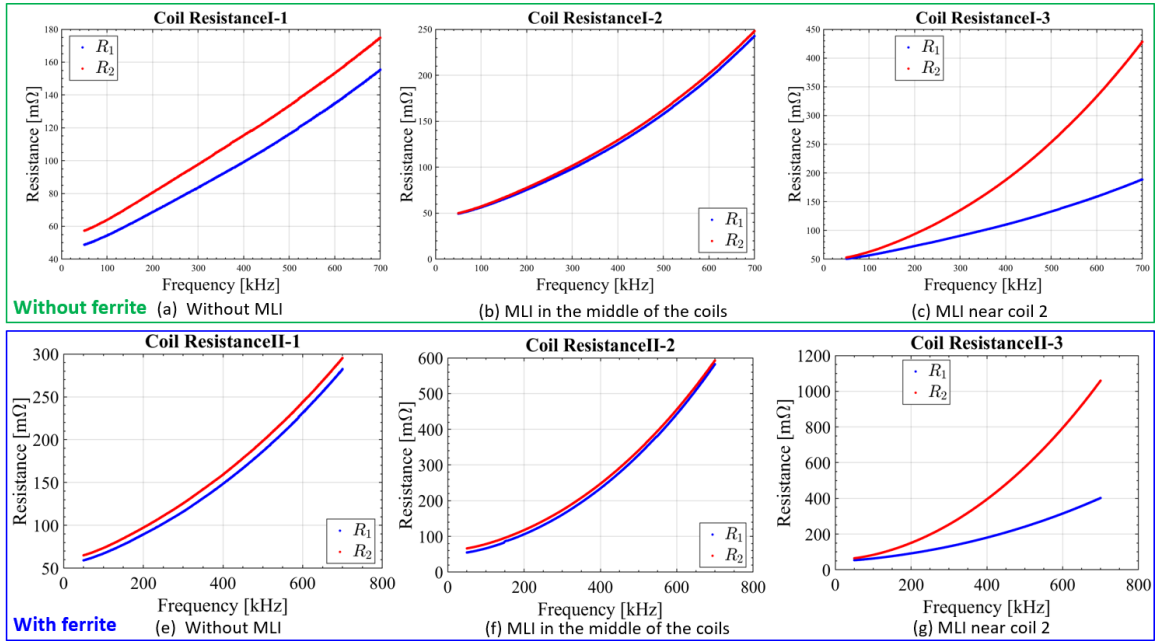


Fig. 2.13 Results of measurement for Qi-A11 Coils with MLI

MLI materials is placed near (about 1 mm) the secondary coil. The difference of two types of coils is whether the ferrite exists. The coils are TDK 10K2- A11-6-T170909 based on A11 specification of Qi [36], using AWG17 type 2 litz wire consists of 105 AWG40 strands. Measurement is carried out using KEYSIGHT E4990A Impedance Analyzer and the Agilent Technologies E5061B Network Analyzer, with both devices resulting in similar data. Frequency range is chosen to be 50-700kHz, because higher frequency leads to increasing hardware costs, while below 50kHz the quality factor is usually insufficient. The resistance of the coils with or without ferrite is shown in Fig. 2.10. It can be observed in Fig. 4 that the resistance increases with the frequency in all cases, and the MLI materials adds to the measured resistance of the coils in Fig. 2.10 (c) and Fig. 2.10 (g). The closer the MLI materials is, the higher the coil resistance increases. This is because the eddy current loss in MLI materials depends on the magnetic field, and the magnetic field strength is stronger near the coils. Comparing with the coils without ferrite, the coils with ferrite possess a higher resistance because of a higher magnetic strength. This is because the H-field influences the skin and proximity effects of the coil, and the eddy current in the MLI materials. Another property taken into consideration is the mutual inductance. Compared with the resistance, the frequency-dependent variation of mutual inductance is not significant. But the influence of MLI materials is obvious, due to the block of magnetic field, and MLI reduces the mutual inductance. In the rough calculation of optimal frequency,

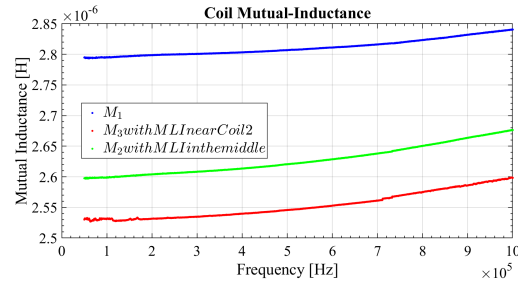


Fig. 2.14 Results of Mutual inductance for Qi-A11 Coils case I

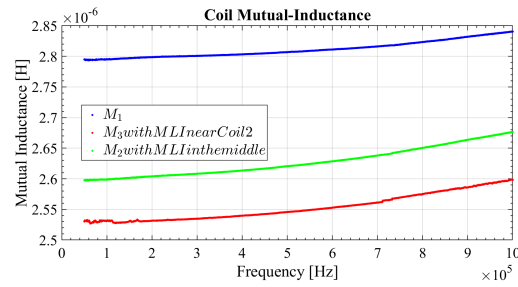


Fig. 2.15 Results of Mutual inductance for Qi-A11 Coils case II

mutual inductance can be considered as a constant, the result of mutual inductance variations are presented in Fig. 2.11 and Fig. 2.12.

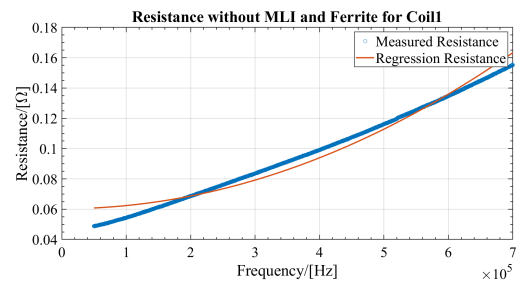


Fig. 2.16 Results of resistance for Coil 1 case I(a)

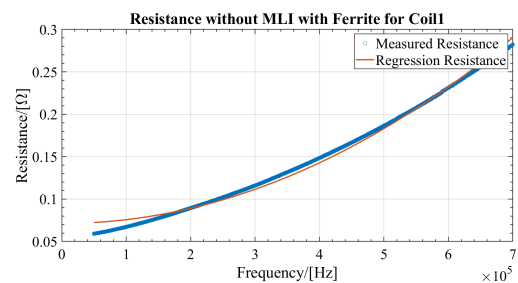


Fig. 2.17 Results of resistance for Coil 1 case II(a)

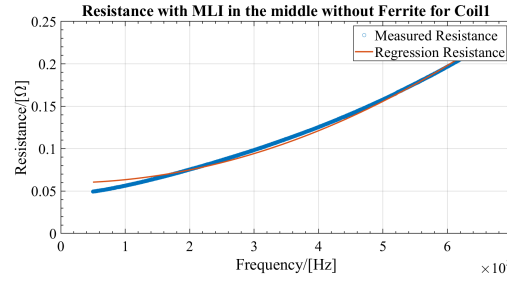


Fig. 2.18 Results of resistance for Coil 1 case I(b)

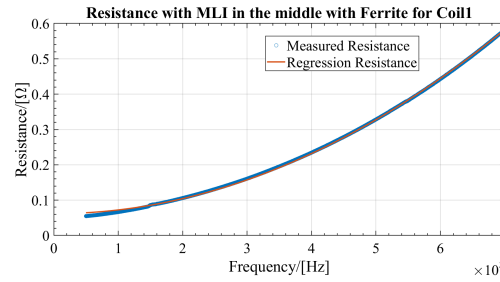


Fig. 2.19 Results of resistance for Coil 1 case II (b)

Based on the regression model, the OLS regression has been conducted. The objective is to verify the analysis and to estimate the factors and to calculate the optimized frequency for the coils. The regression result is shown in tables and curves below. The regression result based on proposed regression model is shown in Fig 2.13-23. The estimated  $k_{cond}$  as well as the  $k_{total}$  is shown in Table 2.1 and Table 2.2.

Both  $k_{cond}$  and  $k_{total}$  have a high confidence level of T-statistics ( $> 99.99$  percent), and  $R^2$  of the regressions is always higher than 96 percent. From the estimation parameters, it can be concluded that  $k_{cond}$  is similar to each other, representing the fixed conducting resistance, and the difference is because of the different length of connecting wires during the measurement and measurement errors. For  $k_{total}$ , it can be observed that the MLI materials' influence on resistance has the same order of magnitude as the proximity effect. This may be because of both losses are proportional to H-field squared. It can be observed for the regression model, to a large extent, the variation of resistance is explained. The higher the resistance is, the better the data fits the model. These measured parameters, together with the regression model, will be applied to the optimization in Chapter 4 and 5.

Table 2.1 Estimated results of  $k_{cond}$ 

| cases     | 1       | 2       | 3       |
|-----------|---------|---------|---------|
| Coil 1 I  | 0.06028 | 0.05958 | 0.06154 |
| Coil 2 I  | 0.07150 | 0.06143 | 0.06257 |
| Coil 1 II | 0.07125 | 0.06168 | 0.06308 |
| Coil 2 II | 0.07889 | 0.07398 | 0.06825 |

Table 2.2 Estimated results of  $k_{total}$ 

| cases     | 1         | 2         | 3         |
|-----------|-----------|-----------|-----------|
| Coil 1 I  | 2.103e-13 | 3.848e-13 | 2.737e-13 |
| Coil 2 I  | 2.315e-13 | 3.939e-13 | 7.559e-13 |
| Coil 1 II | 4.474e-13 | 1.063e-12 | 7.034e-13 |
| Coil 2 II | 4.618e-13 | 1.063e-12 | 2.023e-12 |

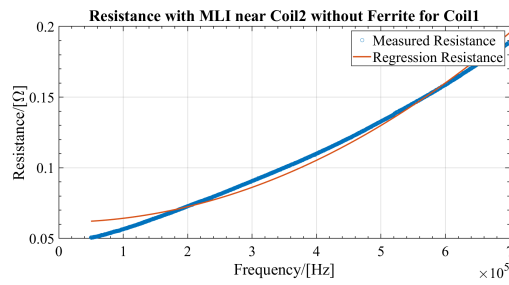


Fig. 2.20 Results of resistance for Coil 1 case I(c)

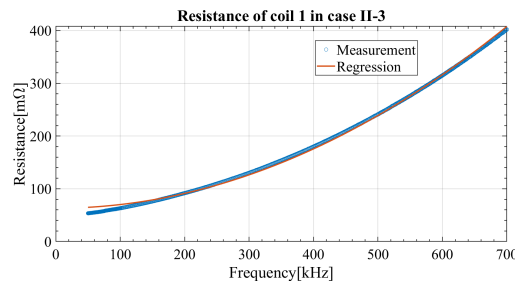


Fig. 2.21 Results of resistance for Coil 1 case II(c)

### 2.7.2 Verification for FE Model and AC-resistance Calculation

Comparison between the FE model results and the measurement results is also conducted, as well as the half-numerical half-FE method.

Note the FEMM it self do not provide the calculation result of self and mutual-inductance, block integral of the vector potential  $A$  is needed.

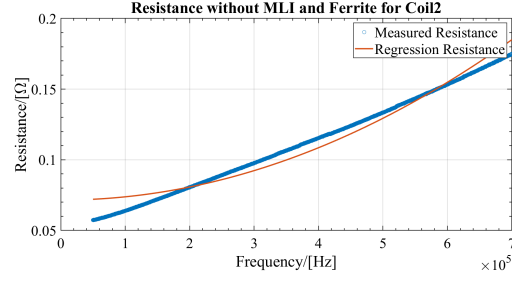


Fig. 2.22 Results of resistance for Coil 2 case I(a)

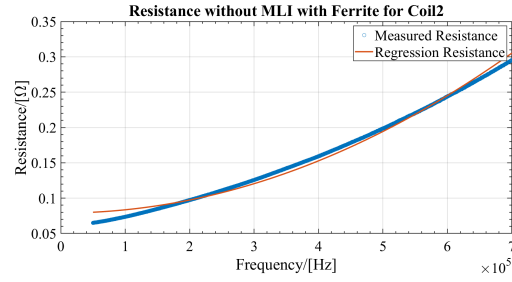


Fig. 2.23 Results of resistance for Coil 2 case II(a)

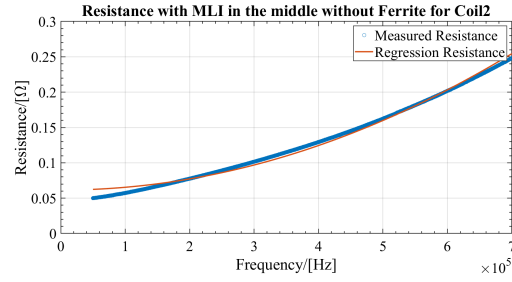


Fig. 2.24 Results of resistance for Coil 2 case I(b)

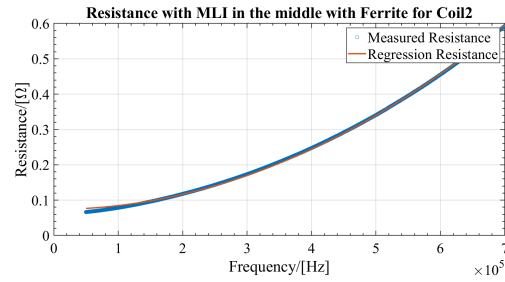


Fig. 2.25 Results of resistance for Coil 2 case II(b)

$$L_{\text{self}} = \frac{\int A \cdot J dV}{i^2} \quad (2.63)$$



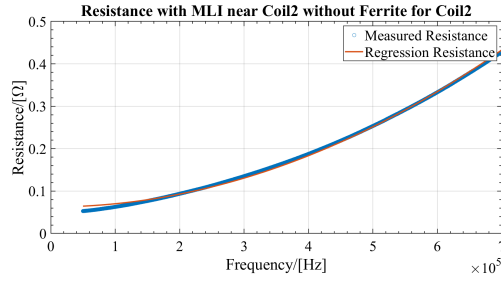


Fig. 2.26 Results of resistance for Coil 2 case I(c)

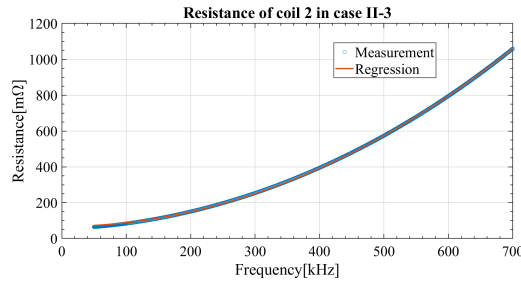


Fig. 2.27 Results of resistance for Coil 2 case II(c)

Where  $J$  is the current density, and  $i$  is the current flowing in the calculated coil.  $dV$  is the volume micro-element of the calculated coil. For the mutual inductance, it is calculated when there is current in transmitter coil, and no current in receiver coil.

$$L_{\text{matual}} = \frac{n_2}{i_1 a_2} \left( \int_{J_{2+}} A_1 dV_2 - \int_{J_{2-}} A_1 dV_2 \right) \quad (2.64)$$

Where  $J_{2+}$  is the current density out of the asymmetric plane and  $J_{2-}$  is the current density into the asymmetric plane, and  $i_1$  is the current flowing in the transmitter coil, and  $a_2$  is the cross section of the receiver coil.  $dV_2$  is the volume micro-element of the receiver coil.  $A_1$  is the vector potential caused by the current in the transmitter coil. The results are shown in Fig. 2. 25, for the 0.9mm diameter solid copper wire coil. Where JAXA means the experimental coil presented by JAXA, with 13 cm diameter, 1.55 mm fixed pitch, 21 turn and 10 cm air-gap in measurement.

The FE models are accurate in the calculation of the solid wire AC resistance, but as mentioned above, the calculation result of litz wire coil is not satisfyingly accurate. Hence the half-FE half-numerical method is adapted. To verify the model, measurement data of the Qi coils has also been compared to the calculated data, shown in Fig 2.26.

The results shows the calculation methods presented in this section, for basic parameters, is almost accurate in the estimation of the actual coils, for both solid

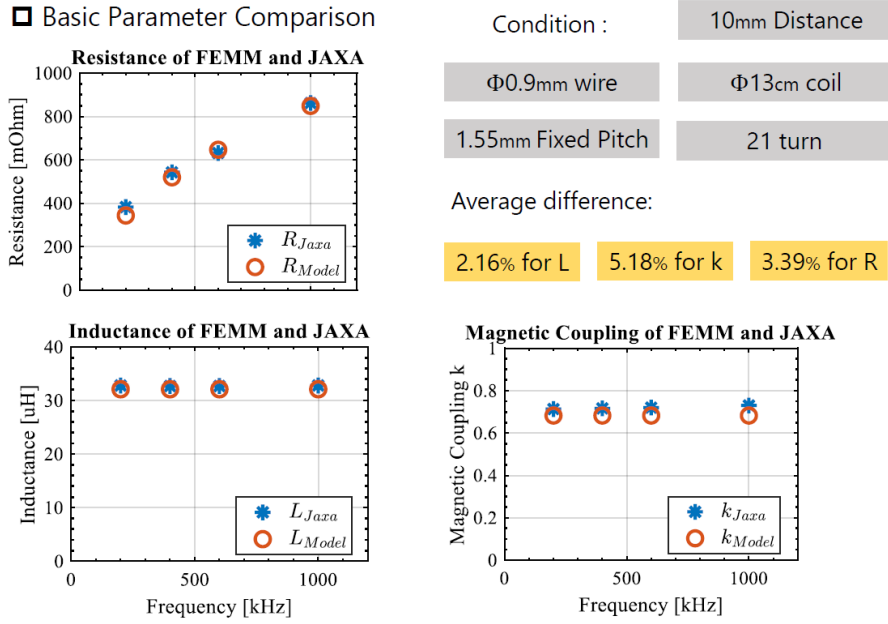


Fig. 2.28 Comparison between the basic parameters FE model and Measurement for a Solid Wire coil example

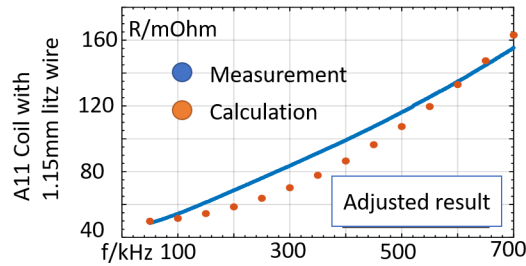


Fig. 2.29 Comparison between the AC resistance of half-FE model and Measurement for a Qi A11 coil example

and litz-wire coils. Based on these parameters, the power electronics losses can be estimated.

### 2.7.3 Verification for DC-DC loss estimation

An experiment for efficiency measurement of each part of a manufactured prototype is introduced to verify the estimation of the total loss. The hardware of the manufactured prototype will be introduced in next chapter, but here we present a comparison between calculation and the measurement.

The basic parameters in the calculation in this subsection is based on the LCR meter measurement data, to eliminate the influence of FE model errors.

Table 2.3 Circuit properties for calculation I

| Properties  | M/uH  | L/uH   | C/nF  | R/Ohm |
|-------------|-------|--------|-------|-------|
| Transmitter | 21.25 | 49.229 | 71.20 | 0.515 |
| Receiver    | 21.25 | 49.488 | 70.84 | 0.515 |

Table 2.4 Circuit properties for calculation II

| Properties | Vi/V   | Rdc/Ohm | f/kHz | $f_o$ /kHz |
|------------|--------|---------|-------|------------|
| Value      | 30.042 | 10.59   | 120   | 85         |

Firstly the circuit properties are listed in table 2.3 to 2.6.

Where the parameters are the mutual inductance, the self-inductance, compensation capacitance and coil resistance plus capacitor ESR in table 2.3.

Where the parameters are the DC source voltage, the load resistance, operation frequency and resonant frequency in table 2.4.

Where the parameters are the conduction resistance of the MOSFETs, the rise time of the MOSFETs, the fall time of the MOSFETs, and buck converter inductor inductance, DC-DC swithing frequency and the reverse recovery time and peak current for the converter in table 2.5.

Where the parameters are the reverse recovery charge of the buck diode, the gate charge of the MOSFETs, the DC resistance of the converter inductor, and dead time rise and fall periods in table 2.6.

The comparison result is shown in Fig. 2.27 and table 2.5.

One can observe from table 2.5, that the proposal of applying s-domain admittance to evaluate the circuit property is valid in the circumstance when the operation frequency is not the resonant frequency. The parameters, except the phase angles, which is assumed to be zero for the passive rectifier, possess a accuracy over 90 percent.

The calculated efficiency for the inverter, WPT, rectifer, buck converter and the total efficiency are : 96.1 percent, 90.3 percent, 94.7 percent, 94.4 percent and 77.6

Table 2.5 Circuit properties for calculation III

| Properties | Rds/mOhm | tr/ms | tf/ms | Lbuck/ mH | fsw/kHz | trr/ns | Irr/A |
|------------|----------|-------|-------|-----------|---------|--------|-------|
| Value      | 80       | 36    | 22    | 1.37      | 35      | 31     | 2.3   |

Table 2.6 Circuit properties for calculation IV

| Properties | Qrr/nC | Qg/nC | Vgs/V | DCR/Ohm | tDr/ns | tDf/ns |
|------------|--------|-------|-------|---------|--------|--------|
| Value      | 44     | 106   | 12    | 170     | 35     | 76     |

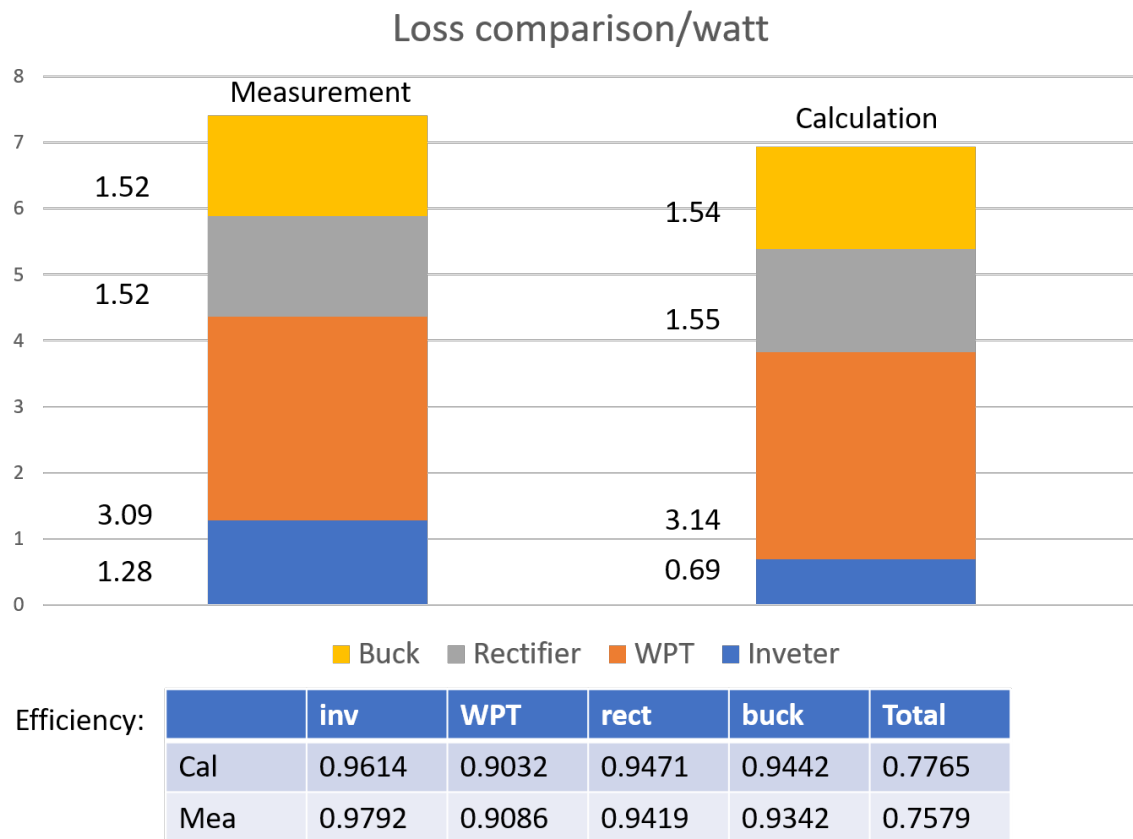


Fig. 2.30 Comparison between the DC-DC efficiency calculation and measurement

percent, while the measured efficiencies are 97.9 percent, 90.8 percent, 94.2 percent, 93.4 percent and 75.8 percent, respectively.

One can conclude that as for the calculation method of DC-DC efficiency, there's no large error. In consequence, the application of the calculation method towards the coil optimization is meaningful.

## 2.8 Summary

In this chapter, most of the numerical equations for loss estimation used in this thesis has been presented. Most of the equations are based on conventional literature.

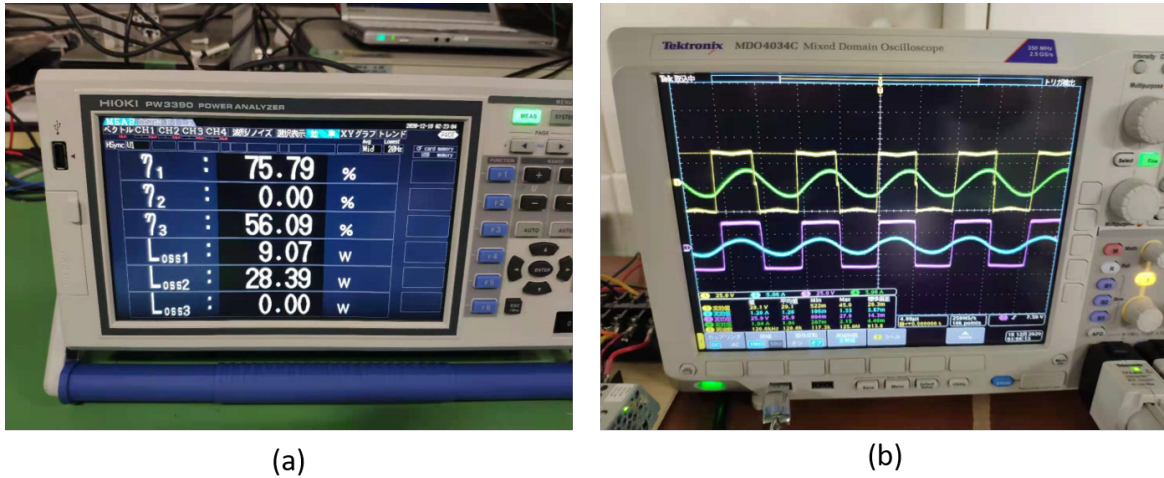


Fig. 2.31 Experiment for the DC-DC efficiency measurement

Table 2.7 Comparison result of WPT circuit

| Properties | V1/V    | V2/V   | I1/A   | I2/A   | $\phi_1$ | $\phi_2$ |
|------------|---------|--------|--------|--------|----------|----------|
| Cal        | 27.0514 | 2.0163 | 2.0163 | 1.2638 | 58       | 0        |
| Mea        | 27.509  | 1.8715 | 1.8715 | 1.2255 | 52       | 17.23    |

To calculate the WPT efficiency at frequency splitting condition, the s-domain admittance and frequency response is applied. The method is traditional, but the application into the WPT efficiency is new in the author of this thesis' knowledge.

Moreover, to estimate the influence of the MLI materials towards the parameters in WPT, a simple regression model is presented based on the measurement.

The calculations has been verified by the experiments and measurements in this chapter.



## **Chapter 3**

# **Conventional and Proposed MPPT Strategies for Lunar Rover WPT system**

As mentioned in Chapter 1, the prerequisite of optimization, when involved with circuit calculation, is the determination of the circuit operation status. Hence, the operation strategies have to be determined first.

This chapter introduced traditional MPPT for Lunar Rover WPT system, and introduced newly proposed operating algorithm. Because frequency splitting is possible in Lunar Rover WPT MPPT process, and it haven't been considered before, this chapter adjusted the traditional MPPT algorithms for DC-DC efficiency improvement.

In addition, since the influence of the extreme temperature variations between Lunar day and night on lunar surface, the variation of compensation circuit also requires new strategies to solve the mismatch influence for the Lunar rover WPT system. A new proposal of frequency-duty two dimensional method for the PV MPPT therefore presented in this chapter.

### **3.1 Review of previous Lunar Rover MPPT Strategies**

Since the PV output is DC, the traditional methods for searching the MPP of PV output is generally carried out by DC-DC converters.

The tradition is also adapted in the design of the Lunar Rover topology, for which the only difference with traditional MPPT scheme could be the DC-DC converter for

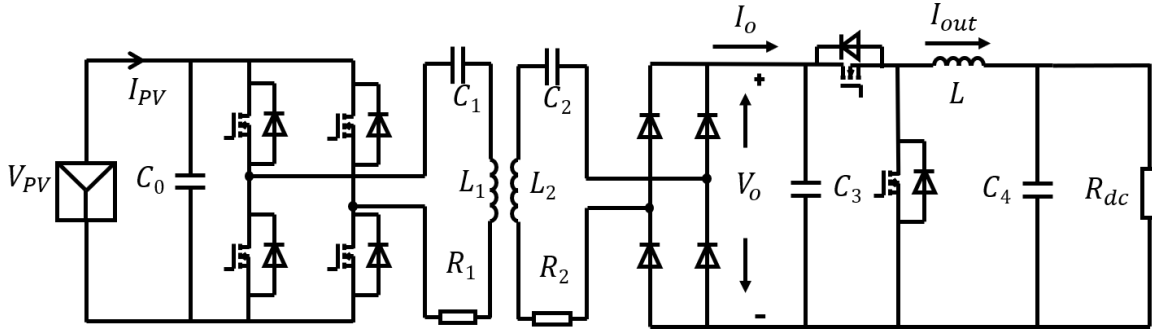


Fig. 3.1 Lunar Rover WPT topology

MPPT is placed at the secondary side of WPT. The topology of is shown in Fig. 3.1, with the simplification of the load into resistor, comparing to the actual prototype in chapter 2.

Before this thesis, there are already several strategies have been presented for the Lunar rover PV MPPT.

These algorithms include duty-sweep method, In-con method, the particle swarm optimization method.

### 3.1.1 Duty-Sweep Method

The purpose of MPPT is to find the maimum power point on the PV output curve. Therefore, sweep the duty of the secondary converter could sweep the input resistance for the PV, by comparison of output power points through the sweep, MPPT is achieved.

$$R_{in} = \frac{\pi^2}{8} \left( R_1 + \frac{\omega^2 M^2}{R_2 + 8R_{dc}/\pi^2 d_{pv}^2} \right) \quad (3.1)$$

Where  $R_{in}$  is the input resistance of the PV. When solar radiation intensity varies, the sweep curve needs to be refreshed to track the new maximum point.

### 3.1.2 Perturb and observe algorithm

The Perturb and observe algorithm is also called Hill-climbing method, in this algorithm, the controller will slightly increase or decrease the voltage and measure its power. If the power increases, continue to adjust the voltage in the same direction until the power does not increase [23].



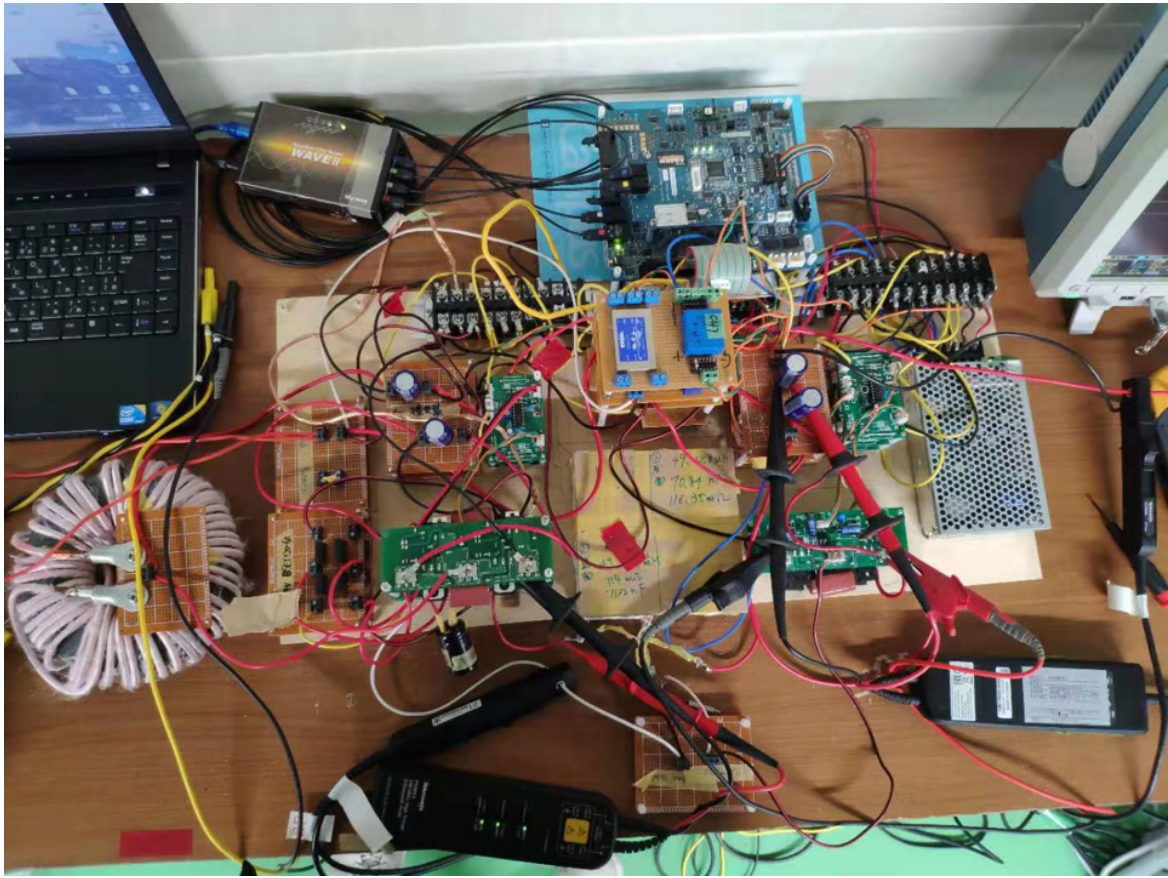


Fig. 3.2 Experimental Platform

The principle of this method is that for solar cells, the power changes with voltage and there is only a maximum value.

For multi-modal curves, this method may not find the maximum power point.

### 3.1.3 Variant Step Incremental Conductance Method

The incremental conductance method controller will gradually adjust the voltage and current of the solar module to predict the effect of changing the voltage [24].

In the previous Lunar Rover WPT research, a method based on the characteristics of uneven conductance increment was proposed.

This modification makes variable step change every time the MPPT is implemented

### 3.1.4 Particle Swarm Optimization Method

Particle Swarm Optimization (PSO) is a common metaheuristic algorithm. Because this thesis will also use this method later, we will only briefly introduce it in this subsection [22, 46, 47].

The principle of PSO is to simulate the process of optimization with the movement of a group of particles in space. Each particle will record its position (duty cycle) and power in each iteration and move to the particle with the highest power to find the global optimum.

### 3.1.5 Drawbacks of the previous methods

The operation strategies above are adjusting the converter duty cycle to track the MPP [6].

The operation frequency remains stable, thus the possibility of frequency splitting has been ignored in traditional scheme.

If frequency splitting has not occurred, when the system can resonate perfectly, this approach is certainly feasible. However, the harsh environment on the moon [48] may cause the resonant capacitor to work at different extreme temperatures, and because the primary side is connected to the PV, it is more exposed to the extreme temperature of the lunar surface. It is very difficult to perfectly compensate the impedance.

Moreover, because the main work of this thesis is coil optimization, and in coil optimization, frequency and air-gap adjustments may cause frequency splitting. Under frequency splitting phenomenon, the higher frequency isolated is generally used as the operating frequency in WPT researches, in order to avoid a lagging phased voltage and harmonics.

## 3.2 Experimental Platform Manufacturing

In order to verify the algorithm in this chapter and the subsequent optimization results, the experimental platform is manufactured.

The topology of the experimental platform is in Fig. 3.1. The hardware of the system is shown in Fig. 3.2.

TI 28335 DSP is applied to the platform, and the sensors are applied to measure the PV side and load side voltage and current.

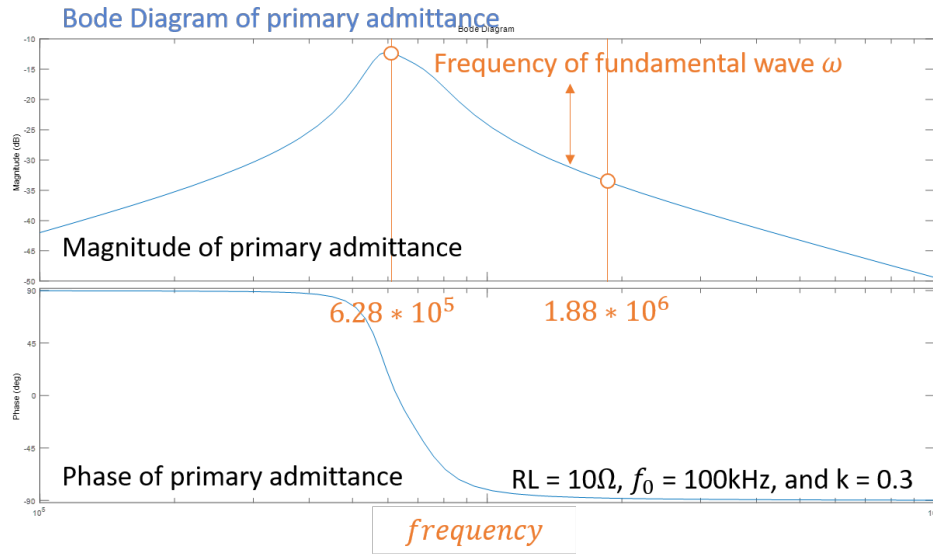


Fig. 3.3 Admittance example without frequency splitting

### 3.3 Proposed Duty-sweep MPPT with frequency adjustment

As mentioned above, for ordinary MPPT systems, DC-DC converters are generally used to implement algorithms.

Nowadays, there are few researches on the combination of PV and WPT, and, like lunar rover WPT system, MPPT with WPT system which needs to simplify the primary side as much as possible is even rarer.

As a result, to the best knowledge of the author of this thesis, there is no paper combining frequency splitting with MPPT, which is the most important phenomenon in WPT design.

In this section, the thesis proposes a sweep method to realize MPPT. The specific method is to realize the change of PV input resistance through the duty sweep of the secondary side DC-DC converter, at the same time of duty sweeping, because the  $R_L$  in the WPT circuit also changes, when the change reaches the critical value, frequency splitting will occur. Through calculation, we can determine the two separated resonance frequencies obtained by frequency splitting, and take them as the instruction value of inverter frequency.

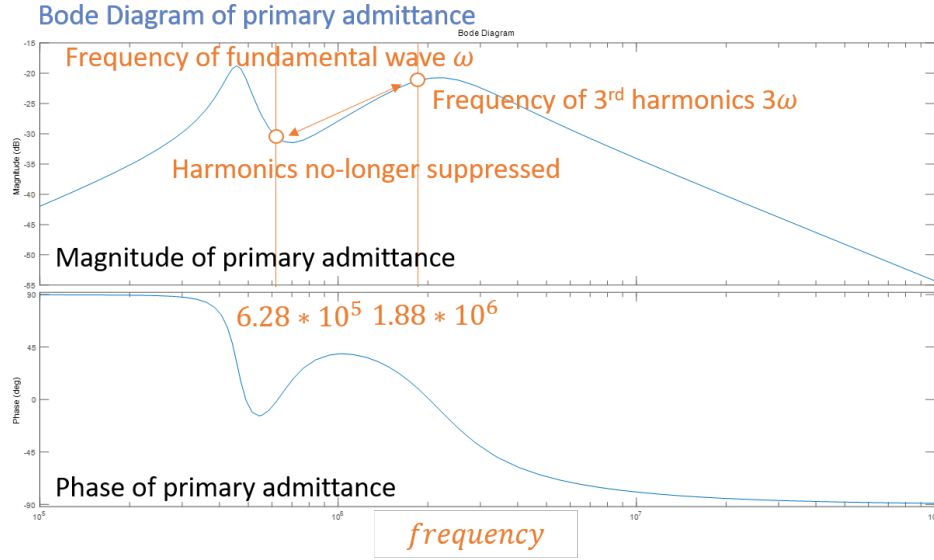


Fig. 3.4 Admittance example with frequency splitting

### 3.3.1 Motivation and application

Although there are not many WPT systems related to PV, frequency splitting has been widely studied in WPT systems powered by power grid or DC power supply.

For a frequency splitting system, the general practice is to set the operating frequency at a higher resonance frequency. On the one hand, this method can reduce the current harmonics of the system, on the other hand, it can ensure that the current lags behind the voltage or the current is in phase with the voltage in the primary circuit. (For voltage driven resonant inverter, turn on loss can be eliminated and reverse recovery of diode can be avoided).

In the past research of WPT, there have been many uses of impedance or admittance Bode diagram to depict the influence of frequency splitting on the higher harmonic of current. Here, the admittance diagram Fig. 3.2 is also used as an example to illustrate the reason of operating at higher frequency.

In addition, for DC power supply, in the case of frequency splitting, compared with the original resonance point, the transmission power of the new resonance point is relatively large due to its smaller impedance, as expressed in equation 3.2. For PV system, this change is related to MPPT.

$$P_{\omega_{1,2}} = \frac{U_1^2 (R + R_L)^2 + U_1^2 X^2}{U_1^2 (R + R_L)^2 + R X^2 P_{\omega_0}} P_{\omega_0} \quad (3.2)$$

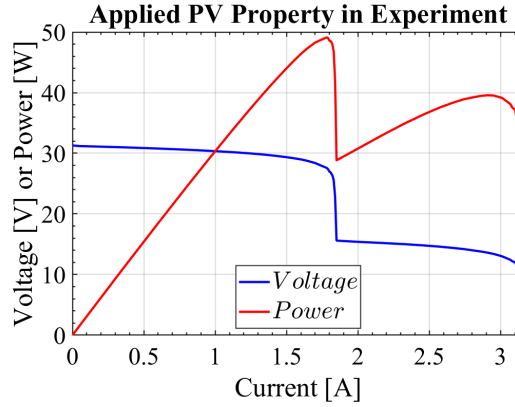


Fig. 3.5 PV output property applied in the experiments

For WPT design, if only KQ product is considered, the smaller the air-gap, the better the result. Although this is consistent with experience, it is not reasonable to ignore frequency splitting in the case of small air-gap in comparison.

Therefore, for the calculation of DC-DC efficiency, when frequency splitting occurs, we use the higher resonance frequency as operation frequency, corresponds with most of the researches.

Therefore, in order to keep the running state and calculation consistent, and also because of the above advantages of working at higher resonance frequency, we carry out MPPT and frequency splitting detection, and always make the system work around higher resonance frequency.

### 3.3.2 Proposed Algorithm

The principle is the same with duty sweep method mentioned in section 3.1.1. When conducting sweeping, the detection of the following criterion is carried out simultaneously.

- Step 1: Duty sweep, for every iteration, repeat step 1 and duty + duty step
  - Step 1.1  $R_L$  estimation

$$R_L = \frac{8R_{dc}}{\pi^2 D^2} \quad (3.3)$$

- Step 1.2 Frequency splitting detection. If

$$4M^2 + C^2 (R + R_L)^4 - 4LC (R + R_L)^2 > 0 \quad (3.4)$$

– and

$$2L - C(R + R_L)^2 - \sqrt{4M^2 + C^2(R + R_L)^4 - 4LC(R + R_L)^2} > 0 \quad (3.5)$$

– Do

$$\omega_2 = \sqrt{\frac{2L - C(R + R_L)^2 + \sqrt{4M^2 + C^2(R + R_L)^4 - 4LC(R + R_L)^2}}{2C(L^2 - M^2)}} \quad (3.6)$$

– else

$$\omega_2 = \omega \quad (3.7)$$

– Operation frequency determination

$$f_2 = \frac{\omega_2}{2\pi} \quad (3.8)$$

– Step 1.3 Update Maximum power point.

– Step 1.4 Repeat step 1.

• Step 3: When duty sweep stopping criteria is satisfied

– Stop the iteration (sweep).

– Find out the MPP result

– Set as Operation point

Where the  $R$ ,  $L$ ,  $C$  and  $M$  are the measured data of the symmetric resonant loop, and the  $R_L$  is the load resistance and  $R_{dc}$  is measured by the current and voltage sensor of the load, and  $D$  is the duty cycle.

After the algorithm starts, sweep the Duty cycle from 0.1 to 0.9, with a sweep step of 0.01. Record the load power after each change. If the power is larger than the previous one, record it as the maximum power point, and record the duty and frequency at this point. At the very beginning, because the load is lighter, frequency splitting does not occur, and then as the load changes, a maximum value will be obtained first. When frequency splitting occurs, the new power value will naturally be compared with the previous maximum, so that we can fairly evaluate different air-gap designs.

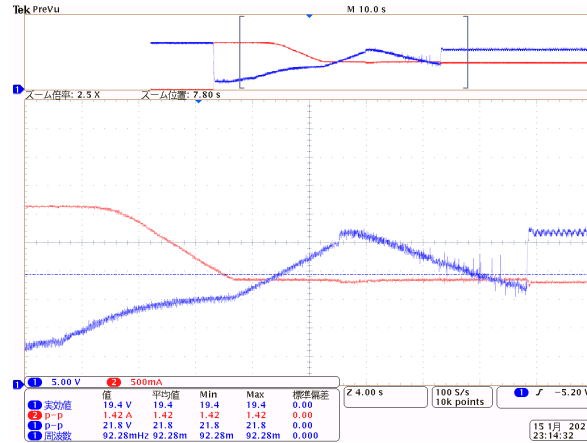


Fig. 3.6 Experiment result of the Proposed Duty-sweep method with frequency adjustment

### 3.3.3 Experimental Verification

A two peak partial-shading PV output curve is simulated by the PV simulator, shown in Fig. 3.5, as the power source of the experiment platform. The load applied is the high power variable resistor.

The resonance frequency is set to 85kHz, and the operating frequency is determined by the load. The remaining parameters are the same as those in the verification experiment in Chapter 2.

PV output variation during scanning is shown in Figure 3.6. Where channel 1 is the output voltage of the PV simulator, and the channel 2 is the output current. It cannot be observed by this figure directly of the inverter frequency, however, from the variation PV input resistance, one can observe the turning point. The beginning frequency of the system is 85 kHz, the MPP frequency of the experiment is 91.825 kHz, and MPP duty cycle is 0.88, with a DC-load efficiency of 85.18 percent.

The MPP of the PV simulator output is set as 27.61 Volt and 1.77 Ampere, with a maximum power of 48.98 Watt, the tracked MPP is 27.08 Volt and 1.79 Ampere, with power of 48.59 Watt. The MPPT efficiency of the proposed method is 99.2 percent.

The experiment result shows the presented method's feasibility of MPPT. And the algorithms successfully adjusted the operation frequency.

## 3.4 Proposed Duty-frequency 2-dimensional MPPT

As mentioned in the introduction, the extreme temperature on the lunar surface influences the parameters of the resonant loops, especially the compensation capacitor.

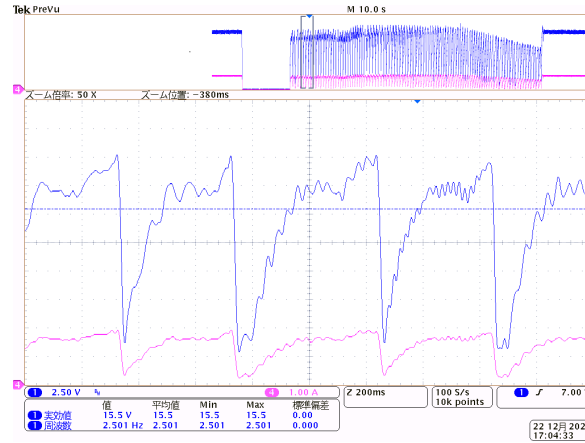


Fig. 3.7 Experiment result of two-dimensional Duty-frequency sweep method

Therefore, in this section, we propose a MPPT algorithm which does not rely on accurate calculation, and can also adjust the frequency at the same time to ensure the current lag voltage of the inverter, so as to obtain higher DC-DC efficiency.

First, we use two-dimensional scanning to prove the feasibility of this method. Then, in order to reduce the time complexity of the algorithm, we use two-dimensional PSO method to track the maximum efficiency.

### 3.4.1 Duty-frequency two dimensional sweeping

This method is an extension of the previous scanning method. If we scan not only the duty cycle, but also the working frequency of the inverter, we will get the result as shown in Figure 3.7.

In Fig. 3.7, channel 1 is the load voltage, and channel 4 is the load current. For every small loop of the sweep, the duty varies from the 0.1 to 0.9 with a 0.01 step. The large sweep loop changes the operation frequency, from the resonant frequency 85 kHz to 120 kHz, with a step of 500 Hz.

From Fig. 3.7 one can conclude, the optimum frequency of the system could be other than the resonant frequency. One of the reasons is the frequency sweep can enlarge the reflected impedance range towards the primary side, so as to compensate the part that cannot be sweep by the DC-DC converter, another reason is the DC-load efficiency is frequency dependence, and higher efficiency may be achieved by another operation frequency other than the resonant frequency. However, the 2-dimensional sweep method's time complexity is intolerable, thus the PSO is applied in next subsection.



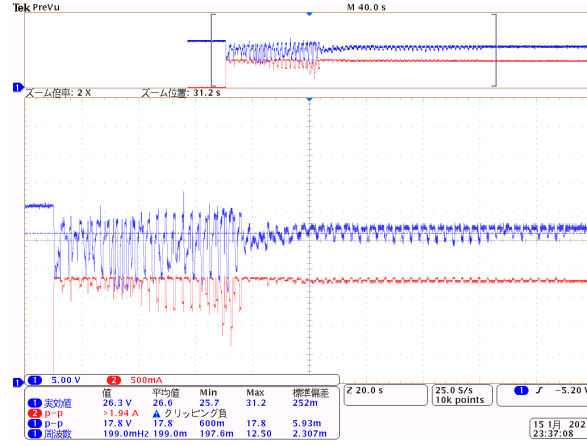


Fig. 3.8 Experiment result of two-dimensional Duty-frequency PSO method

### 3.4.2 Duty-frequency two dimensional PSO

#### Traditional PSO

PSO is a global optimal algorithm to simulate animal population. PSO is known for its fast convergence, and its steps are as follows. Firstly, generating particles in design space. Secondly, evaluating performance of each design. Thirdly, particles moving to the global best position and its personal best position. At last, particles convergence to the optimum point. The mathematical modelling of PSO is as follows.

$$\vec{x}_t = \vec{x}_{t-1} + \vec{v}_t \quad (3.9)$$

$$\vec{v}_t = \vec{v}_{t-1} + c_1 r_1 (\vec{p}_{t-1} - \vec{x}_{t-1}) + c_2 r_2 (\vec{g}_{t-1} - \vec{x}_{t-1}) \quad (3.10)$$

Among which,  $\vec{x}_t$  is the position of a particle in the  $t$ -th iteration,  $\vec{v}_t$  is its speed in the  $t$ -th iteration,  $\vec{p}_{t-1}$  is the historical optimal position of the particle,  $\vec{g}_{t-1}$  is the global optimal position of all particles up to the  $t-1$  th iteration,  $r_1$  and  $r_2$  are random numbers between 0 and 1 to increase the algorithm's randomness, while  $c_1$  and  $c_2$  respectively represent the impact of local optimal and global optimal on particle speed update.

#### Modified PSO with a random velocity

In the MPPT problem, in order to reduce the complexity of the algorithm, particles population is often small. In this thesis, the population is set to be 4, the same as previous researches. However, 4 particles are enough for 1-dimensional searching,

but too few for the 2-dimensional searching. To improve the exploration of the algorithm, a random velocity is applied in the algorithm.

$$\vec{x}_t = \vec{x}_{t-1} + \vec{v}_t \quad (3.11)$$

$$\vec{v}_t = w\vec{v}_{t-1} + c_1r_1(\vec{p}_{t-1} - \vec{x}_t) + c_2r_2(\vec{g}_{t-1} - \vec{x}_t) + c_3r_3\vec{v}_m \quad (3.12)$$

The three learning factors,  $c_1$ ,  $c_2$  and  $c_3$  are distributed as, when the iteration is less than a preset figure, only  $c_3$  possess non-zero value. Then  $c_1$  and  $c_2$  are switched on and  $c_3$  will be switched off to conduct a general PSO. Finally, only the  $c_2$  will be non-zero, for compulsory convergence of the algorithm.

For the 2-dimensional PSO in this section, the position  $\vec{v}_t$  represents the vector of duty and frequency.

$$\vec{x}_t = [duty, frequency] \quad (3.13)$$

And the velocity represents the vector of variation of the duty and frequency. Generated by equation 3.9.

$$\vec{v}_t = [\Delta duty, \Delta frequency] \quad (3.14)$$

The program loops are realized by the interruption functions in DSP.

### 3.4.3 Experiment Verification

The experiment result of proposed 2-dimension PSO MPPT is presented in Fig. 3.8.

Channel 1 is the voltage of the PV simulator, while channel 2 is the current. At the beginning of the algorithm, as there is only random velocity for the particles, the variation is random and large-scaled. In the middle of the algorithm, the algorithm became conventional PSO, and periodic variation and convergence of the voltage and current can be observed. Through the convergence of the PSO, the PV output finally being stabilized at the end of the algorithm.

One can observed from the experiment result that the convergence of the 2-dimension PSO is achieved within tens of iterations. With initial frequency of 85kHz, 95kHz, 110kHz and 120kHz, the particles convergence to the operation frequency at 107.69kHz, with duty of 0.72. The MPPT efficiency is 99.57 percent and the DC-load efficiency is 84.43 percent.

## 3.5 Summary

In this section, the MPPT strategies for the Lunar Rover WPT system have been introduced. Two major proposals, one to calculate and adjust the operation frequency to eliminate the influence of WPT frequency splitting, another to directly conduct frequency-duty 2-dimensional MPPT have been presented in this chapter.

The proposed methods has been verified by the experiments, the successful convergence of the PV output to the MPP shows the feasibility of the proposed operation strategies. Comparison of the experiment results shows the proposed methods are benefit for the improvement of MPPT efficiency for the systems combining MPPT and WPT.

To the best of the author's knowledge, the proposed methods are the first attempt of combining the frequency-splitting phenomenon of WPT with MPPT for a secondary positioned DC-DC MPPT converter topology. The proposed methods could be applied to other system which shares similar topology with Lunar Rover WPT system.

The proposed method of the frequency adjustment in section 3.3 will be applied in the DC-DC efficiency calculation for the coil-frequency optimization in Chapter 5.



## Chapter 4

# Single-Objective Optimization for Lunar Rover WPT

After determination of the operation conditions of the Lunar Rover WPT system, we are going to optimize several design parameters of the system.

At the beginning of the research, JAXA first commissioned the author of this thesis to find out the most suitable operating frequency for the Lunar Rover WPT system.

In this chapter, firstly based on the measurement data, frequency splitting for a certain mini-model will be introduced.

Then considering the optimum frequency is highly system-depended, optimization based on FE models through the meta-heuristic algorithms will be presented, optimizing the coils together with the operation frequency.

The algorithms applied in this section is the Exhaustive algorithm, PSO, Genetic algorithm (GA), and a newly proposed modified PSO namely Logistic-PSO (LPSO).

The cost functions applied in this sections for FE optimization is conventional efficiency evaluation method based on  $KQ$  product and the conventional circuit calculations, as well as the inverter efficiency, as mentioned in Chapter 2.

### 4.1 Optimization based on Measurement

This section presents the optimization results based on the calculation of the proposed regression models, which has been introduced in Chapter 2. The optimization in this section is based on VNA measurement and conventional circuit calculation, and will only be valid for the Qi A11 coil.

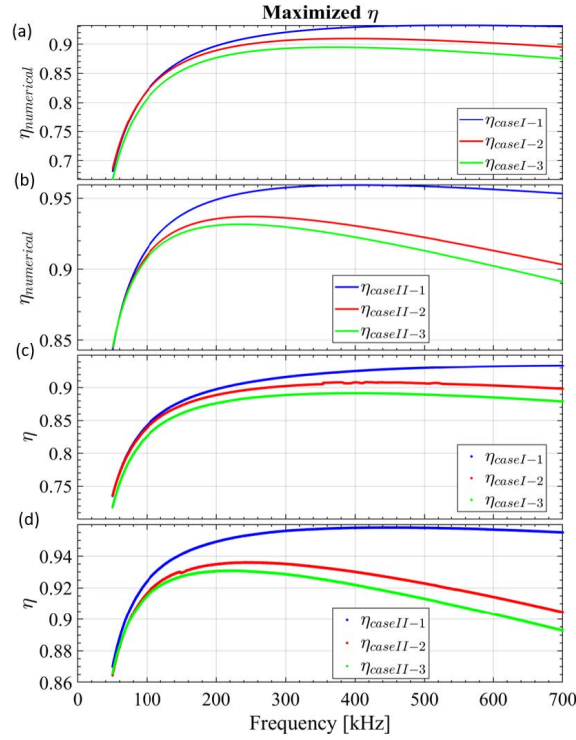


Fig. 4.1 Frequency optimization based on VNA measurement and regression models

However, the calculations based on measurement shows how the MLI material influence the optimum operation frequency. Which can be referenced in the future considerations of design. The frequency sweeping for the mini-model (shown in Fig 2.8 and cases shown in Fig 2.9) is from 50 kHz to 700 kHz, and the calculations applied are based on equation 2.58 for AC resistance, equation 2.14 for load-matching and equation 2.15 for efficiency evaluation.

Based the regression models in chapter 2, the numerical solutions for optimal frequency are calculated. The  $M$  at 50 kHz is chosen to calculate the relation of maximum efficiency and resonance frequency. The calculation result is shown in Fig. 4.1(a),(b). The optimized frequency calculated by the regression models is: 545.4kHz for case I-1; 394.2kHz for case I-2; 369.4kHz for for case I-3. For the systems with ferrite, in the three cases, the optimized frequencies are 406.1kHz, 252.0kHz and 234.5kHz, respectively. MLI and the ferrite reduces the optimal resonance frequency. Ferrite can improve the maximum efficiency at lower frequencies, but when there are MLI materials, the efficiency drops more rapidly with respect to the frequency in a higher frequency range.

Compared with efficiency at 85kHz, the efficiency at optimal frequency increases largely, for case I at 85kHz, the WPT efficiency is 82.25 percent, 82.03 percent and

80.63 percent respectively. But the efficiency at the optimal frequencies is 93.39 percent 90.84 percent and 89.17 percent. For case II, at 85kHz, the efficiency is 91.47 percent, 90.78 percent, 90.67 percent, respectively. The corresponding maximum efficiency at optimal frequencies is 95.81 percent, 93.62 percent and 93.1 percent, respectively.

The case when MLI nears one coil possesses the lowest maximum efficiency and optimal frequency, although in this case the transmitter coil has a lower resistance than the case of MLI material in the middle of two coils. This may be because the symmetric structure has a higher efficiency, and the increase of the resistance of the secondary coil ( $R_2$ ) is larger than the decrease of  $R_1$ . The efficiency curves based on calculating the measured data directly by the conventional WPT efficiency equation have been shown in Fig. 4.1 (c)(d). It can be observed that the regression model agrees with the measurement. For arbitrary WPT systems with MLI, the regression model can be applied to establish a numerical model of frequency-dependent maximum efficiency with few data. The limitation of this work is that the regression model is not a closed-form solution for frequency optimization, which needs measurement data to establish a numerical formula when applying to other coils.

Because the measurement data is not always available, further researches are needed to establish a specific model. Based on the conclusion of this section, by developing the functions of the factors in the proposed regression model, further studies can propose more specific formulas to explain the maximum efficiency at different frequencies.

## 4.2 Optimization Based on Meta-heuristic algorithms

In this section, a design scheme of uncertain working frequency is proposed, which considers the efficiency of WPT part and the loss of inverter part. By constantly changing the coil design parameters and frequency, we can find the best operating frequency of the wireless charging system of lunar rover. In order to reduce computation, the open-source 2-D finite element analysis tool FEMM is adopted. The symmetrical circular coil WPT system is studied. The calculation method of the AC resistance is from section 2.5. The calculation method of inverter loss is introduced in chapter 2.4.1, with MOSFET data from data sheet.

The optimization method is shown in Fig. 4.2. At first, optimization based on exhaustive algorithm is carried out, to show the existence of maximum point inside the design space.

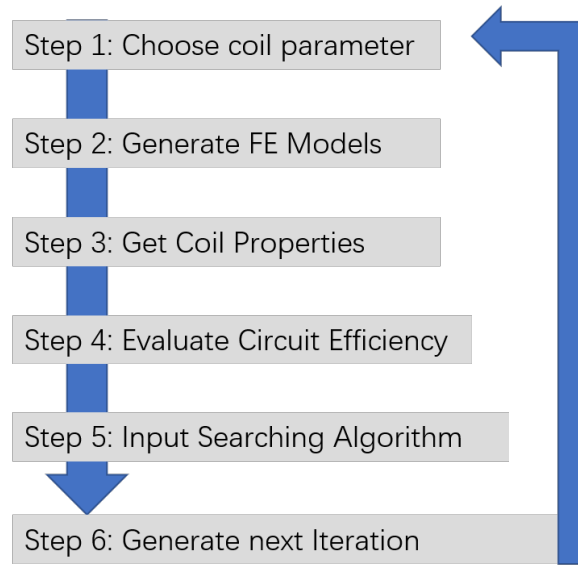


Fig. 4.2 Optimization methods of meta-heuristic algorithms

Table 4.1 Fixed Design Parameters

| Parameters      | Value | Unit |
|-----------------|-------|------|
| Air-gap         | 20    | mm   |
| Outer Radius    | 13    | cm   |
| Strand Diameter | 0.08  | mm   |
| Strand number   | 105   | NA   |
| Wire Diameter   | 1.15  | mm   |
| Input Voltage   | 20    | Volt |

Through the interaction on with MATLAB, each data point of searching algorithm comes from a finite element simulation.

Meta-heuristic algorithm is used to accelerate the optimization process. In this section, two meta heuristic algorithms, genetic algorithm (GA) and particle swarm optimization algorithm (PSO), are applied to the coil design optimization process. Compared with exhaustive method, meta-heuristic algorithm greatly speeds up the design process and makes the optimization more accurate.

The parameters optimized for is shown in table 4.1. And the fixed coil parameters are shown in table 4.2, respectively.



Table 4.2 Variant Design Parameters

| Parameters   | Unit | Upper limit | Lower limit |
|--------------|------|-------------|-------------|
| Turns        | NA   | 0           | 56 (full)   |
| Frequency    | kHz  | 0           | 900         |
| Inner Radius | mm   | 0           | 40          |

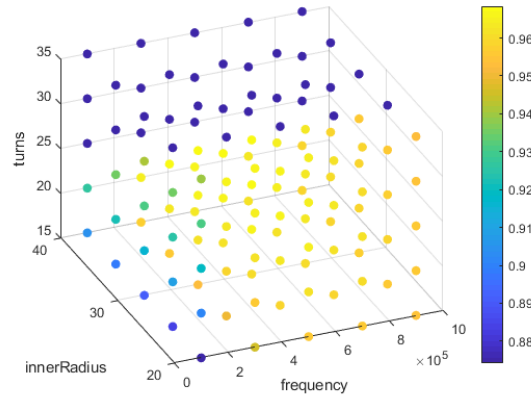


Fig. 4.3 Optimization result of Exhaustive algorithm

### 4.2.1 Exhaustive Algorithm

In the most traditional design method, when we need to design a parameter, the general method is to control other variables, only change one parameter to be designed, and then make multiple designs examples and compare the examples with each other.

If we change the variable evenly, and exhaust all design possibilities to find the best design, this method is called exhaustive algorithm.

In Fig. 4.3 the result of exhaustive algorithms is shown. Every point in the Fig 4.3 shows a result of efficiency calculation, and colorbar shows the magnitude of calculated WPT and inverter efficiency. The physical constraints also considered in the calculation, with zero efficiency for every impossible design.

From the result one can infer that there's optimum point inside design space, however, because the limitation of calculation points of exhaustive algorithm, it is impossible to obtain accurate result in continuous design space. To optimize WPT system in the continuous design space, PSO and GA have been implemented.

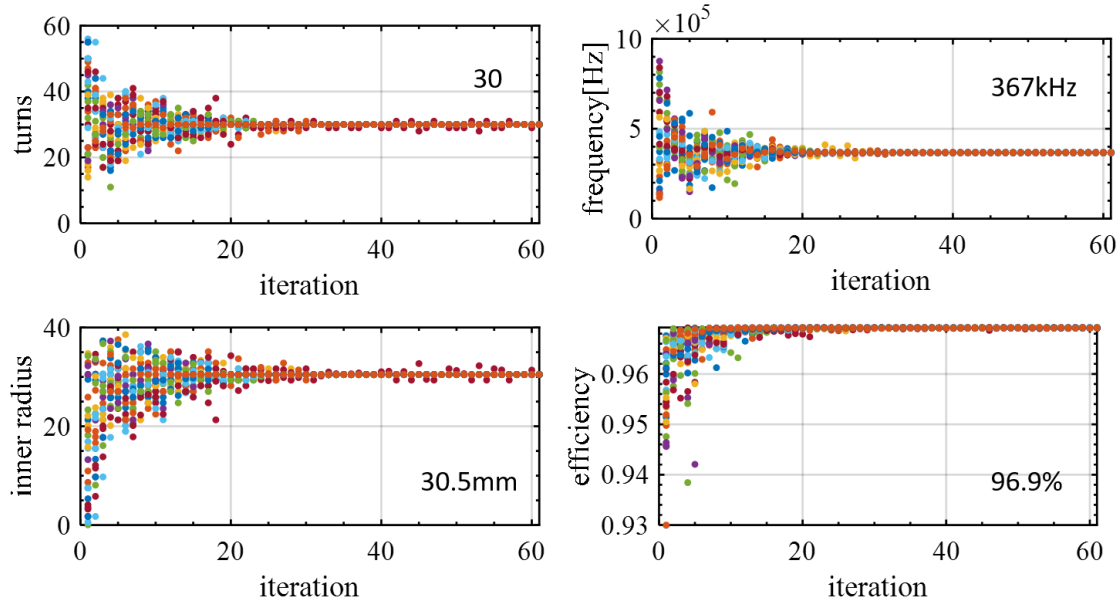


Fig. 4.4 Optimization result of pso for WPT efficiency

#### 4.2.2 PSO optimization for KQ product

The introduction of PSO has been carried out in Chapter 3. Here, PSO is used to search for the optimum inside the design space.

The positions of PSO for the  $t$  – th iteration in this section is:

$$\vec{x}_t = [\text{innerradius}, \text{frequency}, \text{turns}] \quad (4.1)$$

While the velocity update obeys equation 3.7. The convergence of the PSO algorithms is shown in Fig. 4.4-5.

#### 4.2.3 Genetic algorithm and GA optimization for KQ product

Compared with PSO, genetic algorithm has more sufficient mathematical basis. In this section, genetic algorithm is used to verify the results of PSO.

Genetic Algorithms has been applied in the following processes. At first, a number of position vectors,  $[\text{innerradius}, \text{frequency}, \text{turns}]$  is randomly generated inside the design space. Then cross over is conducted, at first the random vector  $\alpha$  is generated, then the off-springs are generated by the random vector and the parents.

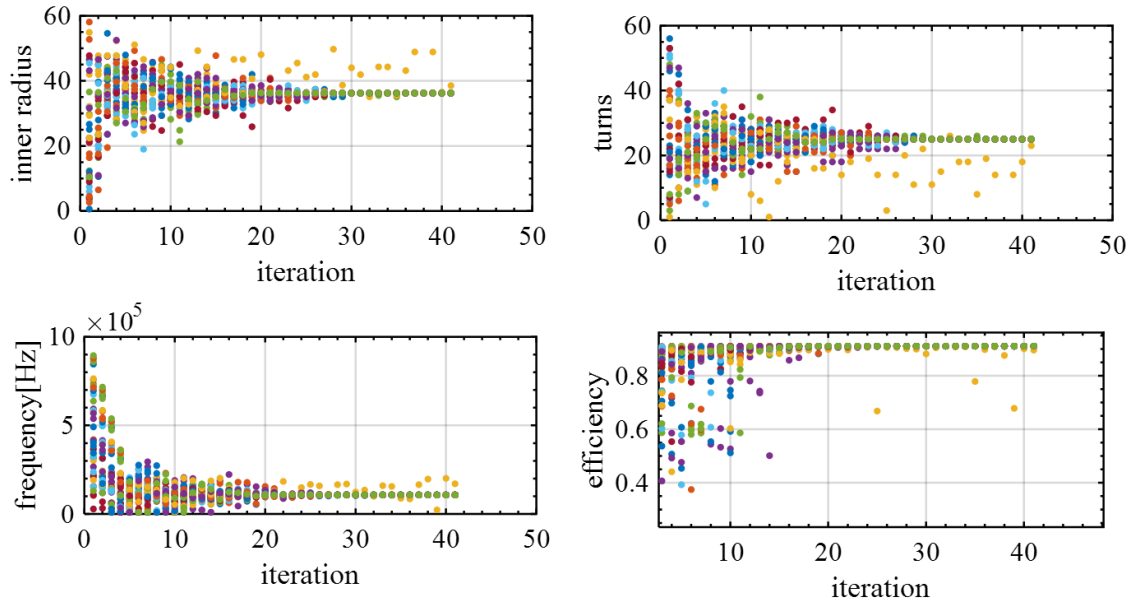


Fig. 4.5 Optimization result of pso for WPT and inverter efficiency

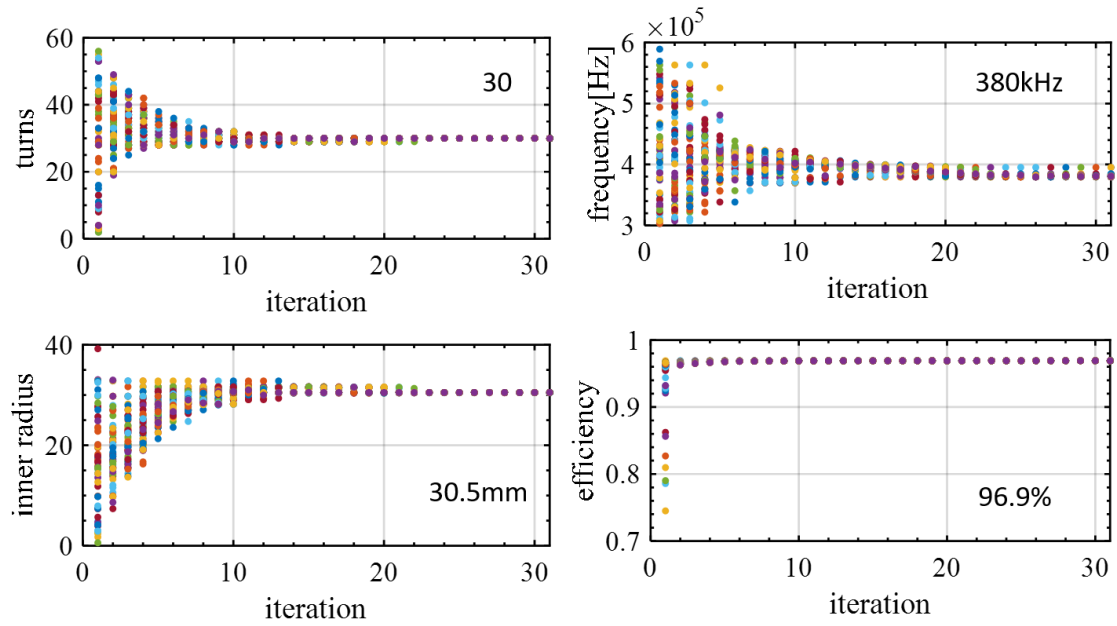


Fig. 4.6 Optimization result of GA for WPT efficiency

$$\begin{aligned}
 x_1 &= (x_{11}, x_{12}, x_{13}) = (f_1, R_{in1}, N_1) \\
 x_2 &= (x_{21}, x_{22}, x_{23}) = (f_2, R_{in2}, N_2) \\
 \alpha &= (\alpha_1, \alpha_2, \alpha_3) \\
 \alpha_i &\in [0, 1]
 \end{aligned} \tag{4.2}$$

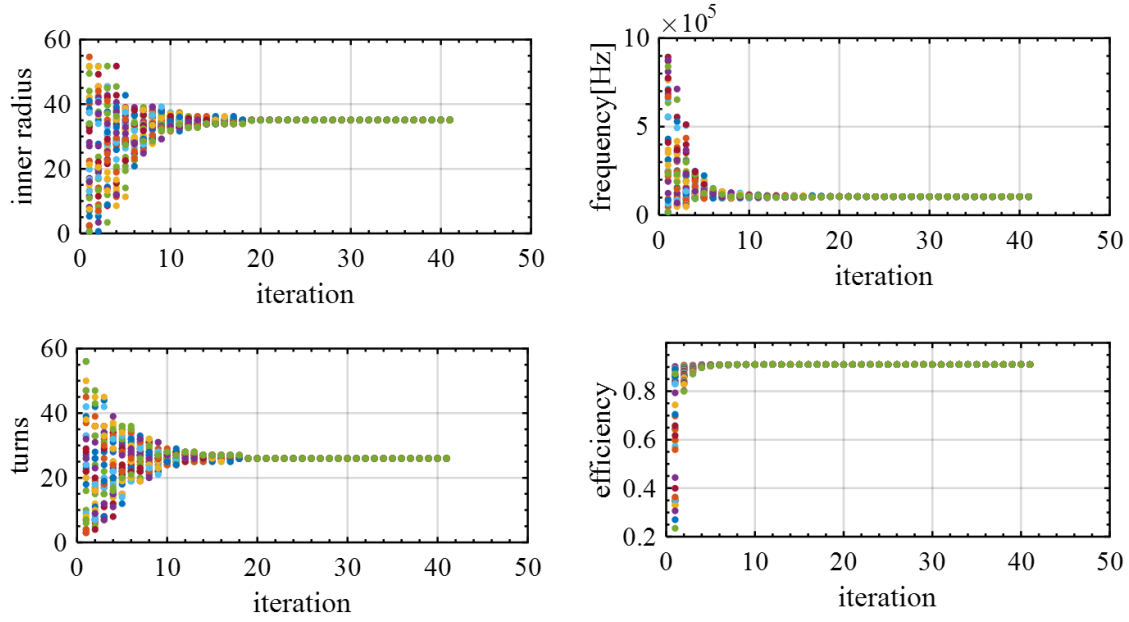


Fig. 4.7 Optimization result of GA for WPT and inverter efficiency

Where,  $\alpha$  is the random vector, and the  $x$  is the parents vectors. Then the offspring  $y$  is generated, as:

$$\begin{aligned}
 y_{1i} &= \alpha_i x_{1i} + (1 - \alpha_i) x_{2i} \\
 y_{2i} &= \alpha_i x_{2i} + (1 - \alpha_i) x_{1i} \\
 y_1 &= (y_{11}, y_{12}, y_{13}) \\
 y_2 &= (y_{21}, y_{22}, y_{23})
 \end{aligned} \tag{4.3}$$

The mutation is conducted after crossover section, for a random position, it can be expressed as:

$$\begin{aligned}
 x &\rightarrow x' \\
 x_j &\rightarrow x'_j \\
 x_j &= x_j + \delta
 \end{aligned} \tag{4.4}$$

Where  $x'$  is the generated new vector, and the  $\delta$  is a random number generated based on Gaussian distribution. After crossover and the mutation, the parents and offspring are merged together, and evaluated. The efficient solutions are selected to be the parents of next iteration.

#### 4.2.4 Discussion of Optimization results and Algorithm Selection

In order to consider the influence of inverter loss on the optimal operating frequency and coil design, two different objective functions are optimized in this section. Firstly, the KQ product of symmetrical coil is optimized. KQ product determines the highest efficiency of WPT part. Then the multiplier efficiency and WPT efficiency are optimized as the new objective function. At first, the exhaustive searching is applied to ensure there is a global best solution inside the design space. Then PSO is conducted, and GA is conducted to verify the result of PSO.

Each color represents a particle, and 60 iterations are carried out in total. The efficiency of 30 particles is calculated in each iteration. From these results, we can see that the PSO converges very fast and converges to the only point. At 30 iterations, PSO has almost converged. Finally, for the optimized result of 13cm coil, the optimal frequency is about 367khz, which is obtained at 30.5mm inner diameter and 30 turns.

It is worth mentioning that the distance between the wires of the coil can be calculated by the number of turns and the inner diameter, that is, pitch. In this section, according to the PSO optimization results, when pitch is zero, the coil KQ value is the maximum. Next, the same optimization process is repeated with GA, and the result is basically the same as that of PSO. The optimization results of GA are shown in Fig. 4.6 and Fig. 4.7. It can be observed that the convergence of GA is more uniform than that of PSO, and the convergence speed is slower. However, in this section, the number of GA population is set to 60, which is twice the number of PSO, so in order to ensure the same calculation, the number of iterations is changed to 30. From the comparison between the results of GA and PSO, we can see that in addition to the optimization results of the optimal frequency, the difference between the two is about 3.4 percent, and the differences of other optimization results are all below 1 percent. Therefore, the author considers that the results of GA and PSO are mutually verified, and the optimal results of WPT with 30 turns, 30.5 mm inner diameter and about 370 khz frequency of 13 cm coil are obtained.

After the KQ product of the coil is optimized, the consideration of the inverter loss is also added to the optimization process. The result is very different from the original optimization result, mainly because the influence of the inverter loss on the optimal resonance frequency is very obvious.

The calculation of inverter loss must be carried out under the fixed voltage and current. Therefore, in this optimization, the DC voltage is specified as 20V, and the load is set as the highest WPT efficiency all the time, and the current is calculated from this. However, it is worth noting that the phase of the current is set to 5 degrees

lagging voltage. After considering the loss of class D inverter, the optimal frequency converges to 105 kHz, while the optimal number of turns of the coil decreases to 26. Figures 4.5 to 4.7 show the optimization results. In the same way, PSO and GA optimization are implemented under the same condition considering the inverter loss, the optimization results are almost the same, the difference is less than 1 percent.

To sum up, this section draws a conclusion that, before and after considering the inverter loss, not only the optimal frequency of the system has changed, but also the structure of the optimal coil has changed. This change is often ignored in previous FE analysis.

To sum up, one can conclude from the PSO and GA optimization that, the application of meta-heuristic algorithm can reduce the calculation of coil optimization design and reduce the trial and error cost of coil design. Secondly, after considering the loss of the inverter, the optimal frequency and the number of turns of the coil will change. Therefore, in coil design, in addition to WPT efficiency itself, other frequency dependent losses are also very important, and they also affect the coil structure.

### 4.3 Proposed Logistic PSO

In this section, a new algorithm, based on the scheme of PSO, combining the exploration ability of exhaustive algorithm and the convergence speed of PSO is proposed for further FE optimization. The algorithm is inspired by the diffusion phenomenon, but different with traditional diffused PSO, with random velocity controlled by the learning coefficients. The learning coefficients are distributed by Logistic-distribution, so the algorithm is named Logistic PSO (LPSO). The multi-objective version of LPSO algorithm will be implied in the optimization in Chapter 5.

#### 4.3.1 Motivation of Modified Algorithm

When we use PSO to track the optimal operating point as in Chapter 3, we often hope that the algorithm can converge quickly. Moreover, in the process of tracking, there is often not much space to explore. These properties determines that the original PSO starts convergence at the first iteration. In general numerical calculations, although the space for exploration may be large, the calculation cost of every particle in every iteration may not be too high, so we can afford large amount of populations. However, when we apply the PSO into FEM design, for every particle at every

iteration, we have to calculate the H-field at every point of the mesh. Which means the calculation cost is so high that we can no longer afford a large population of particles. If we let the particles converge at the first iteration of the algorithm in a large design space, there is risk of convergence towards a local best than the global best. In the optimization based on PSO and GA, we can already find out that for the optimization at the same condition, the result can be different. Which means the convergence of the particles may not be the global best.

Here we propose a modified PSO based on the diffusion phenomenon, to increase the exploratory ability of the algorithm to reduce the possibility of the algorithm converging to local best.

### 4.3.2 Principles of Modified Algorithm

In traditional PSO, the learning coefficients  $c_1$  and  $c_2$  are constant, which is recommended to be 1.496[30]. It means the algorithm starts to converge at the first iteration, this is favorable in applications with low-dimension searching space and large amount of particles. However, in application of design, the design space is usually high-dimensional, and calculation amount of evaluation is large. As a result, the possibility of convergence to local best is increased in design application.

To reduce the possibility of convergence combine the PSO and exhaustive algorithms is proposed. We know that when the particles are moving, if the velocity of the particles are random, the particles will spontaneously diffuse toward the places with low concentration, as expressed in equation 4.5.

$$\frac{\partial \varphi}{\partial t} = D \nabla^2 \varphi \quad (4.5)$$

Therefore, we divide the original algorithm into three processes: diffusion, searching and convergence. The implementation method is as follows.

A random velocity is added to the original velocity update of PSO, and the learning coefficients are distributed by combinations of Logistic functions.

$$\vec{x}_t = \vec{x}_{t-1} + \vec{v}_t \quad (4.6)$$

$$\vec{v}_t = w\vec{v}_{t-1} + c_1 r_1 (\vec{p}_{t-1} - \vec{x}_t) + c_2 r_2 (\vec{g}_{t-1} - \vec{x}_t) + c_3 r_3 \vec{v}_m \quad (4.7)$$

Where learning coefficients are:

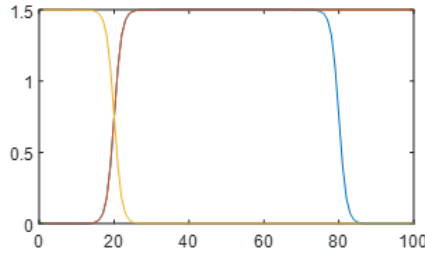


Fig. 4.8 Distribution of three learning coefficients( blue:  $c_1$ , red:  $c_2$  and  $c_3$ , yellow:  $c_3$ )

$$c_1 = \frac{L}{1 + e^{-k(t-t_0)}} \times \left(1 - \frac{L}{1 + e^{-k(t-t_1)}}\right) \quad (4.8)$$

$$c_2 = \frac{L}{1 + e^{-k(t-t_0)}} \quad (4.9)$$

$$c_3 = 1 - \frac{L}{1 + e^{-k(t-t_0)}} \quad (4.10)$$

Where  $L$  determines the upper limit of coefficients, which is set to be 1.5 in this section,  $k$  determines the variation speed between each step of algorithm, set to be 1 in this section  $t_0$  and  $t_1$  is the determine line of each step. The distribution of learning coefficients divide the algorithm into three steps continuously.

At the beginning of the algorithm,  $c_3$  is the dominant coefficient, therefore the particles diffuse in the searching space. Then  $c_1$  and  $c_2$  become dominant and the algorithm become conventional PSO. After a certian period,  $c_1$  decrease and the particles are forced to convergence.

### 4.3.3 Test of New Algorithm

In order to briefly test whether our algorithm can really increase the possibility of converging to the global optimal as imagined, we compared the convergence of several mainstream search algorithms on the test function.

The test function we use is the eggholder function shown in equation 4.11. It has many local optima and only one global optimum, which is shown in equation 4.12.

$$f(\mathbf{x}) = -(x_2 + 47) \sin \left( \sqrt{\left| x_2 + \frac{x_1}{2} + 47 \right|} \right) - x_1 \sin \left( \sqrt{|x_1 - (x_2 + 47)|} \right) \quad (4.11)$$



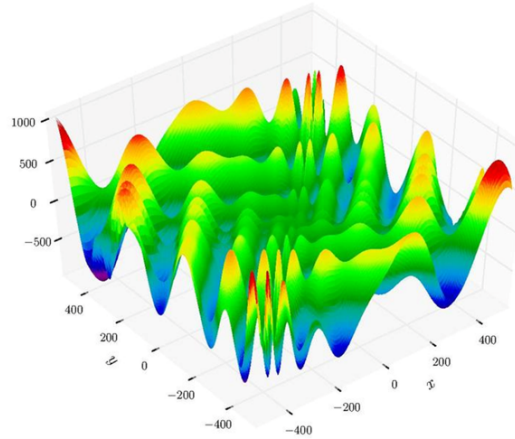


Fig. 4.9 The test function eggholder

$$f(\mathbf{x}^*) = -959.6407, \text{ at } \mathbf{x}^* = (512, 404.2319) \quad (4.12)$$

The successful rate is applied in comparison of algorithms. We repeat the search for each algorithm on the test function one hundred times. When the true global optimum is found, the experiment is considered successful. Finally, the number of successful experiments divided by one hundred, as the success rate.

Table 4.3 Comparison of proposed and conventional algorithms

| Algorithm | Successful rate |
|-----------|-----------------|
| LPSO      | 0.98            |
| PSO       | 0.25            |
| GPSO      | 0.24            |
| GA        | 0.2             |

In order to simulate the amount of calculation in the actual FEM optimization, we set iterations to 100 and population to 30 for each algorithm.

It can be seen from the results that, compared to mainstream algorithms, our proposed LPSO has a greater possibility of finding the global optimum under low population numbers.

The author thinks this algorithm is more suitable for FEM optimization than traditional PSO and GA. Its multi-objective version will be applied for optimization in Chapter 5.

## 4.4 Summary

In this chapter, we performed a single-objective optimization of WPT. The optimization function is the  $kQ$  product of the WPT system, which represents the highest efficiency of the WPT system. First of all, we optimized the operating frequency with the measurement data. The results show that the use of MLI and ferrite will advance the optimal frequency. Secondly, in order to optimize the coil and working frequency at the same time, we applied FEM and search algorithm to optimize the number of turns, inner diameter and frequency of the coil at the same time. From the optimization result, we found pitches convergences to zero. The coil should not be wound to the center, the frequency and number of turns of the coil will vary depending on whether inverter loss is considered, but the result of pitch will not. Finally, inspired by the difference in the results of each optimization, we proposed an improved algorithm LPSO for FEM optimization.

## Chapter 5

# Multi-Objective optimization for Lunar Rover WPT

As for the previous researches of WPT optimization, most of them only focus on the efficiency, ignoring other important parameters.

However, if we consider only efficiency in the optimization of WPT frequency, the only result that can be obtained is that the higher the operating frequency, the higher the WPT efficiency in most of the cases. This is obviously inconsistent with the facts, because based on experience, we need to carefully select frequencies to ensure the balance of all parts of the WPT system.

So in this chapter, we try to introduce the concept of Pareto optimality in economics into our WPT frequency optimization research.

At the beginning of this chapter, multi-objective optimization based on measurement data will be performed. This optimization is carried out for the theoretical maximum efficiency and theoretical maximum power of the WPT system. However, because it takes time to make the actual model for the measurement, the only parameter for optimization is the operating frequency. Therefore, optimization results based on measured values are limited.

Next, we applied the MOEAD algorithm to multi-objective optimization of air-gap and efficiency.

Finally, based on the PV mathematical model and the DC-DC efficiency calculation formula in Chapter 2, combined with the working status determined by the MPPT method in Chapter 3, as well as the proposed LPSO in Chapter 4, we performed the Pareto optimization of power density and thermal density.

One of the optimization results was made as a real coil and a measurement experiment was carried out.

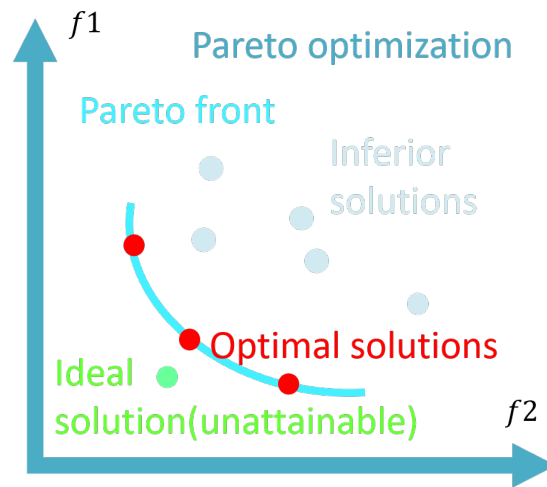


Fig. 5.1 Pareto Optimization illustration

## 5.1 Pareto Optimization

Pareto Optimality, proposed by Italian economist Vilfredo Pareto, also known as Pareto efficiency, refers to an ideal state of resource allocation, assuming an inherent group of people and allocatable resources, from one allocation state to another. In a state of change, at least one person becomes better without making anyone worse off. This is called Pareto improvement or Pareto optimization.

In the field of engineering, the Pareto Optimization is also called multi-objective optimization. The principle is to find out a set of solutions, namely Pareto Front. The solutions on the Pareto Front are Pareto-optimized, which means the further improvement of one objective for the solution means the degradation of another objective of design. The solutions on the Pareto Front is also called Feasible solutions. If for one design, there is any other solutions that possess better performance in every design objectives, we call the design is dominated by the later solution.

Most engineering problems are multi-objective optimization problems, there are many conflicting objectives in these problems. Different from single objective optimization problems, the essence of multi-objective optimization is that, in most cases, the improvement of one objective may cause the degradation of other objectives' performance, and it is impossible to achieve the optimization of multiple objectives at the same time, and only a coordinated trade-off and compromise can be made between the objectives. The optimal solution of the multi-objective optimization problem is composed of many Pareto optimal solutions.

### 5.1.1 Review of Pareto Optimization in the WPT Design

Some previous studies have combined WPT with multi-objective optimization. Reference [14] gives a comprehensive analysis of the maximum efficiency and power density of the electric vehicle WPT through exhaustive algorithm and multi-objective optimization. In reference [27], by optimizing the maximum efficiency and VA rating of WPT system at the same time, the multi-objective particle swarm optimization algorithm is used to find the optimal parameters of a specific WPT system. Similar optimization is also applied to the optimization design of ferrite and coil structure. The objective functions considered are magnetic coupling  $K$ , magnetic lead and quality factor  $Q$  [49]. Optimization for some novel cost functions such as channel capacity in communication circuit together with traditional indicator power transfer capability  $S_{21}$  [50] also have been discussed.

In addition, there are also examples of multi-objective optimization of capacitive coupled WPT and optimization research on the specially designed optimization functions [51], and in the field microwave wireless charging system, multi-objective optimization has also been considered recently [52].

In these researches, only [14] provides us with systematical considerations for WPT system, but the method suffers from calculation cost and ignorance of frequency splitting.

Compared to the methods introduced in 5.1.1, Chapter 5 provides a systematic point of view based on multi-objective heuristic algorithms, taking frequency-slitting and MPPT into consideration. The combination method of different aspects will be especially reflected by section 5.4.

## 5.2 Frequency Optimization based on Measurement

Based on the measurement result of mini-model in Chapter 2, we conducted the optimization for maximum efficiency and maximum power of a WPT system. The design parameter is frequency in this section.

### 5.2.1 Cost Functions

In this section, a multi-objective optimization considering both efficiency and power is presented based on the measurement data of coils. With applying pareto optimization to frequency selection, the influence of the eddy current between the

coils is discussed, and the recommended frequency range for higher efficiency and power for different position of MLI materials is presented.

$$\eta = \frac{\omega^2 M^2 R_L}{(R_2 + R_L)(R_1 R_2 + R_1 R_L + \omega^2 M^2)} \quad (5.1)$$

$$R_L = R_{\eta \max} = \sqrt{R_2 \left( \frac{\omega^2 M^2}{R_1} + R_2 \right)} \quad (5.2)$$

The maximum efficiency of the system is calculated by equation 5.1.

$$R_{P \max} = \frac{(\omega M)^2}{R_1} + R_2 \quad (5.3)$$

$$P_{\max} = \frac{1}{4R_1 \left( 1 + \frac{R_1 R_2}{(\omega M)^2} \right)} \dot{U}_1^2 = k_p \dot{U}_1^2 \quad (5.4)$$

The maximum power is calculated through the Maximum power transfer theorem, where the maximum power is at 50 percent WPT efficiency, calculated by equation 5.2.

the expression of the optimization problem can be expressed as equation 5.5.

$$\begin{aligned} \min \quad & l(f) = \max(w_1(\eta(f) - \eta^*), w_2(P(f) - P^*)) \\ \text{subject to} \quad & 50\text{kHz} \leq f \leq 700\text{kHz} \end{aligned} \quad (5.5)$$

### 5.2.2 Chebyshev Metric Method

This is a traditional decomposition approach for Pareto optimization. Because we cannot directly compare different vectors of objective functions (We can only compare the magnitude of each coordinate) we turn the comparison of vectors into the comparison of the distance to the ideal vector. The ideal vector is the ideal design.

In this approach, the distance is Chebyshev Metric. The Chebyshev Metric is the maximum absolute value among all the coordinates. The definition and calculation method is shown in equation 5.6 and 5.7.

$$D_{\text{Chebyshev}}(x, y) = \lim_{p \rightarrow \infty} \left( \sum_{i=1}^n |x_i - y_i|^p \right)^{1/p} \quad (5.6)$$

$$D_{\text{Chebyshev}}(x, y) = \max(|x_i - y_i|) \quad (5.7)$$

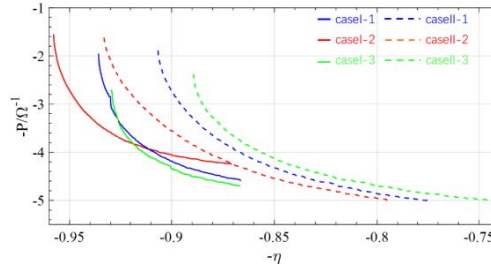


Fig. 5.2 Pareto Front for 6 cases

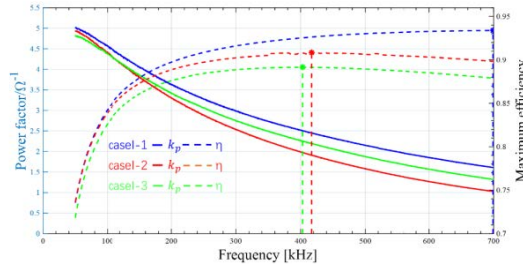


Fig. 5.3 Efficiency and power with respect to frequency for case I

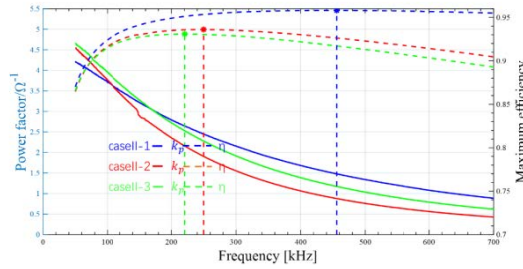


Fig. 5.4 Efficiency and power with respect to frequency for case II

The geometric meaning of points sharing same chebyshev distance is that they are on the same rectangle. In consequence, if there is a Pareto front on the performance space, we calculate the chebyshev distance from all the measurement points to the ideal vector and find the smallest value, which is the point where the rectangle from the ideal vector meets the Pareto front.

Compared with the optimization of adding different objective functions, this approach can find a non-convex Pareto front.

### 5.2.3 Optimization results

The cases of measurement are introduced in section 2.7.1. The results are shown in Fig. 5.2-4.

The Pareto front shows how the theoretical efficiency contract with theoretical power. It is observed from the optimization result that the range of optimal frequency is from 50 kHz to the frequency at the peak of the efficiency curve. To translate the optimization result, efficiency and power with respect to each frequency is plotted in Fig. 5.3 and Fig. 5.4. Considering the power is a decrease function and the efficiency curve is a uni-modal curve, the recommended frequency range is the frequency lower than the optimal frequency with respect to the efficiency. Comparing the optimal frequency under the presence or absence of ferrite and MLI material, it is concluded that both of them reduces the upper limit of the recommended operating frequency. The reason is both ferrite and MLI material cause intense increase in resistance of the coils, which leads to the reduce in optimal frequency with respect to the efficiency. The optimization result can be summarized as follows. Firstly, the operating frequency should be lower than the optimal frequency of the efficiency curve, considering the power is decreasing with respect to frequency. Secondly, because the ferrite and MLI reduces the optimal frequency of the efficiency curve, the operating frequency for the system with ferrite or MLI should be selected lower than frequency for systems without ferrite and MLI. The position of MLI also influences the frequency selection, in the cases which MLI is 1mm to the secondary coil, optimal frequency is lower than the cases MLI in the middle of two coils.

#### 5.2.4 Design Intuitions

The optimization result shows a wide-known design principle: the maximum power transfer capability of WPT decreases with resonant frequency. From this optimization result, it is referred that the operating frequency choosing for the WPT system should be lower than the optimal frequency of the efficiency curve. And with MLI and ferrite, the operating frequency is always lower than the cases without MLI and ferrite.

### 5.3 Air-gap efficiency Pareto Optimization

In section 5.3, two-dimensional finite element analysis tool FEMM, combined with Multi-Objective Evolutionary Algorithm based on Decomposition (MOEA/D), is used to optimize the working frequency and coil structure of WPT system. We hope to use the optimization results to give suggestions of air-gap to Lunar rover WPT coil design.



Table 5.1 Coil Specification in air-gap and efficiency Optimization

| Parameters            | Value | Unit |
|-----------------------|-------|------|
| Air-gap               | 10-30 | mm   |
| Diameter of Coils     | 130   | mm   |
| Coil layer limitation | 1     | NA   |
| Wire Diameter         | 0.9   | mm   |
| Pitch                 | 1.55  | mm   |
| Turns                 | 1-21  | NA   |
| Frequency             | 0-1   | MHz  |

Table 5.2 Experiment Result of MLI Influence on WPT [4]

| Frequency | Aluminized Layer | MLI with Slit |
|-----------|------------------|---------------|
| 100 kHz   | 0.967            | 0.987         |
| 678 kHz   | 0.838            | 0.966         |
| 1000 kHz  | 0.848            | 0.961         |

### 5.3.1 Design Background

Air-gap is a important design parameter for WPT systems. To find out the influence of airgap to the coil design and operation frequency selection, we carried out the multi-objective optimization for it. Tab. 5.1 is the optimization specifications. It is worth mentioning that according to the power transmission experiment of JAXA on MLI materials, we can get the effect of MLI materials on WPT efficiency at different frequencies. The influence is also considered in the optimization, the method is curve fitting. Tab. 5.2 shows experiment result of WPT with MLI, the data in Tab. 5.2 is the influence ratio of the influence of MLI or normal Aluminized Mylars towards the WPT efficiency. The considered MLI is of one layer, and the efficiency is viewed as 100 percent when there is no MLI.

### 5.3.2 Multi-Objective Optimization based on Decomposition

This is a widespread evolutionary approach towards Pareto optimization, proposed in 2007 [31]. The principle of MOEA/D is the same with our previously presented traditional method Chebyshev metric approach, but here it is implemented by the genetic algorithm.

A multi-objective optimization problem can be expressed as:

$$\begin{aligned} &\text{maximize } F(x) = (f_1(x), \dots, f_m(x))^T \\ &\text{subject to } x \in \Omega \end{aligned} \quad (5.8)$$

Where  $\Omega$  is called decision space, and  $F(x)$  consists of  $m$  objective functions. The multi-objective focus on cases where the objective functions contradict with each other, the best trade-offs among them is named Pareto optimally. In MOP, if a feasible decision satisfies at least one objective function superior to other choices, and all objective functions are not inferior to other choices, it is called Pareto optimal vector. The assemble of the Pareto optimal vectors is named the Pareto Front (PF).

Decomposition is a strategy in classic multi-objective optimization, the principle of it is using the weighted sum of the objectives or Chebyshev distance from the ideal solution to convert the multi-objective problem into single objective. Applying decomposition in the evolutionary optimization, a powerful Multi-Objective Evolutionary Algorithm based on Decomposition (MOEA/D) is proposed in recent years [10].

The principle of MOEA/D is to decompose the MOP into scalar optimization sub problems and solving them simultaneously. Applying evolutionary algorithm, a population of solutions composed of best solutions found so far for each subprograms is generated in every iteration. MOEA/D defines 'neighborhood' in the population to conduct crossover. A 'neighborhood' is composed of different points which is near each other in the objective space (the space of the objective functions). It is assumed in every 'neighborhood', the exchange of position information is meaningful for exploring the Pareto Front.

Several decomposition method has been developed in recent researches. Like the Pareto optimization based on measurement, the Chebyshev Approach is adopted. In this approach, MOP is converted into scalar optimization problem defined by the Chebyshev Matric towards the ideal solution.

$$\begin{aligned} &\text{minimize } g^{te}(x|\lambda, z^*) = \max_{1 \leq i \leq m} \{\lambda_i |f_i(x) - z_i^*|\} \\ &\text{subject to } x \in \Omega \end{aligned} \quad (5.9)$$

Where  $z^* = (z_1^*, \dots, z_m^*)^T$  is the reference point, named ideal solution, defined by:

$$z_i^* = \min \{f_i(x) | x \in \Omega\} \quad (5.10)$$

$\lambda$  is the weighting vector of each optimal point, respectively.

The steps of MOEA/D can be expressed as follows.

- Step 1: Initialization
  - Set  $EP = \emptyset$ , where External population is the population recorded and updated in every iteration.
  - Calculation the Euclidean distance between each weighting vectors and find out T closest weighting vectors to define a 'neighborhood' for each population.
  - Generate the initial population and ideal vector.
- Step 2: Iteration, for every iteration, repeat step 2 for every population.
  - Reproduction: randomly select two points in a neighborhood of point  $i$ , conducting crossover to exchange the position information of them.
  - Updating ideal vector  $z$ , for every  $z_j < f_j(y')$ , set  $z_j = f_j(y')$ .
  - Updating neighborhood: check every neighbors, if  $g^{te}(y'|\lambda^j, z) \leq g^{te}(x^j|\lambda^j, z^j)$ , set  $x^j = y'$ .
  - Updating EP.
- Step 3: When stopping criteria is satisfied
  - Stop the iteration.
  - Output the EP as the Pareto Front.

### 5.3.3 MOEA/D Optimization Results

The objective function is:

$$\eta_{WPT} = \eta_{\max} * \eta_{MLI} \quad (5.11)$$

Where for symmetric coils the WPT efficiency is:

$$\eta_{\max} = \frac{k^2 Q^2}{(1 + \sqrt{1 + k^2 Q^2})^2} \quad (5.12)$$

And the MLI ratio is calculated based on curve fitting of the measurement data.

MOEA/D is used to optimize the efficiency of combining WPT and inverter as one objective function, and the air-gap between the coils as another, individually. The WPT efficiency is calculated by equation 5.12, and the inverter loss is calculated at a input DC voltage of 20V at the equivalent load with the load is set to be at highest

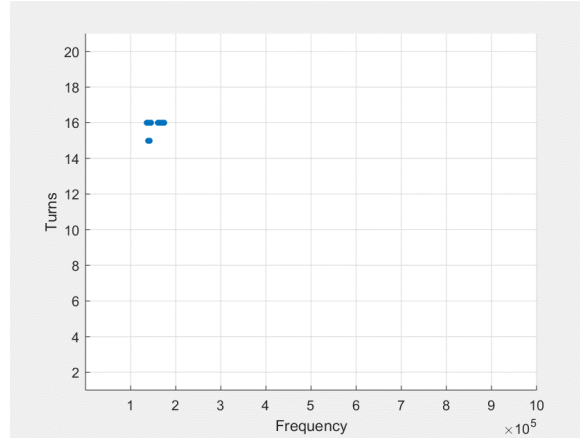


Fig. 5.5 Frequency and number of turns on Pareto Front

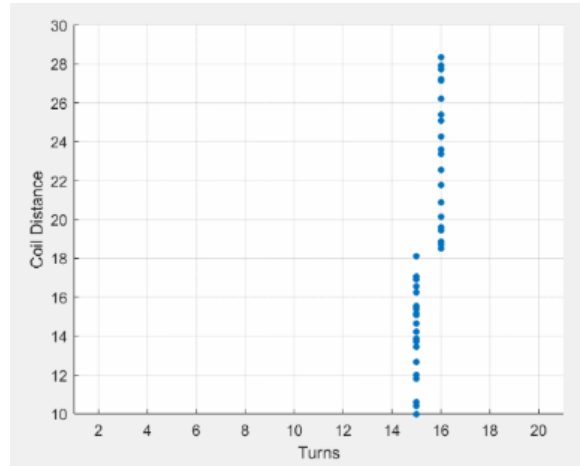


Fig. 5.6 Optimization Result of the Final External Population

WPT efficiency at each case, and based on the data from data-sheet [53]. There is a 5 degree phase difference for the current lagging the voltage in order to ensure a turn off current at the switching process.

### Number of turns and frequency

In Fig. 5.6, the design space of the final external population is shown. One can find that on the Pareto front, there is a positive correlation between the coil turns and the air-gap. The frequency in the final design space is limited to about 160 to 180 kHz, shown in Fig 5.5, and is distributed according to the air-gap. The number of turns is limited to 15 and 16, but the tendency is very apparent. If the distance between the coils is further improved, the number of turns may increase simultaneously.

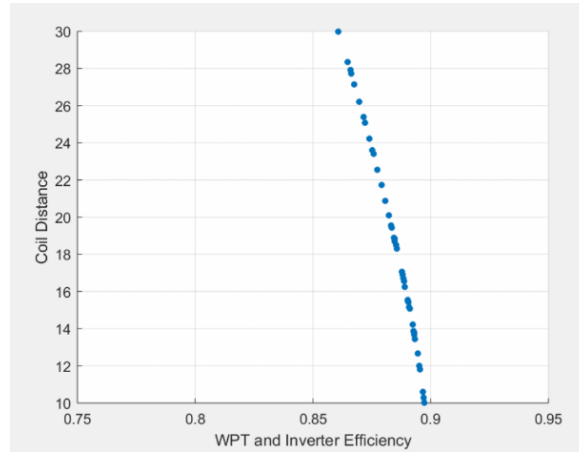


Fig. 5.7 Pareto Front of the Efficiency and Air-gap

### Pareto Front

PF is slightly convex, but not obvious. It shows that the WPT efficiency drop caused by Air-gap accelerates with the increase of air-gap.

### 5.3.4 Design Intuitions

From section 5.3, we can conclude:

- The optimal number of coil turns is positively related to the air-gap.
- We can notice the convergence of the number of turns and frequency. This shows that these design parameters are not greatly affected by air-gap, that is, mutual inductance.

However, the result in 5.3 is the result calculated by the conventional indicator  $KQ$  product, so frequency splitting is not considered. In order to make the design more able to reflect the impact of air-gap on WPT, we also took it into consideration in section 5.4.

## 5.4 Power Density and Thermal Density Pareto Optimization

This section is the most important part of Chapter 5. In Chapter 2, we introduced the mathematical model of PV and the loss calculation formulas of inverter, WPT,

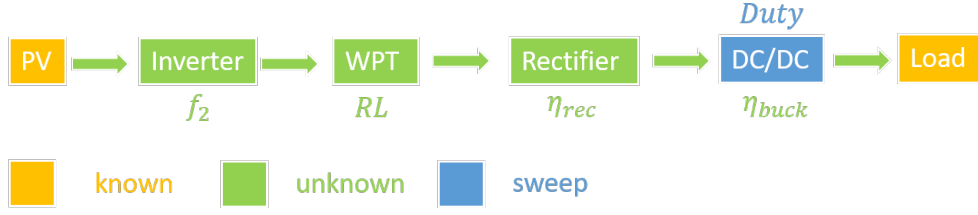


Fig. 5.8 Calculation method of PV-load Efficiency

rectifier, and DC-DC converter for the calculation of this section. In Chapter 3, we introduced the MPPT strategy considering frequency splitting, which is to determine the circuit state for the optimization of this section. In Chapter 4, we introduced the LPSO specially proposed for FEM optimization, and its multi-objective version will be applied in this section.

The cost function used in this section is different from previous WPT system optimization research. The input power in calculation comes from the mathematical model of PV, circuit state comes from MPPT strategy, and the optimization goal is the power density and thermal density of the system.

As far as the coil and frequency design of the lunar rover are concerned, the size of the coil determines the mass of the coil. Of course, we hope to reduce the mass of the coil. The heat dissipation per unit area determines the difficulty of the thermal design of the coil, because there is no heat convection in a vacuum environment, the heat dissipation problem is more important than the general WPT design.

#### 5.4.1 Implementation of L-MOPSO

In Chapter 4, we introduced a original modified algorithm LPSO, which is specially designed for the optimization of FE models. In this subsection, we are going to discuss its multi-objective version.

##### MOPSO

In order to consider several performance parameters, multi-objective PSO is considered. MOPSO shares similar velocity and position update equations with PSO, however, a repository is established with the non-dominated positions detected by particles. The 'global best' in single objective PSO is replaced by 'leader position', where 'leaders' for a certain particle is randomly selected in the repository. The proposed update equations in MOPSO is:

$$\vec{x}_t = \vec{x}_{t-1} + \vec{v}_t \quad (5.13)$$

$$\vec{v}_t = w\vec{v}_{t-1} + c_1 r_1 (\vec{p}_{t-1} - \vec{x}_t) + c_2 r_2 (\vec{l}_{t-1} - \vec{x}_t) \quad (5.14)$$

Where  $\vec{l}_{t-1}$  is the leader position.

### L-MOPSO

Based on the same consideration in Chapter 4, we considered a random velocity in the MOPSO velocity update equation.

$$\vec{v}_t = w\vec{v}_{t-1} + c_1 r_1 (\vec{p}_{t-1} - \vec{x}_t) + c_2 r_2 (\vec{l}_{t-1} - \vec{x}_t) + c_3 r_3 \vec{v}_m \quad (5.15)$$

Where the learning coefficients here, also obeys the Logistic distribution, the same as LPSO introduced in Chapter 4. We believe the exploration at the early stage of the algorithm will thus be improved.

### LMOPSO Tests

In order to observe the performance of the proposed algorithm, experiment on test functions is conducted. Test function in this section is ZDT3 shown in equation 5.16.

$$\begin{aligned} f_1(\vec{x}) &= x_1 \\ f_2(\vec{x}) &= g(\vec{x}) \left[ 1 - \sqrt{x_1/g(\vec{x})} - x_1/g(\vec{x}) \sin(10\pi x_1) \right] \\ g(\vec{x}) &= 1 + \frac{9}{n-1} (\sum_{i=2}^n x_i) \\ 0 &\leq x_i \leq 1, i = 1, \dots, n \end{aligned} \quad (5.16)$$

Two indicators representing the diversity and accuracy, namely spread [31] and IGD [54] is applied in the multi-objective test, smaller the spread and IGD is, better the diversity and accuracy will be.

$$Spread = \frac{d_f + d_l + \sum_{i=1}^{N-1} |d_i - \bar{d}|}{d_f + d_l + (N-1)\bar{d}} \quad (5.17)$$

Where  $d_i$  is the distance between two particles on solution set  $d_l$  and  $d_f$  are the distance between real boundary and optimized boundary.

$$IGD = \left( \sum_{i=1}^{N^*} d_i \right) / N^* \quad (5.18)$$

Where  $N^*$  is the evenly selected point on the real pareto front. The result is shown in table 1. The result shows the proposed LMOPSO possesses slightly better diversity than MOPSO, MOEA/D and NSGA-III.

Table 5.3 Comaprison of LMOPSO and conventional algorithms

| Algorithm | Spread | IGD    |
|-----------|--------|--------|
| LMOPSO    | 0.7050 | 0.0148 |
| MOPSO     | 0.7137 | 0.0149 |
| MOEA/D    | 0.8600 | 0.2355 |
| NSGAIII   | 0.7266 | 0.0174 |

Based on the above verification, we believe that the proposed LMOPSO has certain advantages over previous multi-objective optimization methods, so this method is adopted in the optimization.

#### 5.4.2 Cost Functions

Figure 5.10 shows how we calculate the efficiency of each part of the system. Our power source is a PV cell, it is not appropriate to do optimization under a certain voltage for this power source. Fortunately, we know the series-parallel connection of the solar cell module and the U-I diagram of each component. In consequence, we can build a mathematical model of the planned PV output by using the parameters estimated in Chapter 2. According to the admittance model of the WPT resonant circuit we have adopted, we can find the input resistance of the PV when  $R_L$  is determined. Substituting it into the PV model, we can determine the output of the PV.

Therefore, the core problem of our calculation is to find the  $R_L$ , determine the operating frequency  $f_2$ , once frequency splitting occurs, immediately track the high resonance point, which is completely consistent with the MPPT method proposed in Chapter 3.

The method of the operation status determination is completely consistent with the MPPT content in Chapter 3. We sweep the duty cycle of the secondary side DC-DC converter with a certain step length, determine the working status based on this, record all the working status, select MPP, and finally compare the different designs' performance at the MPP point.

Among them, the most important thing is that we cannot get an explicit solution regardless of the output of PV or  $R_L$ , so we use an iterative solution in which the relaxation factor changes with iteration. The output of PV is the inner loop and  $R_L$  is



the outer loop. After both of them converge, we proceed to the next step of the duty cycle sweeping.

Because this part cost the author a lot of effort, he would like to briefly introduce the derivation algorithm of the cost functions.

- Step 1: Initialization

- Set all efficiency as 100 percent.
- Set coil parameters from FEMM simulation (this part is determined by LMOPSO iteration and FEMM script).
- Set  $R_{DC}$  value.
- Initialize MOSFET data, inductor and capacitors.
- Initialize Relaxation factors  $k_s$  for PV loop and  $k_l$  for  $R_L$  loop.
- Initialize PV property through parameters estimated and following equations.

$$I_{ph} = [I_{sc} + k_i \cdot (T - 298)] \cdot \frac{G}{1000} \quad (5.19)$$

$$I_0 = I_{rs} \cdot \left(\frac{T}{298}\right)^3 \cdot \exp \left[ \frac{q \cdot E_{go} \cdot (1/298 - 1/T)}{n \cdot k} \right] \quad (5.20)$$

$$I_{rs} = \frac{I_{sc}}{e^{\left(\frac{q \cdot V_{oc}}{n \cdot k \cdot T}\right)} - 1} \quad (5.21)$$

- Step 2: Duty sweep, for every iteration, repeat step 2 and duty + duty step
  - Step 2.1: While 1, do
    - \* Determine input voltage for inverter trough

$$V_m = 4 * \frac{V_{pv}}{\pi} \quad (5.22)$$

This equation is derived from the Fourier expansion of voltage. Where  $V_m$  is the magnitude of the sine wave voltage and  $V_{pv}$  is the magnitude of PV voltage.

- \*  $R_L$  determination by

$$R_{buck} = \frac{R_{dc}}{D^2} * \eta_{buck} \quad (5.23)$$

$$R_L = \frac{8 * R_{buck}}{\pi^2 * \eta_{rect}} \quad (5.24)$$

These two equation are derived from conservation of energy. Where  $R_{buck}$  is the equivalent resistance of DC-DC converter, while  $R_{dc}$  is the equivalent resistance of the load.

\* Frequency splitting detection. If

$$4M^2 + C^2 (R + R_L)^4 - 4LC (R + R_L)^2 > 0 \quad (5.25)$$

\* and

$$2L - C (R + R_L)^2 - \sqrt{4M^2 + C^2 (R + R_L)^4 - 4LC (R + R_L)^2} > 0 \quad (5.26)$$

· Do

$$\omega_2 = \sqrt{\frac{2L - C (R + R_L)^2 + \sqrt{4M^2 + C^2 (R + R_L)^4 - 4LC (R + R_L)^2}}{2C (L^2 - M^2)}} \quad (5.27)$$

· else

$$\omega_2 = \omega \quad (5.28)$$

\* Operation frequency determination

$$f_2 = \frac{\omega_2}{2\pi} \quad (5.29)$$

\* Determine WPT loop properties by:

$$z_1 = z_2 = R_1 + sL_1 + \frac{1}{sC_1} = R_2 + sL_2 + \frac{1}{sC_2} \quad (5.30)$$

$$DEN = -s^2 * M^2 + z_1 * z_2 + z_1 * R_L \quad (5.31)$$

$$Y1 = \frac{z_2 + R_L}{DEN} \quad (5.32)$$

$$Y2 = \frac{s * M}{DEN} \quad (5.33)$$

$$I_m = V_m * |Y1(j\omega_2)| \quad (5.34)$$

$$I_{m2} = V_m * |Y2(j\omega_2)| \quad (5.35)$$

$$V_{m2} = I_{m2} * R_L \quad (5.36)$$

$$\eta_{\text{wpt}} = \frac{P_2}{P_1} = R_L \cdot \frac{|Y_2|^2}{\text{Re}(Y_1)} = R_L \cdot \frac{|Y_2|^2}{|Y_1| \cos(\angle Y_1(j\omega_2))} \quad (5.37)$$

\* Inverter loss estimated by

$$P_{\text{inv}} = I_m^2 r_d + 4f(t_r/3 + t_f/2) V_{pv} I_m \sin(\angle Y_1(j\omega_2)) + 4f Q_g V_g \quad (5.38)$$

\* Inverter output power estimated by

$$P_{\text{out}} = \frac{I_m V_m}{2 \cos(\angle Y_1(j\omega_2))} \quad (5.39)$$

\* Inverter efficiency update

$$\eta_{\text{inv}} = \frac{P_{\text{out}}}{P_{\text{in}} + P_{\text{out}}} \quad (5.40)$$

\* Rectifier efficiency update

$$\eta_{\text{rec}} = 1 - \left( \frac{8VF}{\pi V_{m2}} + \frac{2RF}{RL} + \frac{8rc}{\pi^2 RL} \times \left( \frac{\pi^2}{8} - 1 \right) \right) \quad (5.41)$$

Where  $VF$  is the forward voltage of the diodes,  $RF$  is the conduction resistance of the diodes and  $r_c$  is the ESR of the filter capacitor.

\* DC-DC converter operation condition determination

$$V_{\text{dcdcin}} = V_{\text{rectout}} = \frac{\pi}{4} * \eta_{\text{rect}} * V_{m2} \quad (5.42)$$

For current driven rectifier, due to conservation of energy, the loss in rectifier causes voltage drop.

$$V_{\text{dcdcout}} = D * V_{\text{dcdcin}} \quad (5.43)$$

$$I_{\text{dcdcout}} = V_{\text{dcdcout}} / R_{dc} \quad (5.44)$$

$$\Delta I = \frac{V_{\text{dcdcin}} - V_{\text{dcdcout}}}{f_{sw} * L_{\text{buck}}} D \quad (5.45)$$

Where  $\Delta I$  is the ripple of the converter at continuous conduction mode. Here, synchronous rectification type buck converter is applied. In other topology, the equations can be replaced by the real condition.

Based on these parameters, we could estimate the efficiency of buck converter.

\* Loss estimations

$$P_{\text{cinloss}} = \left( D \sqrt{1-D} * I_{\text{dcdcout}} \right)^2 * r_c \quad (5.46)$$

We know that for the buck converter, the input is not a direct current, but a rectangular wave. After the half-wave sinusoidal current of the resonance circuit is filtered by the input capacitor of the buck converter, the approximate square wave absorbed by the buck converter also flows from the capacitor.

Integrate according to the waveform, and we calculate the AC current flowing into and out of the capacitor according to the superposition principle.

$$P_{\text{on}} = \left( I_{\text{dcdcout}}^2 + \frac{\text{Deltal}^2}{12} \right) * R_{ds} \quad (5.47)$$

In addition, the switching loss is estimated as follows.

$$P_{\text{sw}} = (V_{\text{dcdc}} + VF) * I_{\text{dcdc}} * \left( \frac{t_r}{3} + \frac{t_f}{2} \right) * f_{\text{sw}} \quad (5.48)$$

If the ripple is large, it will produce more obvious eddy current loss when flowing through the inductor. However, in our design, a large inductance is used to suppress the ripple, so only the DC resistance considered at this time.

$$P_{\text{ind}} = \left( I_{\text{dcdc}}^2 + \frac{\text{Deltal}^2}{12} \right) * DCR \quad (5.49)$$

In addition, the output of dcdc converter also consists ripple, which is filtered by the output capacitor.

$$P_{\text{closs}} = \frac{\text{Deltal}^2}{12} * r_{\text{cbuck}} \quad (5.50)$$

\* Update the buck efficiency

$$\eta_{\text{buck}} = \frac{V_{\text{dcdcout}} * I_{\text{dcdcout}}}{(V_{\text{dcdcout}} * I_{\text{dcdcout}} + P_{\text{on}} + P_{\text{sw}} + P_{\text{cinloss}} + P_{\text{ind}} + P_{\text{closs}})} \quad (5.51)$$

\* Update PV input resistance

$$R_T = \frac{\pi^2}{8 \cos(\angle Y1(j\omega_2)) |Y1(j\omega_2)|} \quad (5.52)$$

\* While 1 (the second inner loop)

- Reduce the relaxation factor  $k_s$  by a certain ratio
- Update PV output current by

$$I_{pv} = (I_{pv} - I_{pv\text{last}}) * k_s + I_{pv\text{last}} \quad (5.53)$$

$$I_{pv\text{last}} = I_{pv} \quad (5.54)$$

$$V_{pv} = I_{pv} * R_T \quad (5.55)$$

$$I_{sh} = \left( \frac{V_{pv} + I_{pv} \cdot R_s}{R_{sh}} \right) \quad (5.56)$$

$$I_{pv} = I_{ph} - I_0 \cdot \left[ \exp \left( \frac{q \cdot (V_{pv} + I_{pv} \cdot R_s)}{n \cdot k \cdot T \cdot N_s} \right) - 1 \right] - I_{sh} \quad (5.57)$$

· if  $I_{pv}$  convergence

1.  $k_s$  restore original value
2. Record the circuit status
3. Break second inner loop

\* if  $R_L$  convergence 1.  $k_l$  restore original value 2. Break inner loop

\* Update  $R_L$  by

$$R_L = (R_L - R_{L\text{last}}) * k_l + R_{L\text{last}} \quad (5.58)$$

$$R_{L\text{last}} = R_L \quad (5.59)$$

Note the  $R_L$  in step 2.1 is the temporary value determined by the newly updated several efficiencies, and these efficiencies were calculated by  $R_L$  from last iteration of step 2.1, so they are not the accurate value, either. We need to repeat step 2.1 until  $R_L$  and the efficiencies convergence to the final results.

- \* Reduce  $k_l$  by a certain ratio.
- Repeat step 2.1
- Step 3: When duty sweep stopping criteria is satisfied
  - Stop the outer iteration (sweep).
  - Find out the MPP result
  - Calculate power density of coils

$$\text{power-density} = P_{\text{output}} / \iiint dv \quad (5.60)$$

- Calculate thermal density of coils

$$\text{thermal-density} = P_{\text{loss-WPT}} / \iint dA \quad (5.61)$$

- Output [*power – density, thermal – density*]

### 5.4.3 Optimization Results

In this subsection, the optimization result of the power-density and thermal-density optimization will be briefly introduced, physical meaning of optimization results will be introduced.

#### Pareto front of power-density and thermal-density designs

Each iteration of the algorithm, as mentioned before, is updated by the LMOPSO algorithm under the result of the previous iteration, and the new non-dominant feasible solutions are added to the Pareto Front obtained from the previous iteration.

And the evolution of PF is shown in Fig. 5.11. At the beginning, there was no Pareto front, as shown in (a). After one iteration, a few non-dominated solutions were selected, and with the iteration, more and more low thermal density and high power density results were discovered by the algorithm.

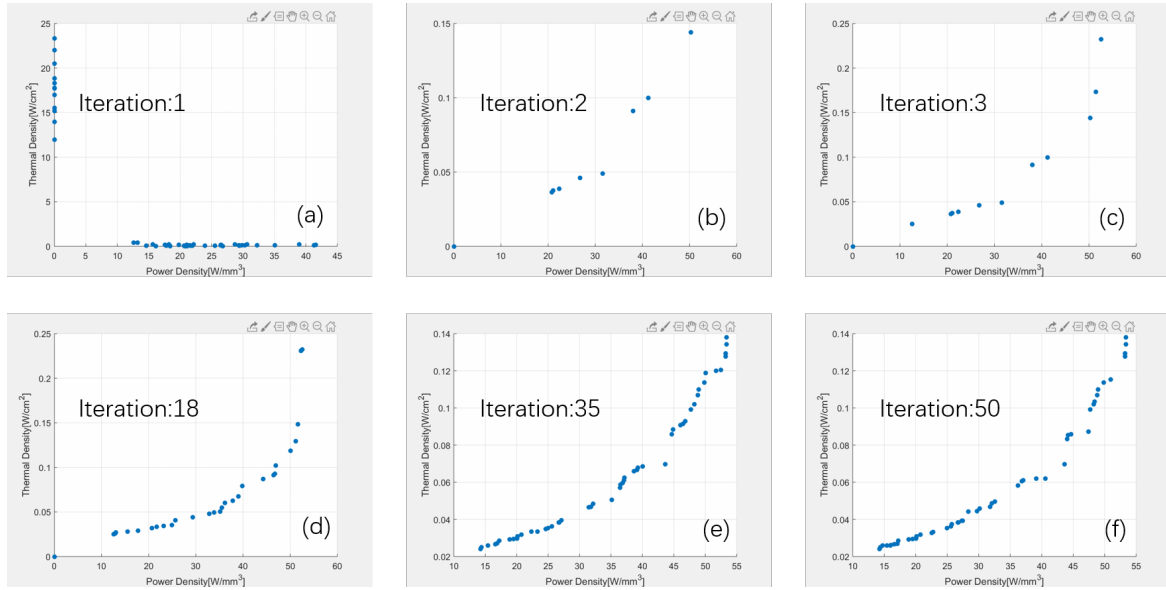


Fig. 5.9 Pareto Front of the power density and thermal density

In the end, we got a solution set, all within the solution set are Pareto optimal designs. The thermal density ranges from  $0.2\text{W}/\text{cm}^2$  to  $1.4\text{W}/\text{cm}^2$ , and the power density ranges from about  $14\text{W}/\text{mm}^3$  to about  $54\text{W}/\text{mm}^3$ . When we improve any one of these parameters, it will lead to the deterioration of the other parameter.

The Pareto front is convex, which means that starting from its center, the improvement of thermal density due to deterioration of power density is diminishing marginal utility, vice versa. Therefore, the design at the center of the Pareto front is a relatively balanced and feasible.

### Designs parameters on the Pareto front

Next we would like to discuss what design parameters the Pareto optimal solutions corresponds to.

In order to show the distribution of various design parameters on the PF obtained in this section, we have identified them with different color-bars.

- Frequency

First of all, we get that the higher the designed resonance frequency, the greater the power density of the coil, and the thermal density of the coil also increases with the operating frequency. This conclusion is the same as our experience, because the design frequency of small WPT systems is often higher. However, the fact that there is a big difference in such a narrow frequency range is

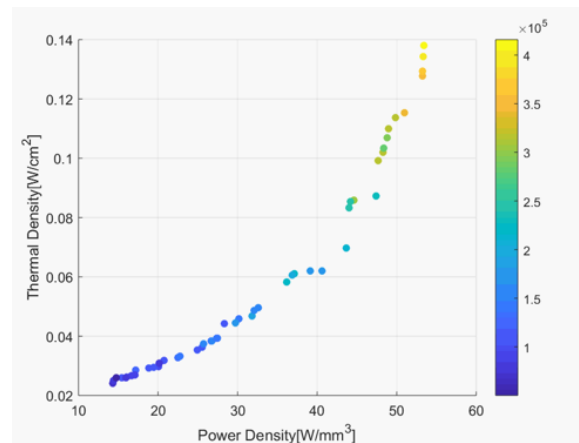


Fig. 5.10 Frequency on Pareto Front

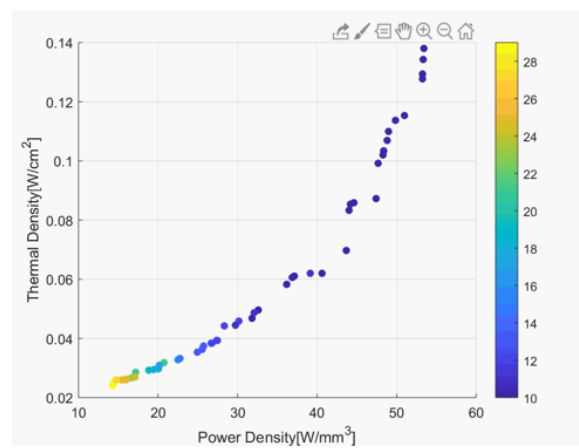


Fig. 5.11 Number of turns on Pareto Front

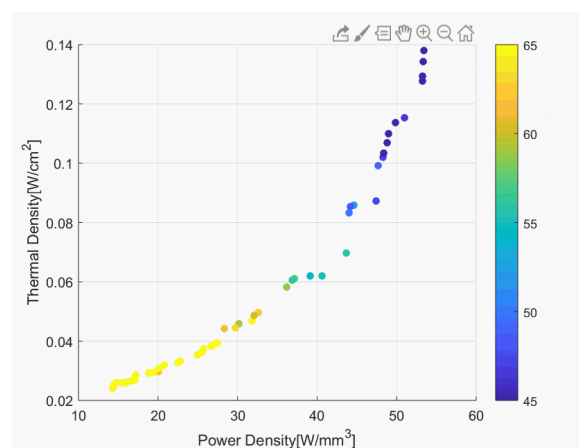


Fig. 5.12 Coil outer diameter on Pareto Front



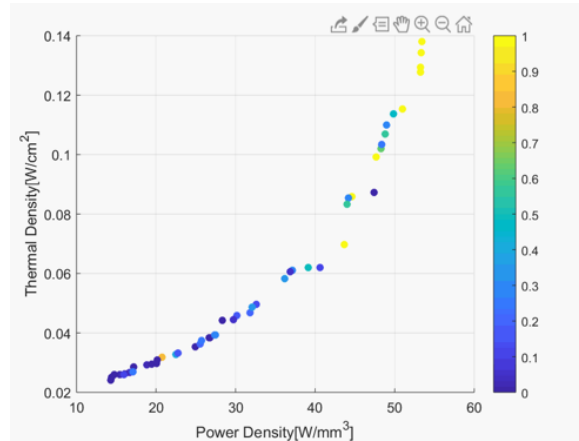


Fig. 5.13 Pitch on Pareto Front

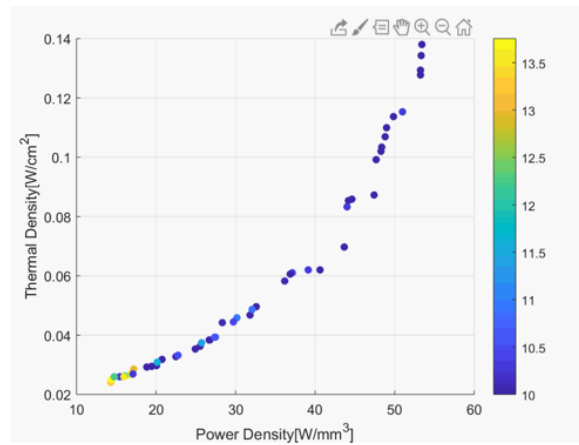


Fig. 5.14 Air-gap on Pareto Front

still beyond the author's expectation. The author believes the variation of power-density on the Pareto front is majorly caused by the change of coil turns and diameter.

- Number of Turns

When we observe the change of the number of turns on the Pareto front, we will find that its trend is exactly opposite to the frequency. In other words, for the designs of lower frequency, relatively speaking, the power density is smaller, the number of turns is larger, and the thermal design is easier.

- Outer diameter

It is generally believed that the diameter of the coil should be enlarged when designing the WPT coil. But this is the conclusion when considering the

absolute value of efficiency. Our design indicators are power density and thermal density, which gives us the possibility to compare coils of different diameters. According to the optimization results, we believe that the influence of coil size on the optimal results is opposite to frequency. The large coil is suitable for low frequency, and the small coil is suitable for high frequency, which is consistent with our experience.

- Air-gap

The variations of air-gap on Pareto front is beyond our expectations. It is generally believed that high frequency design is more prone to frequency splitting. However, according to our optimization results, air-gap converges to its minimum value under high frequency conditions, but air-gap does not converge to a fixed value under low frequency conditions. The lower the frequency, the greater the diversity in air-gap. However, even so, considering that the initial design range is  $10 - 30mm$ , and the final air-gap is less than  $14mm$ , the experience that reducing the air-gap helps to improve the efficiency of WPT is still applicable.

It is worth mentioning that although the optimization in section 5.4 is completely different from that in section 5.3, the positive correlation between air-gap and the number of coil turns is similar.

- Pitch

The trend of pitch is the same as frequency, and the trend of coil diameter, air-gap and number of turns is opposite. In the case of high frequency, a small coil with a small number of turns and a large pitch has a high power density. In the case of low frequency, which in this optimization, that is, in the case of less than  $150kHz$ , the pitch of most optimization results converges to 0.

## Design Intuition

Based on the above observations, we can conclude the following intuitions:

Low frequency, large coils are suitable for situations where heat dissipation is difficult. In this case, the pitch is zero and a larger number of turns is required.

If the heat dissipation requirements are not strict, the design of high frequency, small coil, and large pitch can significantly increase the power density.

For the lunar rover, heat dissipation is obviously more important than power density, so we chose a large coil with a higher number of turns as our design example.

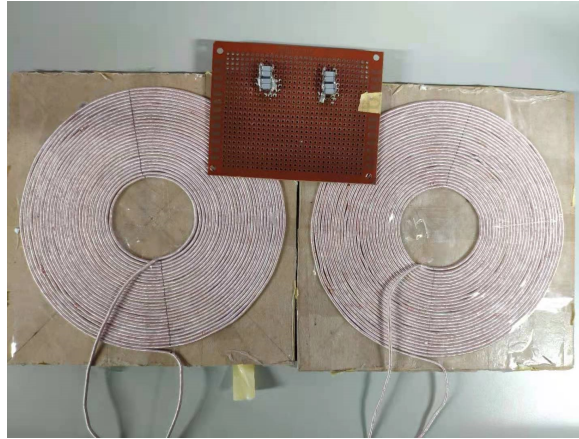


Fig. 5.15 Low thermal density coil Example

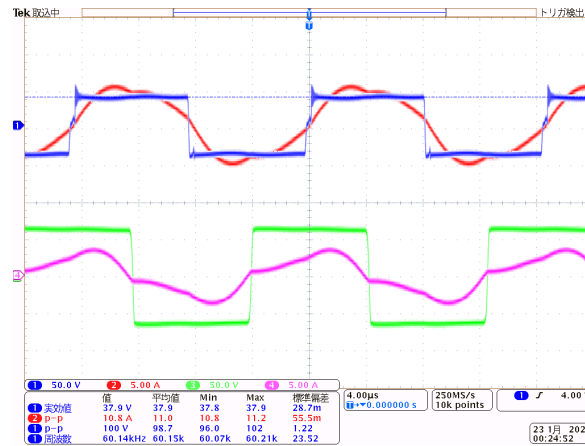


Fig. 5.16 Experiment waveform of Low thermal density coil Example

#### 5.4.4 Selected Design Example and Experiment

In order to simplify the thermal design difficulty to the greatest extent, we chose a design example of 65mm radius, 29 turns, 0 pitch and 57.1kHz, and conducted experimental measurements.

In the experiment, the PV output curve we estimated in Chapter 2 is applied as power source, realized by the PV simulator Agilent E4350B. The implemented maximum theoretical output is 130Watt, and the MPPT strategy is the duty sweep method and 2-dimensional PSO method proposed in Chapter 3 in which the inverter frequency is adjusted with frequency sweeping.

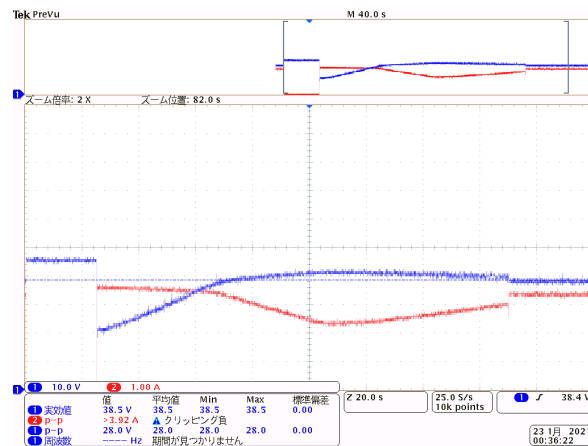


Fig. 5.17 PV output of sweep experiment

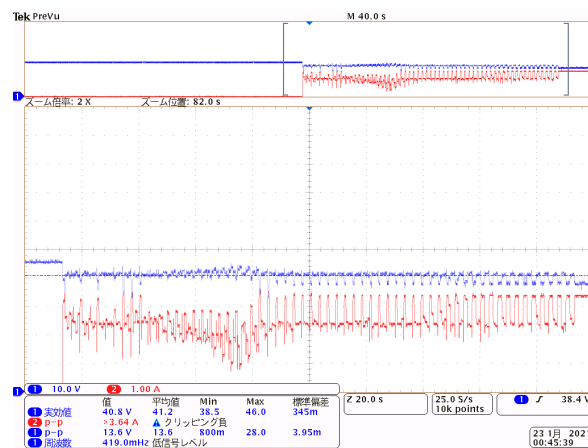


Fig. 5.18 PV output of PSO experiment

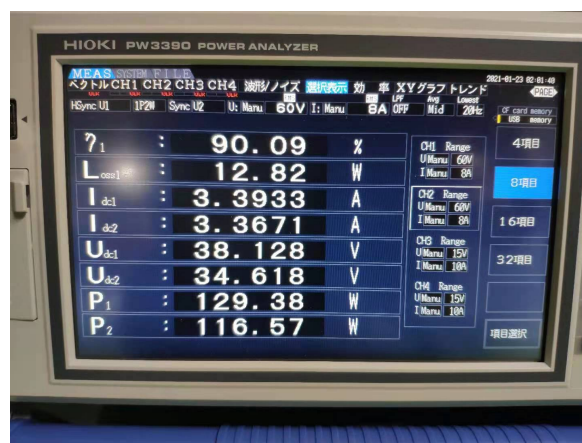


Fig. 5.19 PV-Load efficiency of sweep experiment

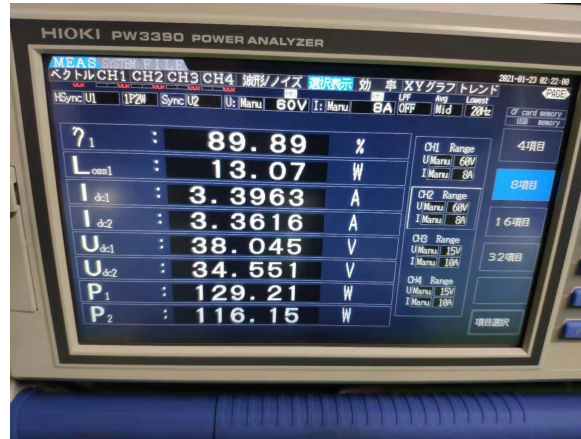


Fig. 5.20 PV-Load efficiency of PSO experiment

### Sweep MPPT with frequency adjustment

For the sweep method, we estimate  $\omega_2$  based on the measurement data of the coil to ensure that the voltage of the inverter never lag behind the current during the entire duty sweep process.

In the end, the convergence result has a PV-to-Load efficiency of 90.09 percent and 99.52 percent MPPT efficiency.

### 2-D PSO MPPT

This method does not require accurate measurement data and converges to 89.89 percent PV-Load efficiency and 99.39 percent MPPT efficiency.

## 5.5 Summary

In this chapter, we performed multi-objective optimizations of the Lunar Rover WPT system. Based on traditional chebyshev metric approach and measurement data, we concluded operation frequency should be less than the efficiency peak frequency. Through airgap-efficiency optimization by MOEA/D, we can infer narrowing the air gap can improve efficiency, but the improvement effect is marginal, moreover, reducing the airgap has an impact on the optimal number of turns of the coil.

Simultaneous optimization of power density and thermal density is an important content in this chapter. From the optimization results, we conclude that coils with low frequency, high turns, and low pitch can meet the planned power for lunar rover while minimizing the thermal density.

The experimental results show that our optimized coil example together with our proposed MPPT method can achieve over 90 percent efficiency while conducting MPPT. Compared with the 75 percent efficiency of the previous lunar rover prototype, the efficiency is significantly improved.

## Chapter 6

# Evaluation of JAXA's Coil Design

In order to find the optimal coil structure and consider the optimal operation frequency, JAXA has done a series of power transmission experiments. The experiments mainly includes the comparison of WPT efficiency of different coil sizes at different frequencies, the comparison of WPT efficiency of different coils of the same size and different turn number, and the comparison of transmission efficiency of different coil shapes with the same turn number and diameter. However, due to the time and cost limitations of the experiment, we are not able to manufacture real coil models in all cases, and it is not possible to carry out the power transmission experiment at all frequencies. Therefore, there are only few examples of comparison in the experiments, such as the comparison of several groups of data. Consequently, it is difficult to draw accurate conclusions considering a continuous design space. Therefore, the design of virtual prototype based on FEM is essential to supplement and explain the experiment results of coil design. In addition, the author believes the Pareto optimization and meta-heuristic algorithms may give us a point of view different from the intuitive experiments, and provide us with some useful design inspiration.

So in this chapter, optimization is used as scene reconstruction for JAXA's experiment. Benefit from the small cost of FEM than experiment, we can implement optimization in continuous design spaces. And the position of the design selected by experiment will be shown on the Pareto Fronts.



Fig. 6.1 Coil Manufactured in the experiments

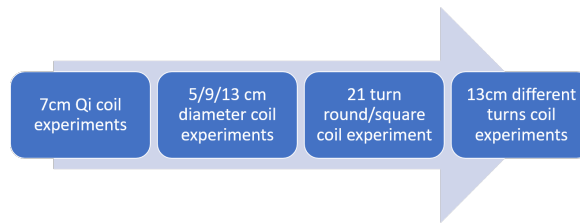


Fig. 6.2 Process of coil design experiments

## 6.1 Brief Introduction to Coil Design Experiments

In order to find a suitable coil and working frequency, using manufactured coil and VNA measurements, JAXA did some experiments. The first thing to determine is the size of the coil. The initial size of the coil is planned to be 7cm, and Qi-A11 coil is used for design. However, a series of experimental results showed that the DC-DC efficiency at that time was only less than 70 percent. As a result, several coils of different sizes were made and experimental comparisons were carried out.

After comparing the diameter of 5-7-9-13 cm, the experiment results show that the efficiency of the 13 cm coil is higher, so the 13 cm diameter coil is selected. Next, round and square coils were compared. Round coil is selected.

Finally, coils with different turns were compared. In the comparison of 9-21 turns, 21 turns were selected. The manufactured coils are shown in Fig. 6.1, as well as the design process based on the experiments in Fig. 6.2.

Here we apply out multi-objective optimization in continuous design space, to check the position of the selected design in the experiment.

### 6.1.1 Experiment Setup and FE Reproduction

The fixed and variant parameters in the optimization in this section is shown in table 6.1.



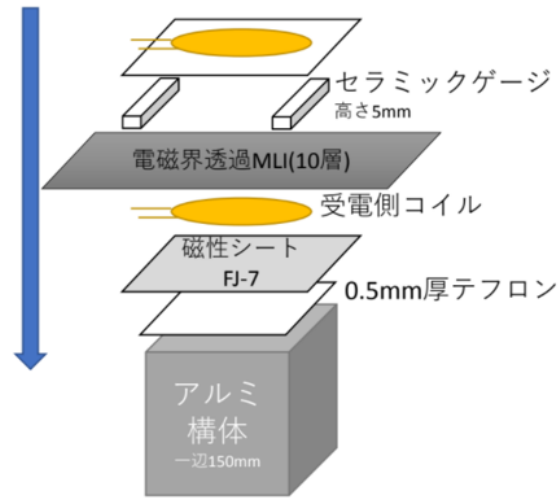


Fig. 6.3 Experiment illustration of JAXA's Coil Design

Table 6.1 Coil Specification in JAXA Experiment and Optimization [4]

| Parameters            | Value     | Unit |
|-----------------------|-----------|------|
| Air-gap               | 10        | mm   |
| Diameter of Coils     | 130       | mm   |
| Coil layer limitation | 1         | NA   |
| Wire Diameter         | 0.9       | mm   |
| Pitch                 | 1.55      | mm   |
| Turns(Experiment)     | 9/15/21   | NA   |
| Frequency(Experiment) | 0.2/0.6/1 | MHz  |

During the experiment, in order to better simulate the real situation, JAXA used aluminum materials similar in size to the lunar rover around the WPT coil. And used MT-MLI to place between the coils.

The specific experimental method is VNA measurement. VNA can scan the frequency of  $S_{21}$ . And  $S_{21}$  is interpreted as the ratio of the amplitude of the output voltage traveling wave to the input voltage traveling wave amplitude. Thus its square is the ratio of the energy of the input and output voltage traveling waves.

At the beginning of WPT research in the 2000s, WPT efficiency evaluation was often carried out using S parameters. If we use circuit parameters to express it, it is Equation 6.1.

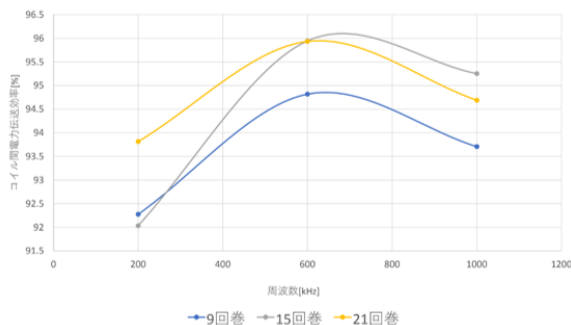


Fig. 6.4 Result of coil design experiments

### 6.1.2 Cost Functions

$S_{21}$  can be intuitively interpreted as the efficiency in the case of impedance matching (that is, the equivalent resistance of the WPT circuit input and output is  $50\Omega$ ).

$$S_{21}(\omega) = \frac{2jL_m Z_0 \omega}{L_m^2 \omega^2 + \left\{ (Z_0 + R) + j\left(\omega L - \frac{1}{\omega C}\right) \right\}^2} \quad (6.1)$$

Where for normal measurement,  $Z_0$  is the output resistance of the source and the input resistance of the load, set as  $50\Omega$ .

### 6.1.3 Result

Trough measurement, JAXA concluded the optimum design should be about 500 kHz to 600 kHz, and the coil should possess a large number of turns.

In the experiment, 15 turn coil performance in high efficiency is better, but considering the 21 turn coil's efficiency distribution in the frequency range is more even than 15 turn design, which benefits the selection of operation frequency, JAXA determined to use 21 turn coil for the design prototype.

## 6.2 Single Objective Optimization for Experiment Reproduction

Single objective optimization using the traditional WPT evaluation method  $KQ$  product with the consideration of MLI is firstly conducted. The objective function is:

$$\eta_{WPT} = \eta_{\max} * \eta_{MLI} \quad (6.2)$$

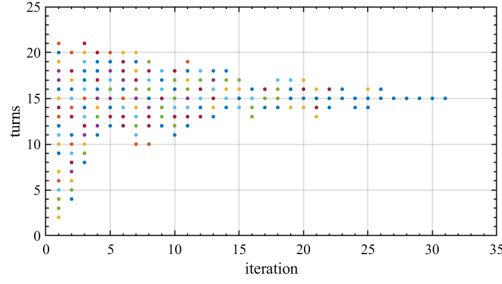


Fig. 6.5 Single objective optimization-number of turns

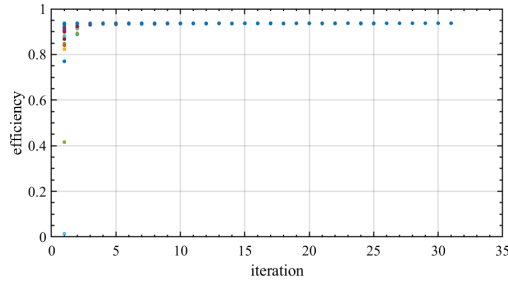


Fig. 6.6 Single objective optimization-efficiency

Where for symetric coils the WPT efficiency is:

$$\eta_{\max} = \frac{k^2 Q^2}{(1 + \sqrt{1 + k^2 Q^2})^2} \quad (6.3)$$

And the MLI ratio is calculated based on curve fitting of the measurement data.

Today's WPT systems generally use the efficiency obtained by the  $KQ$  product for evaluation, so we also use the  $KQ$  product for optimization in this section.

## Result

The single objective optimization is based on particle swarm optimization, and the result of frequency, efficiency and number of turns convergence is shown in the figures. The best efficiency is 93.7 percent, at 568  $\text{kHz}$  and 15 turn.

We found that the result is basically the same as the optimal coil obtained by JAXA measurement. However, the relationship between the optimal number of turns and the frequency is not the same. We believe this is caused by the difference in evaluation indicators.

Therefore, on this basis, we carried out multi-objective optimization of both  $S_{21}$  and  $KQ$  product.

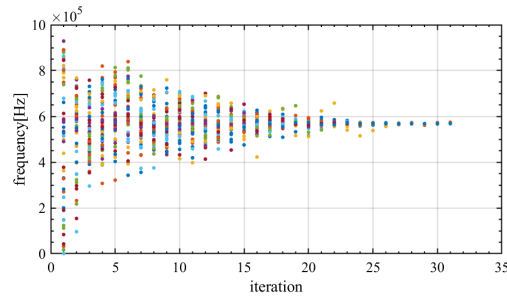


Fig. 6.7 Single objective optimization-frequency

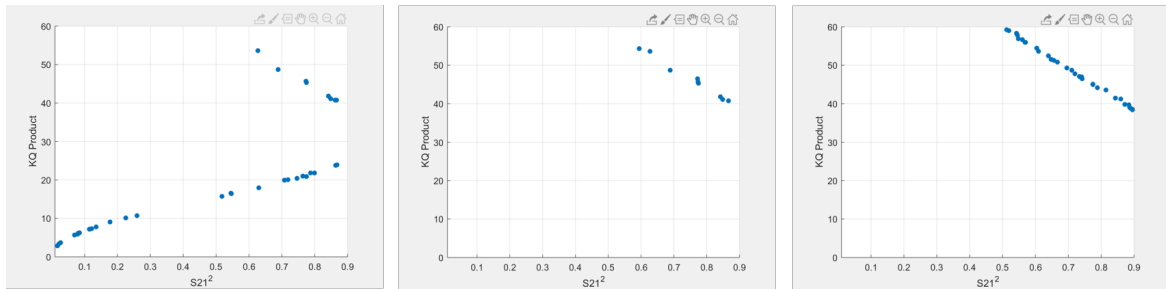


Fig. 6.8 Pareto Front convergence

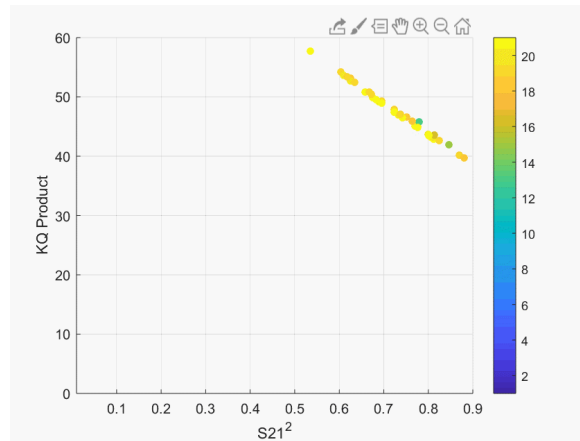


Fig. 6.9 Number of turns on Pareto Front

### 6.3 Multi-Objective Optimization for Experiment Reproduction

In this section, we repeated the optimization experiment of JAXA, with both  $KQ$  product and  $S_{21}$  as our optimization objects. The method we use is the L-MOPSO proposed in this thesis. We adopted the same coil structure and design parameters

as JAXA, but replaced the aluminum structure in the experiment with an FE model of an aluminum disc.

### 6.3.1 Cost Functions

From an intuitive point of view, as mentioned in the derivation of the  $KQ$  product in Chapter 2, the  $KQ$  product represents the theoretical maximum efficiency of the WPT system. And  $S_{21}$  represents the efficiency at maximum power transmission.

$$\eta_{\max} = \frac{k^2 Q_1 Q_2}{\left(1 + \sqrt{1 + k^2 Q_1 Q_2}\right)^2} \quad (6.4)$$

$$S_{21}(\omega) = \frac{2jL_m Z_0 \omega}{L_m^2 \omega^2 + \left\{(Z_0 + R) + j\left(\omega L - \frac{1}{\omega C}\right)\right\}^2} \quad (6.5)$$

In this optimization, we consider these two indicators and observe the position of the experimental results on the Pareto front, hoping to provide a theoretical explanation for JAXA's experiment by our optimization method.

### 6.3.2 Optimization Results

In the optimization of this section, the design parameters are coil size, frequency and number of turns.

Although our design parameters are randomly distributed, the PF still has a certain regular pattern at the first iteration. This shows the intrinsic relationship between the two objective functions.

#### Pareto Front

For these two objective functions, PF is not concave nor convex, so we believe that, unlike the optimization in Chapter 5, the two objective functions do not have diminishing marginal utility.

#### Frequency

We can see that even if the surrounding aluminum material is considered, when our optimization goal is the original nature of WPT, the optimum design still has a trend toward high frequency.

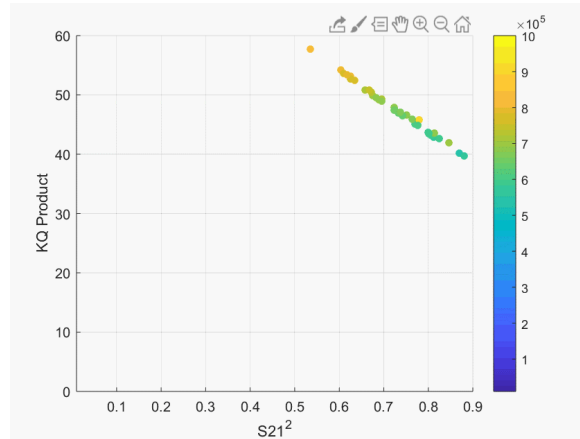


Fig. 6.10 Frequency on Pareto Front

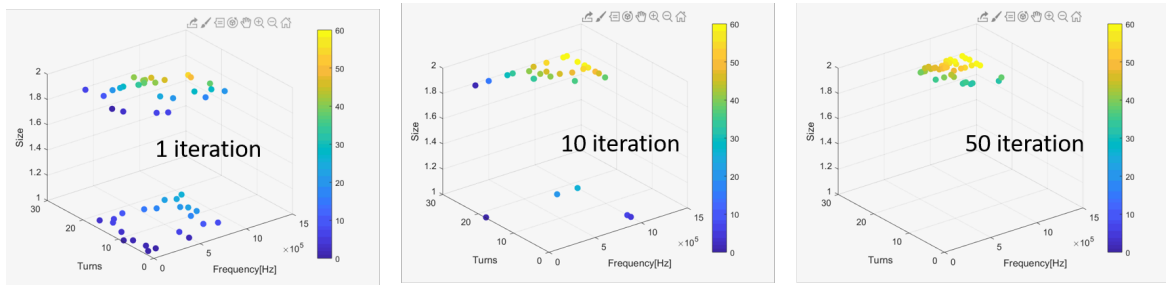


Fig. 6.11 KQ product on Pareto Front

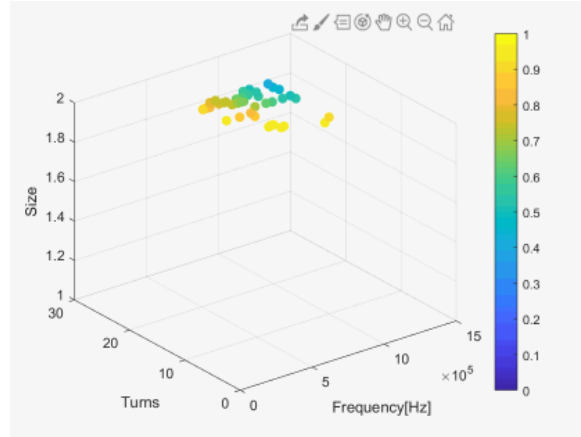
Especially for  $KQ$  product, the only limitation of high frequency on  $KQ$  comes from the increase of  $R_{ac}$  caused by eddy current loss, but it is not important compared with the improvement of quality factor.

### Number of Turns

The optimization results of turns show that high turns are beneficial to both objectives. The author believes that this result is due to the fact that there is a fixed pitch in the experiment and the upper limit of number of turns of coil has not been set to the center.

### Position of Experiment Result in the Performance Space

The result of the algorithm selects a large coil between a large coil and a small coil, which is reflected in all points converging on the upper plane. Note that the upper and lower planes represent different coil areas.

Fig. 6.12  $S_{21}$  on Pareto Front

Moreover, the particles on the Pareto Front are fan-shaped with high frequency and high turns as the center. The WPT efficiency ( $KQ$ ) at the center is high, while the transmission capacity at the surroundings is strong.

In figure 6.11 and 6.12, the distribution of design parameters is displayed in three dimensions.

It can be found that at 500-600 kHz, 21 turns of 65 mm radius coils exist on Pareto Front due to the high  $S_{21}$  value.

From the reader's perspective, it should be at the lowest frequency edge of the fan-shaped Pareto Front.

This shows that the optimization results are basically consistent with the experimental results, and the coil obtained by JAXA is a feasible solution in the multi-objective optimization.

And we also learned from the optimization that JAXA coil is the best choice with the lowest frequency when switching and driver loss are not considered.

### Design Intuitions

If we regard  $S_{21}$  as power transfer capability and  $KQ$  as efficiency, we can conclude that the coil selected by JAXA has better power transfer capability than efficiency performance, comparing to other designs on Pareto Front.

Reducing the number of turns and increasing the frequency simultaneously can further increase the power transfer capacity, but at the cost of reduced efficiency.

On the contrary, directly increasing the frequency without change of number of turns can increase efficiency, but it will lose transmission capacity.

The boundary between the two changes is determined by the geometry of Pareto Front.

## 6.4 Summary

In this Chapter, we repeat and explain JAXA's coil optimization experiment by applying multi-objective optimization. The optimization results show that the coil design of JAXA is feasible solution in the  $S_{21}$  and  $KQ$  product Pareto Optimization.



# Chapter 7

## Conclusion and Future Work

### 7.1 Conclusion

This thesis discussed coil design parameter and frequency optimization for Lunar Rover WPT system.

Half-numerical half-FE based loss estimation model specially for a PV-WPT system with a secondary-side MPPT converter is established.

To take the frequency splitting phenomenon into consideration for PV-WPT MPPT, the thesis proposed MPPT algorithms not only based on duty variation of DC-DC converter, but also WPT frequency in real time, and achieved higher resonant point tracking during MPPT process.

Optimization method based on various of meta-heuristic algorithms for Lunar Rover WPT system is proposed, with the proposed operation strategy to determine the circuit operation condition, as well as traditional WPT evaluation indicators, both single and multi-objective optimization for coil design parameters and operation frequency is conducted.

Based on proposed operation strategies as well as design example obtained from optimization, over 15 percent of PV-load efficiency improvement is achieved compared to the previous Lunar Rover WPT prototype.

Design intuitions were obtained. For WPT system with the same switching device, lower frequency together with zero pitch, high number of turns large coil is benefit for thermal design. Higher frequency together with large pitch, low number of turns small coil can achieve higher power density, with acceptable thermal density.

Evaluation for JAXA's coil design is conducted based on the proposed method, result shows the consistency of JAXA's experiments and the optimization in this thesis.

## 7.2 Future Work

Firstly, this thesis proposed optimization based on PSO, GA, MOEA/D, MOPSO and proposed LPSO and LMOPSO. However, the improvement of LMOPSO is not obvious compared to the original algorithm, and test experiment is insufficient. Further discussion about algorithm selection and new algorithms is needed.

Secondly, based on proposed 2-D PSO MPPT method, measurement of primary side can be eliminated even during parameter variation, primary circuit can be further simplified. However, there's still driver circuit remains at the primary side. The author is planing to replace the driver circuit by a bidirectional WPT or by multiple coils controlled by secondary side. Together with proposed 2-D PSO, we can achieve a simplest primary side expose to the extreme environment, with only MOSFET and coils remains.

Thirdly, the usual modeling method for foreign metal objects is indutor-resistor model. However, during measurement in this thesis, the author find out it cannot be applied to MT-MLI. New equivalent circuit model for the MT-MLI is in consideration.

# References

- [1] Xuanji. [https://k.sina.cn/article\\_7055636087\\_p1a48c7677001015e84.html](https://k.sina.cn/article_7055636087_p1a48c7677001015e84.html). Accessed: 2021-01-20.
- [2] CC BY-SA 4.0 Fernando de Gorocica. A spanish lunar calender for year 20. <https://commons.wikimedia.org/w/index.php?curid=54520011>. Accessed: 2021-01-20.
- [3] CC BY-SA 3.0 Luc Viatour. Russian lunar rover. <https://commons.wikimedia.org/w/index.php?curid=1254946>. Accessed: 2021-01-20.
- [4] Shunhei Shimada and al. et. Wpt and magnetic transmissive mli for high heat insulating moon explorer. *ESPC*, 2019.
- [5] Andre Kurs, Aristeidis Karalis, Robert Moffatt, John D Joannopoulos, Peter Fisher, and Marin Soljačić. Wireless power transfer via strongly coupled magnetic resonances. *science*, 317(5834):83–86, 2007.
- [6] Bingcheng Ji. Research on wireless power transfer system for pv powered lunar rover with maximum power point tracking control. *Doctor's Thesis of Tokyo University, Graduate School of Frontier Sciences*, 2020.
- [7] Diode iv curve. <https://commons.wikimedia.org/wiki/File:Diode-IV-Curve.svg>. Accessed: 2021-01-20.
- [8] Dowon Kim, Ahmed Abu-Siada, and Adrian Sutinjo. State-of-the-art literature review of wpt: Current limitations and solutions on ipt. *Electric Power Systems Research*, 154:493–502, 2018.
- [9] Jiang Jingshan. Multilayer insulation materials and their application to spacecrafts [j]. *AEROSPACE MATERIALS & TECHNOLOGY*, 4, 2000.
- [10] Bingcheng Ji, Katsuhiro Hata, Takehiro Imura, Yoichi Hori, Shuuhei Shimada, Sayuri Honda, Osamu Kawasaki, and Satoshi Ichikawa. Basic study of solar battery powered wireless power transfer system with mppt mode and dc bus stabilization for lunar rover. In *IECON 2018-44th Annual Conference of the IEEE Industrial Electronics Society*, pages 4787–4792. IEEE, 2018.
- [11] John T Boys and Grant A Covic. The inductive power transfer story at the university of auckland. *IEEE circuits and systems magazine*, 15(2):6–27, 2015.

- [12] Siqi Li and Chunting Chris Mi. Wireless power transfer for electric vehicle applications. *IEEE journal of emerging and selected topics in power electronics*, 3(1):4–17, 2014.
- [13] Takehiro Imura and Yoichi Hori. Maximizing air gap and efficiency of magnetic resonant coupling for wireless power transfer using equivalent circuit and neumann formula. *IEEE Transactions on industrial electronics*, 58(10):4746–4752, 2011.
- [14] Roman Bosshard, Johann Walter Kolar, Jonas Muhlethaler, Ivica Stevanovic, Bernhard Wunsch, and Francisco Canales. Modeling and  $\eta - \alpha$ -pareto optimization of inductive power transfer coils for electric vehicles. *IEEE Journal of Emerging and Selected Topics in Power Electronics*, 3(1):50–64, 2014.
- [15] Matthew Schormans, Virgilio Valente, and Andreas Demosthenous. Practical inductive link design for biomedical wireless power transfer: A tutorial. *IEEE Transactions on Biomedical Circuits and Systems*, 12(5):1112–1130, 2018.
- [16] Zhengchao Yan, Yiming Zhang, Tianze Kan, Fei Lu, Kehan Zhang, Baowei Song, and Chunting Chris Mi. Frequency optimization of a loosely coupled underwater wireless power transfer system considering eddy current loss. *IEEE Transactions on Industrial Electronics*, 66(5):3468–3476, 2018.
- [17] Jia-Sheng Hu, Fei Lu, Chong Zhu, Chang-Yi Cheng, Sin-Li Chen, Tsai-Jiun Ren, and Chunting Chris Mi. Hybrid energy storage system of an electric scooter based on wireless power transfer. *IEEE Transactions on Industrial Informatics*, 14(9):4169–4178, 2018.
- [18] Matthew McDonough. Integration of inductively coupled power transfer and hybrid energy storage system: A multiport power electronics interface for battery-powered electric vehicles. *IEEE transactions on power electronics*, 30(11):6423–6433, 2015.
- [19] Zhenjie Li, Chunbo Zhu, Jinhai Jiang, Kai Song, and Guo Wei. A 3-kw wireless power transfer system for sightseeing car supercapacitor charge. *IEEE Transactions on Power Electronics*, 32(5):3301–3316, 2016.
- [20] Bingcheng Ji, Katsuhiko Hata, Takehiro Imura, Yoichi Hori, Shuhei Shimada, and Osamu Kawasaki. Wireless power transfer system design with power management strategy control for lunar rover. *IEEJ Journal of Industry Applications*, 9(4):392–400, 2020.
- [21] Tanaka Kosuke, Shimada Shuhei, and al. et. The study on thermal control technology to realize the moon exploration rover staying on the moon overnight without nuclear power. *Proceedings of the Space Sciences and Technology Conference*. 3G08, 2017.
- [22] Bingcheng Ji, Katsuhiko Hata, Takehiro Imura, Yoichi Hori, Shuhei Shimada, and Osamu Kawasaki. Mppt control for pv based wireless power transfer system in lunar rover by secondary side converter. In *2019 IEEE PELS Workshop on Emerging Technologies: Wireless Power Transfer (WoW)*, pages 105–110. IEEE, 2019.

- [23] Samer Alsadi and Basim Alsayid. Maximum power point tracking simulation for photovoltaic systems using perturb and observe algorithm. 2012.
- [24] Y. Xiong, S. Qian, and J. Xu. Research on constant voltage with incremental conductance mppt method. In *2012 Asia-Pacific Power and Energy Engineering Conference*, pages 1–4, 2012.
- [25] Qijun Deng, Jiangtao Liu, Dariusz Czarkowski, Marian K Kazimierczuk, Mariusz Bojarski, Hong Zhou, and Wenshan Hu. Frequency-dependent resistance of litz-wire square solenoid coils and quality factor optimization for wireless power transfer. *IEEE Transactions on Industrial Electronics*, 63(5):2825–2837, 2016.
- [26] Hong Zhou, Xingran Gao, Jingang Lai, Wenshan Hu, Qijun Deng, and Dongguo Zhou. Natural frequency optimization of wireless power systems on power transmission lines. *IEEE Access*, 6:14038–14047, 2018.
- [27] Nazmul Hasan, Tuba Yilmaz, Regan Zane, and Zeljko Pantic. Multi-objective particle swarm optimization applied to the design of wireless power transfer systems. In *2015 IEEE Wireless Power Transfer Conference (WPTC)*, pages 1–4. IEEE, 2015.
- [28] Nazmul Hasan. Optimization and control of lumped transmitting coil-based in motion wireless power transfer systems. 2015.
- [29] Darrell Whitley. A genetic algorithm tutorial. *Statistics and computing*, 4(2):65–85, 1994.
- [30] James Kennedy and Russell Eberhart. Particle swarm optimization. In *Proceedings of ICNN'95-international conference on neural networks*, volume 4, pages 1942–1948. IEEE, 1995.
- [31] Qingfu Zhang and Hui Li. Moea/d: A multiobjective evolutionary algorithm based on decomposition. *IEEE Transactions on evolutionary computation*, 11(6):712–731, 2007.
- [32] C. A. C. Coello, G. T. Pulido, and M. S. Lechuga. Handling multiple objectives with particle swarm optimization. *IEEE Transactions on Evolutionary Computation*, 8(3):256–279, 2004.
- [33] Jie Zhou, De-jun Li, and Ying Chen. Frequency selection of an inductive contactless power transmission system for ocean observing. *Ocean Engineering*, 60:175–185, 2013.
- [34] Ryuji Itoh, Yuichi Sawahara, Toshio Ishizaki, and Ikuo Awai. Wireless power transfer to moving ornamental robot fish in aquarium. In *2014 IEEE 3rd Global Conference on Consumer Electronics (GCCE)*, pages 459–460. IEEE, 2014.
- [35] Zhengchao Yan, Kehan Zhang, Haibing Wen, and Baowei Song. Research on characteristics of contactless power transmission device for autonomous underwater vehicle. In *OCEANS 2016-Shanghai*, pages 1–5. IEEE, 2016.

- [36] Dries Van Wagoningen and Toine Staring. The qi wireless power standard. In *Proceedings of 14th International Power Electronics and Motion Control Conference EPE-PEMC 2010*, pages S15–25. IEEE, 2010.
- [37] R. Huang, B. Zhang, D. Qiu, and Y. Zhang. Frequency splitting phenomena of magnetic resonant coupling wireless power transfer. *IEEE Transactions on Magnetics*, 50(11):1–4, 2014.
- [38] Takehiro Imura. Research on wireless power transfer using electromagnetic resonant coupling. *Doctor's Thesis of Tokyo University, Electrical Engineering Department*, 2010.
- [39] David Meeker. Finite element method magnetics. *FEMM*, 4:32, 2010.
- [40] NASDA-ADS-2130/502-01 Sharp. Photo-voltaic cell for space application datasheet, 2003.
- [41] Marian K Kazimierczuk and Dariusz Czarkowski. *Resonant power converters*. John Wiley & Sons, 2012.
- [42] Chwei-Sen Wang, Grant A Covic, and Oskar H Stielau. Power transfer capability and bifurcation phenomena of loosely coupled inductive power transfer systems. *IEEE transactions on industrial electronics*, 51(1):148–157, 2004.
- [43] Rohm. Switching regulator ic series efficiency of buck converter application note, 2016.
- [44] Jonas Mühlethaler. *Modeling and multi-objective optimization of inductive power components*. PhD thesis, ETH Zurich, 2012.
- [45] Fausto Fiorillo. *Measurement and characterization of magnetic materials*. North-Holland, 2004.
- [46] Bingcheng Ji, Katsuhiro Hata, Takehiro Imura, Yoichi Hori, Sayuri Honda, Shuhei Shimada, and Osamu Kawasaki. A novel particle jump particle swarm optimization method for pv mppt control under partial shading conditions. *IEEJ Journal of Industry Applications*, 9(4):435–443, 2020.
- [47] Bingcheng Ji, Katsuhiro Hata, Takehiro Imura, Yoichi Hori, Shuhei Shimada, and Osamu Kawasaki. Pv mppt control under partial shading conditions with a particle replacement gaussian particle swarm optimization method. *IEEJ Journal of Industry Applications*, 9(4):418–427, 2020.
- [48] Edison Pettit and Seth B Nicholson. Lunar radiation and temperatures. *The Astrophysical Journal*, 71:102–135, 1930.
- [49] Tuba Yilmaz, Nazmul Hasan, Regan Zane, and Zeljko Pantic. Multi-objective optimization of circular magnetic couplers for wireless power transfer applications. *IEEE Transactions on Magnetics*, 53(8):1–12, 2017.

- [50] Sami Barmada, Marco Raugi, and Mauro Tucci. A multi-objective optimization algorithm based on self-organizing maps applied to wireless power transfer systems. *International Journal of Numerical Modelling: Electronic Networks, Devices and Fields*, 30(3-4):e2145, 2017.
- [51] Kate Doubleday, Ashish Kumar, Brandon Regensburger, Saad Pervaiz, Sreyam Sinha, Zoya Popovic, and Khurram K Afridi. Multi-objective optimization of capacitive wireless power transfer systems for electric vehicle charging. In *2017 IEEE 18th Workshop on Control and Modeling for Power Electronics (COMPEL)*, pages 1–8. IEEE, 2017.
- [52] Xun Li, Kwai Man Luk, and Baoyan Duan. Multiobjective optimal antenna synthesis for microwave wireless power transmission. *IEEE Transactions on Antennas and Propagation*, 67(4):2739–2744, 2019.
- [53] SCT2080KE N Rohm. channel sic power mosfet datasheet, 2014.
- [54] K. Deb, A. Pratap, S. Agarwal, and T. Meyarivan. A fast and elitist multiobjective genetic algorithm: Nsga-ii. *IEEE Transactions on Evolutionary Computation*, 6(2):182–197, 2002.





# Appendix A

## Publication Lists

### A.1 Published

- Mingyang Chen, Bingcheng Ji, Katsuhiro Hata, Takehiro Imura, Hiroshi Fujimoto, Yoichi Hori, Shuhei Shimada, Sayuri Honda, Osamu Kawasaki "Frequency Optimization of Lunar Rover Wireless Power Transfer System with Multi-layer Insulation", 2019 IEICE Wireless Power Transfer Seminar, 2019/10/09, Kyoto, Japan.
- Mingyang Chen, Bingcheng Ji, Katsuhiro Hata, Takehiro Imura, Hiroshi Fujimoto, Yoichi Hori, Shuhei Shimada, Sayuri Honda, Osamu Kawasaki "Pareto Optimization of Power and Efficiency for Lunar Rover Wireless Power Transfer System with Multi-layer Insulation ", Asian Wireless Power Transfer Workshop 2019 2019/11/02, Xian, China.

### A.2 To be submit

- Mingyang Chen, et al. "Pareto Optimization for Lunar Rover Wireless Power Transfer Coil Parameters and Operation Frequency"
  - To be submit to IEEEJ Transactions of Industry Applications
- Mingyang Chen, et al. "Frequency-duty Two-Dimesional Maximum Power Point Tracking for Lunar Rover Wireless Power Transfer System"
  - To be submit to IEEEJ Transactions of Industry Applications

### **A.3 Awards**

- Asian Wireless Power Transfer Workshop Student Award